



Light Upconverting Core-Shell Nanostructures: Nanophotonic Control for Emerging Applications

Journal:	<i>Chemical Society Reviews</i>
Manuscript ID:	CS-REV-05-2014-000170.R2
Article Type:	Review Article
Date Submitted by the Author:	09-Sep-2014
Complete List of Authors:	Chen, Guanying; State University of New York at Buffalo, Institute for Lasers, Photonics and Biophotonics; Harbin Institute of Technology, Chemistry Agren, Hans; Royal Institute of Technology, Department of Theoretical Chemistry & biology Ohulchanskyy, Tymish; State University of New York at Buffalo, , Institute for Lasers, Photonics and Biophotonics Prasad, Paras; Institute for Lasers, Photonics, and Biophotonics,

Light Upconverting Core-Shell Nanostructures: Nanophotonic Control for Emerging Applications

Guanying Chen,^{1,2} Hans Ågren,³ Tymish Y. Ohulchansky,¹ and Paras N. Prasad^{1,4*}*

¹Institute for Lasers, Photonics, and Biophotonics and Department of Chemistry, University at Buffalo, State University of New York, Buffalo, New York 14260, United States

²School of Chemical Engineering and Technology, Harbin Institute of Technology, Harbin, Heilongjiang 150001, People's Republic of China

³Department of Theoretical Chemistry&Biology, Royal Institute of Technology, S-10691 Stockholm, Sweden

⁴Department of Chemistry, Korea University, Seoul 136-701, Korea

*E-mails: chenguanying@hit.edu.cn, pnprasad@buffalo.edu

Abstract: Light upconverting nanostructures employing lanthanide ions constitute an emerging research field recognized with wide ramifications and impact in many areas ranging from healthcare, to energy and, to security. The core-shell design of these nanostructures allows to deliberately introduce hierarchy of electronic energy states, thus providing unprecedented opportunities to manipulate the electronic excitation, energy transfer and upconverted emissions. The core-shell morphology also provides suppression of quenching mechanisms to produce efficient upconversion emission for biophotonic and photonic applications. Using hierarchical architect, whereby each shell layer can be defined to have a specific feature, the electronic structure as well as the physiochemical structure of the upconverting nanomaterials can be tuned to couple other electronic states on the surface such as excitations of organic dye molecules or localized surface plasmons from metallic nanostructures, or to introduce a broad range of imaging or therapeutic modalities into a single

conduct. In this review, we summarize key aspects of nanophotonic control of the light upconverting nanoparticles through governed design and preparation of hierarchical shells in the core/shell nanostructures, and review their emerging applications in biomedical applications, solar energy conversion, as well as security encoding.

1. Introduction

Photon upconversion (UC) refers to an anti-Stokes process in which two or more low energy photons are sequentially or step-wise absorbed *via* real intermediate long-lived electronic states, resulting in an excitation of a higher electronic state, emitting a higher energy photon.^{1, 2} It is distinct from conventional multi-photon absorption induced fluorescence, whereby multiple photons are simultaneously absorbed using virtual intermediate electronic states to produce photon with higher energy,³ and from conventional nonlinear sum frequency generation (typically, second harmonic generation), where two incident photons (at different or same frequencies) are parametrically annihilated in a non-centrosymmetric medium to produce a photon with summed energy.⁴⁻⁶ The advantage offered by sequential excitation is a possibility of generating UC with an excitation power density as low as $\sim 10^{-1}$ W/cm² easily provided by low cost continuous-wave laser diodes or incoherent light sources such as bulb lamps and light emitting diodes. This low power excitation density is in marked contrast to the high power density excitation ($>10^6$ W/cm²) required in nonlinear multiphoton absorption in which an expensive ultrashort pulsed laser has to be employed.³ The idea of photon UC originated from Bloembergen in 1959, who proposed that infrared (IR) light could be detected by sequential absorption of an ion in a solid material.⁷ This concept was then realized and formulated independently by Auzel,⁸ Ovsyankin and Feofilov^{9,10} in the mid-1960s. For a long time, the investigation of photon UC remained centered on f-ion (lanthanide) or d-ion (transition metal)

doped bulk crystalline materials or glasses for use in UC lasers, IR detection, optical storage, etc.¹ It is only recently that photon UC in nanomaterials has captured worldwide attention, because of the advantage offered by nanochemistry to fabricate unique nanostructures with nanophotonic control of the excitation dynamics.¹¹ Photon UC has been reported for many types of nanomaterials, such as lanthanide-doped nanostructures,¹² transition metal-doped nanoparticles,¹³ defects-doped nanostructures,¹⁴ quantum nanostructures,¹⁵ as well as nanoparticles containing organic molecules as donor-acceptor pairs in triplet-triplet annihilation UC.^{15,16} Lanthanide-doped UC nanoparticles (UCNPs) are known as a major thrust area of current research of UC in nanoparticles. The discussion within this review will be limited to this type of UC, with a focus on the emerging hierarchal core/shell structured UCNPs.

Lanthanide-doped UCNPs can be considered as dilute guest-host systems, where trivalent lanthanide ions are dispersed as guests in an appropriate inorganic host lattice with a dimension of less than 100 nm.² The inorganic host lattice can be either a dielectric material¹⁷ or a wide band gap semiconductor.¹⁸ A UC is often more efficient in dielectric materials (e.g., sodium yttrium fluoride, NaYF₄), as they are more favorable to incorporate trivalent lanthanide ions without the need of generating vacancies for charge compensation, and generally have lower phonon cutoff energy, which is important to minimize nonradiative energy losses.^{2,19} Light absorption and emission in the lanthanide dopants involves the *4f-4f* orbital electronic transitions with concomitant wave-functions localized within a single lanthanide ion. The electronic energy gap of a lanthanide ion does not change with a change in the size or shape of UCNPs.¹¹ As a result, lanthanide doped materials generally do not exhibit quantum confinement effects that are clearly manifested in semiconducting materials. Each lanthanide element has a unique electronic configuration, with a system of

well-defined, fine structured energy levels. The fine ladder-like structure of long-lived energy levels covers a broad range of energy. Owing to the pioneering work by Dieke,²⁰ Judd,²¹ Ofelt,²² Wybourne,²³ and others in theoretical and experimental studies of the $4f^N$ electronic structure, most of the energy levels of trivalent lanthanide ions (known as Dieke energy levels), which determine optical properties of lanthanides, have already been established. Because of shielding of the $4f$ electrons by the outer complete $5s$ and $5p$ shells, trivalent lanthanide ions can display line-like sharp, stable emission under photoexcitation. By a judicious selection of one or more lanthanide dopants, UCNPs are able to generate upconverted photoluminescence (UCPL) at selective wavelengths, after being excited with light of longer wavelength. Thus, an energy upconversion takes place, when light is converted from infrared (IR) region to near infrared (NIR) one, NIR to shorter NIR, NIR to visible (VIS), or NIR to Ultraviolet (UV), etc. This light upconversion feature opens up numerous opportunities for the applications of energy nanoconverters, such as in high-contrast deep tissue bioimaging,^{24, 25} photodynamic therapy in deep tissue,²⁶ remote photoactivation,²⁷ security and display,²⁸ biosensing,²⁹ temperature sensing,^{30, 31} drug release and gene delivery,³² as well as in solar cells.^{33, 34} However, conventional lanthanide-doped UCNPs have a number of problems which still limit their practical applications. Some examples are low upconversion efficiency associated with nanosize-induced surface-related quenching effects, undesired interactions between lanthanide ions that seriously constrains the upconversion design, limited excitation light harvesting ability as well as the excitation wavelength tunability, as well as limited functionalities for imaging and therapy. Despite their promising applications in many areas, these limitations prevent rapid evolvement of UCNPs from laboratory bench to clinical, technological and industrial applications.

Hierarchical design of the core/shell UCNPs, whereby each shell layer can be defined within a

regulated scale to introduce a specific feature, provides a range of unique nanophotonic solutions to address the challenges associated with conventional UCNPs and offers new imaging and therapeutic properties, while completely conserving all the merits of conventional UCNPs. With the ability of nanochemistry to produce a shell of stoichiometric composition and a shell thickness with monolayer precision, the electronic structure as well as the physiochemical structure of the upconverting system can be purposely aligned for nanophotonic control of upconversion or to introduce a broad range of imaging or therapeutic modalities into a single conduct. The advantages provided by the core/shell structure encompass:

(i) Higher upconversion efficiency due to suppression of surface-related quenching effect produced by an epitaxial growth of a shell layer. The shell layer is able to provide an effective passivation of lattice defects located on the surface of a core nanoparticle, as well as to create a perfect spatial isolation of the core nanoparticle from the surrounding environment. This results in significant enhancement of the upconversion efficiency which is dependent on the shell type, the defects in the shell, and the thickness of the shell layer.

(ii) Nanoscopic control of ion-ion interactions through spatial confinement of different types of lanthanide dopants in separated shell layers or the core domain. The interaction between lanthanide ions of the same or different types can be precisely engineered by appropriate arrangement of the electronic energy level hierarchy for lanthanides in different shell layers as well as by manipulating the shell thickness to control the interaction strength. This directed interaction provides powerful tools to manipulate the energy transfer processes which are the essence of photon upconversion. As such, the excitation wavelength, the emission color, the absorption of nanoparticles, as well as any

quenching effect can be manipulated for a favorable photon upconversion effect.

(iv) Coupling with new excitation electronic states of dyes or localized surface plasmon resonance (LSPR) for enhanced or broad band upconversion. The nature of 4f-4f electronic transitions in lanthanide ions results in low extinction and narrow absorption band, posing limitations for light harvesting as well as for upconversion efficiency of UCNPs. Coupling them with LSPR, using a core/shell structure, may result in plasmonically induced upconversion emission enhancement.³⁵ Introducing an organic dye shell layer to the surface of UCNPs can cause interaction of the electronic states of dye molecules with that of 4f electrons for energy transfer to lead to upconversion, taking advantage of the high extinction coefficient and large spectral width of organic dyes for light harvesting. These types of core/shell architecture will alleviate the limitations posed by the nature of 4f electrons.

(iv) Generation of new functionalities and multifunctionalities for theranostic applications. The limited functionality of conventional UCNPs can be significantly extended by an epitaxial growth of functional layers that produce new imaging functionalities (for example, the growth of Gd^{3+} -containing shell layer creates the capability for magnetic resonance imaging).³⁶ Along with enriched optical properties, the group of lanthanide elements also has unique magnetic, x-ray absorption, and radiation enhancement properties.² Appropriate doping of lanthanide ions into the multiple shell layers or the core domain can introduce multimodal imaging abilities in a hierarchical core/shell structure without interfering each other, thus accelerating uses of UCNPs as multimodal imaging probes. In addition, the UCNPs can be further coated with a non-epitaxial silica or polymer shell which is able to entrap, encapsulate, or complex drugs, providing therapeutic opportunities for

drug/gene delivery and light-activated therapy (such as photodynamic therapy (PDT) or photothermal therapy (PTT)).^{26, 37} A combination of imaging modalities, provided by epitaxial core/shell structure, and the therapeutic modalities, created by the non-epitaxial shell, promises use of UCNPs-based nanostructures as new generation theranostic nanoplatfoms.

Indeed, core/shell UCNPs produce numerous unprecedented abilities to manipulate the excitation dynamics (the emission properties, including color, efficiency, and lifetime, energy transfer, and cooperative optical transitions) to create UC emission of needs, and to provide new multifunctionalities for effective diagnostics and therapeutics as well as for other nanophotonic applications such as in solar energy conversion. In this work, we review nanophotonic control of upconversion in hierarchically designed core/shell nanostructures based on UCNPs, as well as their application in biomedical applications, solar cells, and security encoding.

2. Nanophotonic Control of Upconversion in Core/Shell Nanoparticles

Photon upconversion employing lanthanides can be produced via six fundamental mechanisms, *i.e.*, excited state absorption, energy transfer upconversion, cooperative sensitization upconversion, cooperative upconversion, cross relaxation, and photon avalanche.^{1, 2} The essence of these mechanisms is sequential excitation through the excited states of a single lanthanide ion or ion-ion interactions in the excited states to allow energy transfer between two or more lanthanide ions.^{2, 11} These features are regulated by the f-f transition nature of lanthanide ions, the local environment around them, as well as the lanthanide ions distributions within a single nanoparticle (or the ion-ion distance within a single nanoparticle). Typically, UCNPs contain lanthanide emitters with ladder-like system of energy levels (e.g., Er³⁺, Tm³⁺, and Ho³⁺ ions), as well as of a sensitizer (e.g., Yb³⁺ ions) to

harvest the excitation energy and nonradiatively transfer to the emitters (energy transfer upconversion mechanism).²

Nanophotonics is an emerging frontier which deals with the interaction of light with matter on a nanometer size scale.¹⁹ A core/shell epitaxial structure can produce important manifestation in defining a local coordinating environment for surface lanthanides, which is distinct from that for the interior lanthanide ions (i.e., bulk crystal field) due to the size-reduction induced structural distortion, surface defects, coordinated organic ligands, etc. Moreover, core/multishell epitaxial structures provide opportunities to engineer the distribution of lanthanide ions as well as to appropriately arrange their energy levels within a nanostructure. As a consequence, a core/shell structure provides nanophotonic means to tailor light excitation harvesting, upconversion efficiency, upconversion emission wavelengths, directed energy transfer, cross relaxation, as well as dopant concentration quenching threshold.² A core-shell hierarchical architecture also offers a structural flexibility for enhancing a specific upconversion or introducing multifunctionalities. In the following sections of 2.1-2.7, we will summarize seven approaches that have been typically used for nanophotonic control of a core/shell nanostructure (Figure 1).

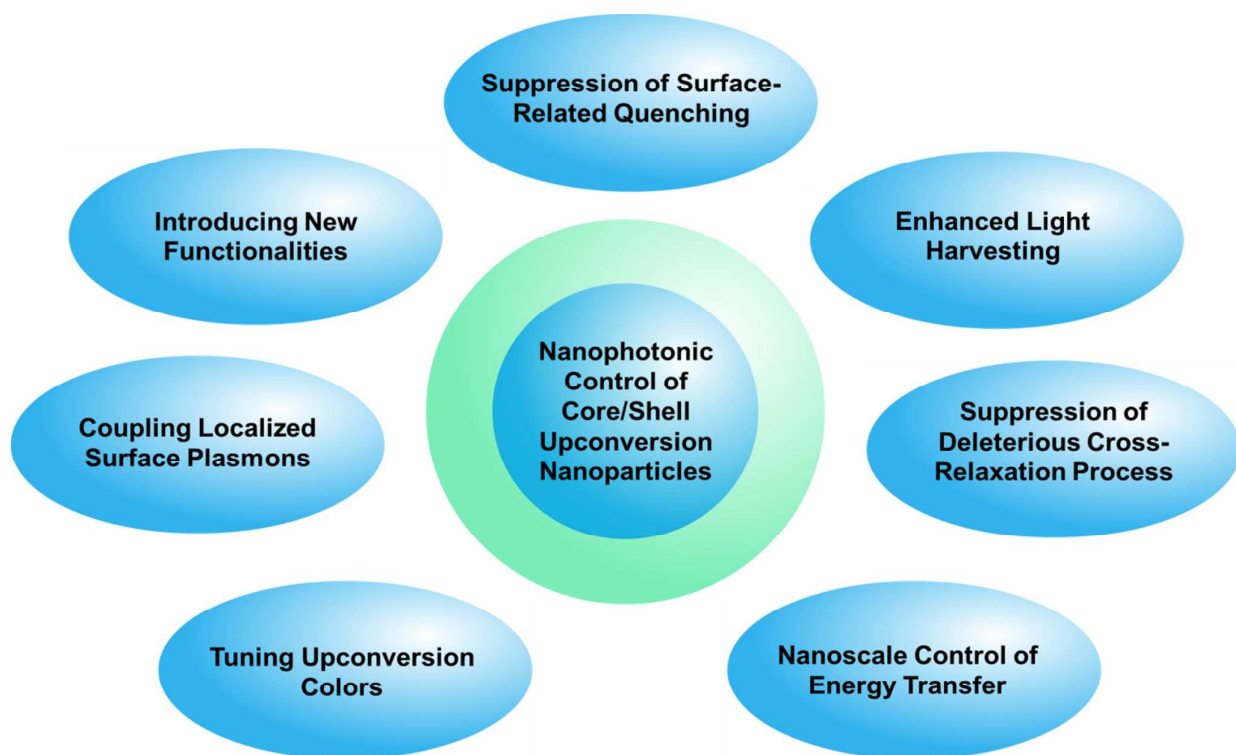


Figure 1. Seven directions for nanophotonic control of upconversion in a core/shell nanostructure.

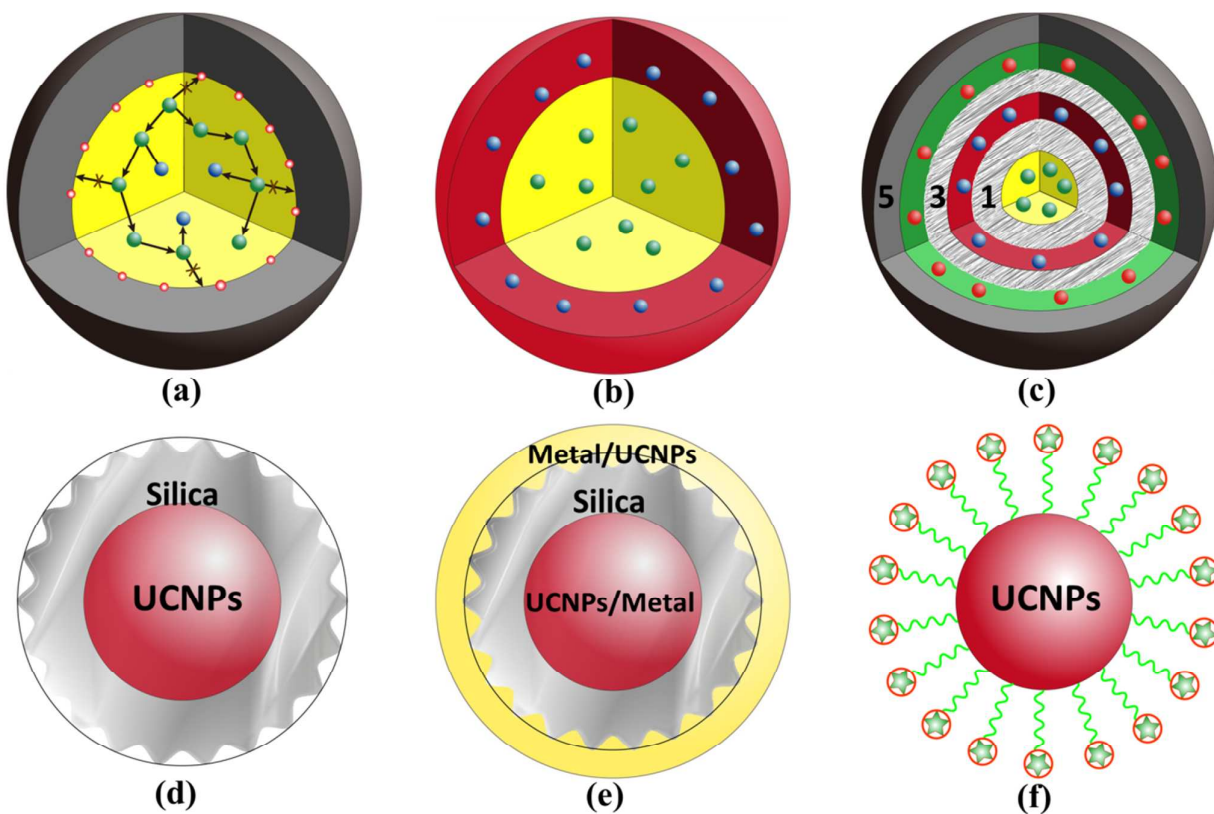


Figure 2. Different types of core/shell structure. The upper panel illustrates core/shell UCNPs with

epitaxial layers: (a) core/shell UCNPs with an “inert” (i.e., without any absorbing/emitting lanthanide dopant) shell layer; the colored balls in the core area depict lanthanide dopants; the red circles at the interface represent surface quenching sites; the black arrows indicate random energy transfer pathways. (b) core/shell UCNPs with an active shell layer (i.e., layers containing “active” lanthanide dopants); and (c) core/shell UCNPs with multiple shell layers. Core/multishell type (c) is exemplified using five layers, in which layer 1 and layer 3 (the gray striped ones) can be either inert layers to avoid undesirable interactions between the active layers (the colored ones), or active layers to enhance the interactions between different active domains. The bottom panel depicts core/shell UCNPs with non-epitaxial layers: (d) UCNPs@silica core/shell nanoparticles, (e) core/shell/shell UCNPs@silica@metal (or metal@silica@UCNPs) nanoparticles, and (f) UCNPs coated by organic dye molecules.

The core/shell nanostructures utilized in recent progresses can be broadly classified in two categories: 1) A core-shell nanoparticle containing epitaxial layers with matched or nearly matched crystalline lattice; 2) a core-shell nanoparticle containing non-epitaxial layers. The core nanoparticle here can be either conventional UCNPs without any epitaxial shell or core/shell UCNPs with epitaxial shell layers. Figure 2 gives examples of six types of core/shell UCNPs from these two categories, which constitute most of current core/shell design to produce selective UC emissions as well as to deliver multifunctionalities to reach comprehensive imaging and therapeutic modalities.

2.1. Core/Shell Structure to Control Surface-Related Quenching

Suppression of surface-related quenching effects is a typical way of enhancing upconversion efficiency of UCNPs through control of the local environment of surface lanthanide ions. Although

this approach has been frequently utilized, the involved specific mechanisms remain experimentally unverified albeit few attempts.³⁸⁻⁴⁰ Surface-related quenching effects for the core UCNPs stem from the high surface-to-volume ratio produced by the nanometer dimension, which exposes most of lanthanide dopants to surface induced deactivation (surface defects, ligands, and solvents that possess high energy phonons). The partition of exposed lanthanide dopants strongly depends on the size of the synthesized core nanoparticles, but also is influenced by the nature of the surrounding environment.^{11, 40} In principle, surface related quenching mechanisms can be divided into two types:

(i) Direct Quenching. Dopants located on or close to surface are directly deactivated by neighboring quenching centres through nonradiative relaxation involving phonons from the surrounding environment. This deactivation pathway applies to a range of intermediate excited states involved in producing UC emission, resulting in more pronounced quenching than in the case of Stokes-shifted (downconversion) luminescence, which involves one exclusive emitting state. Direct quenching is a general surface-related quenching mechanism for all types of luminophores with nanoscale dimension.

(ii) Energy Migration Induced Quenching. The electronic excitation energy of dopants located inside can randomly migrate inside UCNPs and travel to other dopant centres on/around the surface or directly to the surface quenching sites. This type of surface-related quenching mechanisms requires the existence of long-lived energy states favorable for excitation energy hopping. This is generally the case for conventional UCNPs, for example, $\text{NaYF}_4:\text{Yb}^{3+}/\text{Ln}^{3+}$ ($\text{Ln}=\text{Er}, \text{Ho}, \text{Tm}$),⁴¹⁻⁴³ which contain a high concentration of sensitizer ($\text{Yb}^{3+} \geq 18\%$) that has an exclusive long-lived state. However, the mechanism of energy migration induced quenching has not been experimentally substantiated until this point. On the other hand, the migration of excitation energy is also a

necessary prerequisite for adequate activation of lanthanide emitters to produce efficient upconversion emission. An optimized lanthanide concentration for nanoparticles that are devoid of any shell originates from a delicate balance between quenching and emission produced by energy migration. A controlled suppression or elimination of energy-migration-induced quenching mechanism (using core/shell structure) might result in determination of distinct optimized lanthanide concentration that will be a big step in development of the efficient UCNPs. .

The two types of surface-related quenching mechanisms can be addressed through an epitaxial growth of one or multiple inert (i.e., not containing lanthanide dopants) outer shell layer on the core nanoparticle (Figure 2 a), which passivates the imperfections in the host lattice (often located at the core particle surface), and shields the core from the surrounding ligands (which are necessary for solvent dispersion) and solvents of high phonon energy. The distance between the UCNP core and the surrounding environment, created by the inert epitaxial shell, prevents quenching of the excited states of the surface lanthanide ions and curbs the migration of excitation energy into the surrounding environment.^{2, 11} The epitaxial shell layer can be the same as the host lattice of the core nanoparticle or of different composition but having a low lattice mismatch with that of the core nanoparticle. The quality as well as the thickness of the shell is of paramount importance to minimize surface-related quenching mechanisms. The followings describe some variations of this type of core-shell structures.

Homogenous Active Core/Inert Shell. Homogenous active (i.e., containing “active” lanthanide dopants) core/inert shell nanoparticle refers to the one where the core and the shell materials have an identical host lattice (Figure 2 a). This type of core/shell structure has been investigated for a myriad of host lattice materials for a broad range of core sizes and shell thicknesses. For example, upconversion enhancement up to tens of times has been observed in $(\text{NaYF}_4:\text{Yb}^{3+}/\text{Ln}^{3+})/\text{NaYF}_4$

$(\text{Ln}=\text{Er}$ or $\text{Tm})$,^{44, 45-50} $(\text{KYF}_4:\text{Yb}^{3+}/\text{Er}^{3+})@ \text{KYF}_4$,⁵¹ $(\text{SrF}_2:\text{Yb}^{3+}/\text{Er}^{3+}) @ \text{SrF}_2$,⁵²
 $(\text{NaGdF}_4:\text{Yb}^{3+}/\text{Tm}^{3+})@ \text{NaGdF}_4$,^{40,53} $(\text{KGdF}_4:\text{Yb}^{3+}/\text{Tm}^{3+})@ \text{KGdF}_4$,⁵⁴ $(\text{YOF}:\text{Yb}^{3+}/\text{Er}^{3+}) @ \text{YOF}$,⁵⁵
 $(\text{YF}_3:\text{Yb}^{3+}/\text{Ln}^{3+})@ \text{YF}_3$ ($\text{Ln}=\text{Er}$, Tm , or Er/Tm)⁵⁶, $(\text{LaF}_3:\text{Yb}^{3+}/\text{Tm}^{3+})/\text{LaF}_3$,
 $(\text{BaLaF}_5:\text{Yb}^{3+}/\text{Tm}^{3+})/\text{BaLaF}_5$,⁵⁷ and $(\text{NaLuF}_4:\text{Gd}^{3+}/\text{Yb}^{3+}/\text{Er}^{3+})@ \text{NaLuF}_4$,⁵⁸ when excited under NIR
excitation at ~ 980 nm. Absolute quantum yield measurements verified that 30 nm
 $(\text{NaYF}_4:\text{Yb}^{3+}/\text{Er}^{3+})@ \text{NaYF}_4$ core/shell UCNP were 3 times more efficient than the $\text{NaYF}_4:\text{Yb}^{3+}/\text{Er}^{3+}$
core nanoparticles of the same size.⁵⁹ This result provides a direct evidence on the effectiveness of an
inert shell to suppress surface-related quenching effect to increase the upconversion efficiency. It is
important to note that the UC quantum yield (UCQY) or efficiency is dependent on the excitation
power density due to the nonlinearity of the UC processes. As a result, the UCQY should be always
considered in the accompaniment of the excitation power density. We have reported an absolute
upconversion efficiency of $\sim 4\%$ in $\text{NaYF}_4:\text{Er}^{3+}@ \text{NaYF}_4$ core/shell nanoparticles under 1523 nm
excitation with a power density of 20 W/cm^2 .⁶⁰ More recently, $(\text{LiLuF}_4:\text{Yb}^{3+}/\text{Er}^{3+})@ \text{LiLuF}_4$
nanoparticles manifested a quantum yield of 5.0% , while $(\text{LiLuF}_4:\text{Yb}^{3+}/\text{Tm}^{3+})@ \text{LiLuF}_4$ nanoparticles
reached as high as 7.6% under laser power density of 127 W/cm^2 at ~ 980 nm.⁶¹ These newly
determined values of upconversion efficiency of core/shell nanoparticles are close to or higher than
the previously reported ones for bulk materials,⁶² confirming the effectiveness of a shell to suppress
surface-related quenching mechanisms. The relation between the intensity of UCPL and the
thickness of the shell can be described either by a linear dependence (for a few monolayer
thicknesses less than ~ 2.4 nm)⁶³ or by an exponential function, with the optimized shell thickness
(i.e., thickness which effectively enhances the UCPL intensity without an excessive increase of the
overall size of the UCNP) determined to be around 6nm .⁶⁴ More insights are needed to shed light on

this dependence of the UCPL intensity on the shell thickness and thereby to provide guidance for an optimization of a shell, which should be thin but adequate enough to prevent the quenching by the environment.

Heterogeneous Active Core/Inert Shell. Heterogeneous core/shell nanoparticles with the core and the shell host matrix of different compositions (Figure 2 a) have also been investigated for improvement of UCPL. For example, Yan *et al.* reported ~ 300 -fold enhancement of UC emission yield in the 10-13 nm cubic $\text{NaYF}_4:\text{Ln}^{3+}@\text{CaF}_2$ heterogeneous core/shell nanoparticles in comparison to the parent $\text{NaYF}_4:\text{Ln}^{3+}$ nanoparticles.⁶⁵ Such enhancement is extraordinary, as only tens fold enhancements were reported for homogenous core/shell UCNPs (see above). This suggests the importance of the selection of shell types which are evidently different in the ability to passivate the imperfections on the core nanoparticle surface and to minimize the quenching effects from environment. We demonstrated that a hetero-shell of CaF_2 can enhance NIR-to-NIR UCPL from ~ 20 nm $\text{NaYbF}_4:\text{Tm}^{3+}$ by about 35-fold, causing UCQY to be as high as 0.6% under low excitation power density of 0.3 W/cm^2 .²⁵ Han *et al.* reported that NIR-to-UV UC emission in a series of cubic $\text{NaYF}_4:(20\text{-}100\%)\text{Yb}^{3+}/\text{Tm}^{3+}@\text{CaF}_2$ epitaxial core/shell nanoparticles can be enhanced by two orders of magnitude, when compared with the core nanoparticles.⁶⁶ It was suggested that if compared to the typically used NaYF_4 shell, the CaF_2 coating is more effective in resisting quenching in aqueous medium to preserve the upconverted emission and also in suppression of any lanthanide chemical leakage.⁶⁵ The core/shell $\text{NaYF}_4:\text{Ln}^{3+}@\text{NaGdF}_4$ nanoparticles with fixed or tunable shell thicknesses have also been successfully prepared to yield much more efficient upconversion luminescence.^{67, 68} Note that UCPL from the cubic form NaYF_4 is known to be about one order of magnitude less efficient than that from the hexagonal form NaYF_4 .⁶⁹ However, the reported UCPL of

$\text{NaYF}_4:\text{Yb}^{3+}/\text{Tm}^{3+}@/\text{CaF}_2$ is higher or comparable to that of the corresponding hexagonal $\text{NaYF}_4:\text{Yb}^{3+}/\text{Tm}^{3+}@/\text{NaYF}_4$ core/shell nanoparticles, revealing the great potential of developing new heterogeneous core/shell type structures to significantly increase the upconversion efficiency. Indeed, our recent work on ~ 24 nm hexagonal $(\text{NaYbF}_4:\text{Tm}^{3+}/\text{Gd}^{3+})@/\text{NaYF}_4$ core/shell structure showed a ~ 350 fold UCPL enhancement as compared to UCPL from the ~ 22 nm core nanoparticles.⁷⁰

2.2. Core/Shell Structure to Enhance Light Harvesting

Generally, UCNPs have severely limited light absorbing ability due to their low extinction coefficient and narrow band absorption of lanthanide ions. This problem mainly arises from the dipole-dipole forbidden nature of 4f-4f transitions as well as from well-shielded localized electronic wave-function for lanthanide ions in UCNPs, which severely limit use of UCNPs in many applications. An engineering of the core/shell structure provides a new dimension to alleviate or resolve the absorption related issues by introducing absorption from new type of lanthanides or by coupling lanthanide ions with electronic states from organic dyes. Indeed, instead of utilizing an inert epitaxial shell material as discussed in above section, a reasonable concentration of light absorbing dopants can also be introduced in the shell layer or multiple shell layers to enhance light harvesting (Figures 2 b and c). The introduced dopants can be the sensitizer lanthanide ions (e.g., Yb^{3+}) to increase the absorption of the nanoparticles at the certain wavelength (e.g., ~ 980 nm), or multiple types of lanthanide ions to broaden the light excitation/emission range. Moreover, the shell can also be organic in nature, containing a number of dye molecules to provide an intensive and broad absorption band for light harvesting, followed by nonradiatively transfer of the harvested energy to lanthanide ions in the core. The shell layer now takes three roles: (i) Suppression of surface-related deactivation; this role is the same as in core/shell structure with an inert shell. (ii) Enhancement of

UCPL produced by interaction of the lanthanide dopants in the shell with the lanthanide dopants located in the core nanoparticles (Figure 2 b). (iii) Harvesting of light over a broad spectral wavelength range by different types of lanthanide ions in different shells (Figure 2 c) or using an organic dye shell (Figure 2 f).

2.2.1 The Shell Containing Absorbing Lanthanide Dopants

Capobianco *et al.* first reported on $\text{NaGdF}_4:\text{Yb}^{3+}/\text{Er}^{3+}@/\text{NaGdF}_4:\text{Yb}^{3+}$ active core/active shell nanoparticles, displaying a significant increase in the intensity of NIR-to-visible upconversion, when compared to either the $\text{NaGdF}_4:\text{Yb}^{3+}/\text{Er}^{3+}$ active-core@ NaGdF_4 inert-shell, and $\text{NaGdF}_4:\text{Yb}^{3+}/\text{Er}^{3+}$ core only nanoparticles.⁷¹ The active core/active shell strategy has also been utilized in the $\text{NaYF}_4:\text{Yb}^{3+}/\text{Er}^{3+}@/\text{NaYF}_4:\text{Yb}^{3+}$,⁷²⁻⁷⁴ $(\text{CaF}_2:\text{Yb}^{3+}/\text{Tm}^{3+}/\text{Ho}^{3+})/\text{NaYF}_4:\text{Yb}^{3+}$,⁷⁵ $\text{LaPO}_4:\text{Er}^{3+}@/\text{LaPO}_4:\text{Yb}^{3+}$ nanorods,⁷⁶ $(\text{NaLuF}_4:\text{Gd}^{3+}/\text{Yb}^{3+}/\text{Er}^{3+})@/\text{NaLuF}_4:\text{Yb}^{3+}$,⁵⁸ $\text{BaGdF}_5:\text{Yb}^{3+}/\text{Er}^{3+}@/\text{BaGdF}_5:\text{Yb}^{3+}$ nanoparticles,⁷⁷ as well as in $\text{BaF}_2:\text{Ln}^{3+}@/\text{SrF}_2:\text{Ln}^{3+}$ nanoparticles.⁷⁷ We recently reported a significant enhancement of UCPL (~240 times) in cubic $(\text{NaYF}_4:\text{Yb}^{3+}/\text{Tm}^{3+})/\text{NaYbF}_4/\text{NaYF}_4$ active core/active shell/inert shell nanoparticles, using directed energy migration in the second shell layer.⁷⁸ In addition to the suppression of core surface-related quenching, active layer provided enhancement of upconversion through energy transfer from the Yb^{3+} ions-contained in the active-shell to the dopant ions in the core. However, caution has to be exercised when utilizing this strategy, as the introduction of Yb^{3+} into the shell layer at the same time elevates energy-migration induced surface-related quenching mechanism (see section 2.1). An optimized Yb^{3+} concentration in the shell needs to be established. It was shown that the core/shell/shell design of the $(\text{NaGdF}_4:\text{Er}^{3+})@(\text{NaGdF}_4:\text{Ho}^{3+})@/\text{NaGdF}_4$ nanoparticles resulted in enhanced NIR light harvesting due to a combined light harvesting capabilities of both Er^{3+} and Ho^{3+} .⁷⁹ The drawback however is

that high doping concentrations of Er^{3+} and Ho^{3+} may cause adverse cross relaxations, inducing quenching beyond the interfaces, even though the dopants are in different layers. The concept of incorporating lanthanide dopants into distinct layers in the active core/multiple shell structure can provide unprecedented capabilities for nanophotonic control of uncoupled upconversion in each domain (Figure 2 c).

2.2.2. The Shell Containing Organic Dyes

Energy transfer from the electronic manifold of organic dye molecules to lanthanide ions in $\text{NaYF}_4:\text{Yb}^{3+}/\text{Er}^{3+}$ UCNPs has been established to dramatically enhance UC green emission intensity (by a factor of ~ 3300 times) due to a significantly broadened absorption spectral range as well as a greatly increased absorption strength.⁸⁰ The structure can be illustrated using Figure 2 (f); the core is the $\text{NaYF}_4:\text{Yb}^{3+}/\text{Er}^{3+}$ UCNPs to which dye molecules are covalently attached. The organic dye shell will produce an “antenna effect” to sensitize the small sized UCNPs, exploiting three important features: (i) there exists a large amount of lanthanide ions located at or around the nanoparticle surface due to the unique high “surface-to-volume” ratio offered by the nanoscale dimension; (ii) typically, the NIR absorption of a dye molecule is three orders of magnitude more intense than the absorption of a lanthanide ion, and several times broader than its absorption band; (iii) energy transfer from the singlet state of an organic dye to the 4f-4f transition of lanthanide is quantum mechanically allowed *via* a Förster mechanism involving higher-order multipolar interactions (e.g., dipole-quadrupole), or a Dexter mechanism involving double electron exchange.⁸¹ This fact has long been established for lanthanide-coordinated metal complexes.⁸¹ Dye-sensitized upconversion provides a paradigm to broadly harvest NIR light and convert it into visible light. However, the net UCQYs obtained by Zou *et al.* remained relatively low (less than 0.1%),⁸⁰ as the utilized

nanoparticle has a quite poor UC efficiency, and the spectral overlapping between the emission of the organic dye (IR 806) and the absorption of Yb^{3+} ion is extremely limited. Increase of the UCQYs in dye-sensitized UCNPs is an appealing direction.

2.3. Core/Shell Structure to Suppress Cross Relaxation

The cross relaxation process is the main problem for the well-known conventional “concentration quenching effect”, diminishing the luminescence of lanthanides. This loss mechanism is primarily considered for a Stokes-shifted downconversion luminescence, but its impact on the UC luminescent efficiency becomes significant with increase in concentration of the activators, such as Tm^{3+} , Er^{3+} , and Ho^{3+} ions. Moreover, with utilization of several types of lanthanide ion dopants in the same domain, cross relaxation between different types of ions turns into a serious concern. From a fundamental point of view, the cross relaxation process originates from Coulomb interactions between two lanthanide dopant ions which is strongly dependent on the ion-ion distance determined by the dopants concentration in the nanoparticle.¹ Through optimization of the dopants concentration, the cross relaxation process can be minimized; however, the concentration of dopants has to be low, which limits the luminescence efficiency. One solution to this problem is to separate the appropriate lanthanide ions in the core and the shell to create a spatial confinement that can result in a highly efficient UC, reducing detrimental effects of the cross relaxation process (Figure 2 c). For example, the optimized concentration for Er^{3+} ions was determined to be ~2% for $\text{NaYF}_4:\text{Yb}^{3+}/\text{Er}^{3+}$ microsized particles;⁶⁹ this parameter is then typically used in most studies with $\text{NaYF}_4:\text{Yb}^{3+}/\text{Er}^{3+}$ nanoparticles. Recently, Kong and Zhang *et al.* demonstrated that this commonly accepted upper threshold for concentration quenching of Er^{3+} can be raised from 2 to 5% by spatial separation of the emitter doping area inside nanoparticles.⁸² This concept was later exploited by Zhao *et al.* to engineer the

distribution of activators inside one single nanoparticle to enhance upconversion luminescence efficiency. In a comparison with conventional heterogeneous doping, which associates with fluctuations of dopant concentrations inside one nanoparticle, a layer-by-layer deposition of multilayer shells with a defined dopant concentration is able to homogenize the distribution of dopants within one single nanoparticle, thus yielding a two-folds increase in the absolute upconversion yield of $\text{NaGdF}_4:\text{Yb}^{3+}/\text{Er}^{3+}@ \text{NaYF}_4$ UCNPs due to a reduction of cross relaxation -induced quenching effect.⁸³

We exemplified here a recent success of using the concept of suppressing cross relaxation in a core/shell design to shift the typically used excitation wavelength at 980 nm to a more biocompatible wavelength at ~800 nm. A motivation behind this is that a laser at ~980 nm can produce heating to damage biological tissue when long irradiation is involved, due to a noticeable water absorption at this wavelength. At the same time, water is much more transparent for NIR light at 800 nm (Figure 3 a). It was demonstrated that cascade sensitized $\text{Nd}^{3+}/\text{Yb}^{3+}/\text{Er}^{3+}$ (Tm^{3+}) tri-doped ($\beta\text{-NaYF}_4:\text{Ln}^{3+}$)@ $\beta\text{-NaYF}_4$ colloidal UCNPs can shift the typically used excitation at ~980 nm to a ~800 nm.⁸⁴ This system consists of a primary sensitizer (Nd^{3+}), a bridging sensitizer (Yb^{3+}) and an lanthanide emitter Er^{3+} (Tm^{3+}). The Nd^{3+} ions absorb photons at ~800 nm, while the Yb^{3+} ions act as bridge, to receiving the energy from the Nd^{3+} ions and transfer it to the emitters Er^{3+} (Tm^{3+}). The hierarchy of involved energy levels, in conjunction with the interactions of these three lanthanide ions, allows energy to be transported in the way what we described above. A serious problem, existing in this system, is that Nd^{3+} ions exhibit efficient cross relaxation with the emitter Er^{3+} (Tm^{3+}) ion. Overcoming this obstacle (suppressing cross relaxation process) requires the concentration of Nd^{3+} ion to be as low as ~1%, limiting the light absorption ability and, correspondingly, the

upconversion efficiency of this system. Yan *et al.* and Liu *et al.* demonstrated later that doping Nd^{3+} into a shell layer can minimize the cross relaxation process between the Nd^{3+} ions and the emitters (Er^{3+} , Tm^{3+} , Ho^{3+}), while maintaining a high Nd^{3+} ion concentration of $\sim 10\text{-}15\%$.^{85, 86} This is of particular importance for the brightness of the system, as a high concentration of Nd^{3+} not only can increase the absorption of the nanoparticle, but also can increase the cascaded energy transfer efficiency. Indeed, the total UCPL intensity of $(\beta\text{-NaYF}_4:\text{Yb}^{3+}/\text{Er}^{3+})@\beta\text{-NaYF}_4:\text{Nd}^{3+}$ or $(\beta\text{-NaYF}_4:\text{Yb}^{3+}/\text{Tm}^{3+})@\beta\text{-NaYF}_4:\text{Nd}^{3+}$ UCNPs was several tens of times higher than that of $(\beta\text{-NaYF}_4:\text{Nd}^{3+}/\text{Yb}^{3+}/\text{Er}^{3+})@\beta\text{-NaYF}_4$ or $(\beta\text{-NaYF}_4:\text{Nd}^{3+}/\text{Yb}^{3+}/\text{Tm}^{3+})@\beta\text{-NaYF}_4$ nanoparticles, respectively (Figures 3 a and b).⁸⁶ A core/shell design to minimize the cross relaxation process in Nd^{3+} -sensitized systems has also been explored by others, by introduction of a transition layer between the Nd^{3+} -containing layer and the Yb^{3+} -containing layer (Figure 3c) or growth of the anisotropic core/shell structure.⁸⁷⁻⁹⁰ These new core/shell designs resulted in the enhanced upconversion luminescence intensity, more tunable color output, as well as realization of dual modal upconversion and downconversion bioimaging. However, the absolute quantum yield of UCPL for the reported Nd^{3+} -sensitized core/shell nanoparticles remains either unevaluated or rather low. The UCPL at ~ 540 nm from the quenching-shielded sandwich structured UCNPs with Er^{3+} (Figure 3c), that seems to outperform most of the current Nd^{3+} -sensitized core/shell UCNPs, was characterized by UCQY of $0.11 \pm 0.05\%$ under excitation at 800 nm (20 W/cm^2),⁸⁹ which is much lower than the highest UCQY (5%) reported for $\text{Yb}^{3+}/\text{Er}^{3+}$ -doped core/shell nanoparticles when excited at 980 nm (but with higher power density of 127 W/cm^2).⁶¹

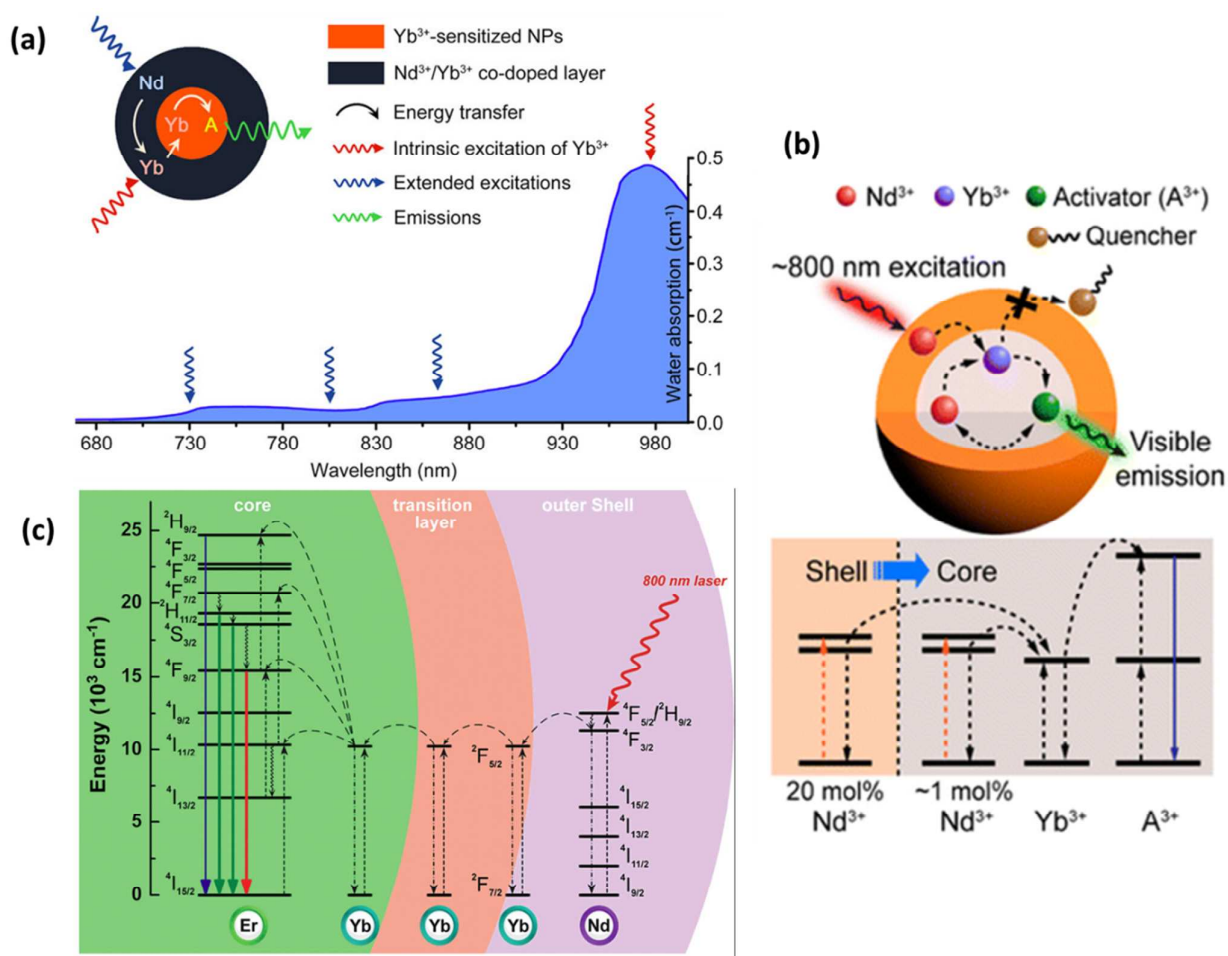


Figure 3. (a) Absorption spectrum of water in range of 680-1000 nm and the core/shell design of $\text{NaYF}_4:\text{Yb}^{3+}/\text{A}^{3+}@\text{NaYF}_4:\text{Nd}^{3+}/\text{Yb}^{3+}$ ($\text{A} = \text{Tm}, \text{Er}, \text{Ho}$); (b) Core/shell design for $\text{NaYF}_4:\text{Nd}^{3+}/\text{Yb}^{3+}/\text{A}^{3+}@\text{NaYF}_4:\text{Nd}^{3+}$; (c) Illustration of involved lanthanide energy levels of a core/shell design of $\text{NaYF}_4:\text{Yb}^{3+}/\text{Er}^{3+}@\text{NaYF}_4:\text{Yb}^{3+}@\text{NaYF}_4:\text{Nd}^{3+}$ with a transition layer to create a larger distance between Nd^{3+} and Er^{3+} ions. All design are based on the cascaded energy flow $\text{Nd}^{3+} \rightarrow \text{Yb}^{3+} \rightarrow \text{A}^{3+}$ ($\text{A}=\text{Er}$ or Tm) (excited at ~ 800 nm). The deleterious cross relaxation between Nd^{3+} and A^{3+} ($\text{A}=\text{Er}$ or Tm) in (a)-(c) is minimized by spatial isolation of the lanthanide dopants into the core domain as well as into the shell domain. In (b), a very limited concentration of Nd^{3+} (1 mol%) is employed to minimize the cross relaxation process, still enhancing energy transfer across the interface. Reproduced with permission from refs. 85, 86, and 89. Copyright 2013 American

Chemical Society. Copyright 2014, John Wiley and Sons.

2.4. Core/Shell to Nanoscopically Control Energy Transfer

Nonradiative energy transfer from the excited states of lanthanide ions plays vital roles in all pertinent UC luminescence phenomena; the ability to precisely control its direction and rate has numerous manifestations in academic interests as well as in technological applications. The main source of nonradiative energy transfer arises from the fundamental multipolar and/or exchange interactions between two lanthanide ions. In general, the energy transfer probability for electric multipolar interactions is proportional to the inverse of the s^{th} power of the ion-ion distance: for dipole-dipole ($s=6$), dipole-quadrupole ($s=8$), and quadrupole-quadrupole ($s=10$) interactions.^{1, 19} The exchange interaction is falling even on a shorter distance, exponentially with the separation distance of ions, as it requires the overlap between wave functions of two ions.⁸¹ This strong dependence of multipolar/exchange interactions on the ion-pair distance at the nanoscale provides an opportunity to use the control of nanostructure to optimize the ion-pair interaction. In particular, the demonstrated ability to control the shell layer thickness with the monolayer accuracy provides a method to manipulate the energy transfer at a nanoscale (see section 3.2), in conjunction with a rational alignment of energy levels in different shell layers. This manipulation of energy transfer between different lanthanide dopants has been implemented in ~ 10 nm LaF_3 based core-shell nanostructures, where the core domain contains the Eu^{3+} dopant, the first layer is an inert LaF_3 , the active second layer contains the Tb^{3+} dopants, and the third layer is an inert LaF_3 .⁹¹ The core/shell structure is similar to Figure 2 (c), with the difference that the 4th and the 5th layers do not exist. It is found that by varying the thickness of the undoped first layer between the Tb^{3+} -doped layer (the second layer) and the Eu^{3+} -doped layer (the core domain), the degree of energy transfer can be engineered to allow

for zero, partial, or full energy transfer from a donor ion (Tb^{3+}) to an acceptor ion (Eu^{3+}). Chen *et al.* illustrated a general strategy to achieve the dual-mode luminescence of Eu^{3+} in $(\text{NaGdF}_4:\text{Yb}^{3+}/\text{Tm}^{3+})/\text{NaGdF}_4:\text{Eu}^{3+}$ core/shell nanoparticles that involves a controlled use of energy migration.⁵³ Another example is provided by Liu *et al.* who prepared $\text{NaGdF}_4:\text{Yb}^{3+}/\text{Tm}^{3+} @\text{NaGdF}_4 @\text{NaGdF}_4:\text{Tb}^{3+}$ core/shell/shell nanoparticles with varied NaGdF_4 shell thickness to show that the excitation energy can travel through the Gd^{3+} sub-lattice for a substantial distance of over 5 nm, without energy losses.¹²

Wang *et al.* reported on light management through a directed energy transfer in a $\text{NaYbF}_4 @\text{Na}(\text{Yb},\text{Gd})\text{F}_4 @\text{NaGdF}_4$ core/shell/shell nanoparticles, where different types of lanthanide dopants were doped into different domains (Figure 3).⁸⁷ To manage the energy level for favorable energy flow, Nd^{3+} were doped into the core domain to harvest light excitation at ~ 800 nm, $\text{Yb}^{3+}/\text{X}^{3+}$ ($\text{X}=\text{Er}, \text{Ho}, \text{Tm}$) were doped into the inner shell domain to produce colored upconversion emission, while the Z^{3+} ($\text{Z}=\text{Eu}, \text{Tb}, \text{Dy}$) were doped into the outmost shell domain to additionally tune the upconversion luminescence. Through the Yb^{3+} sub-lattice network, the harvested energy by Nd^{3+} ions can transfer to the emitter X^{3+} ($\text{X}=\text{Er}, \text{Ho}, \text{or Tm}$) in the inner shell domain. The Gd^{3+} ion has long been known as a good sensitizer for Eu^{3+} , Tb^{3+} , Dy^{3+} and Sm^{3+} when excited in the UV range,^{92, 93} which can also be activated through $\text{Yb}^{3+}/\text{X}^{3+}$ ($\text{X}=\text{Tm}, \text{Er}, \text{or Ho}$) pairs through a five- or six-photon UC process when excited at ~ 980 nm.⁹⁴⁻⁹⁶ However, UC emission in the UV range from the $\text{Yb}^{3+}/\text{Tm}^{3+}$, which is much more intense than UCPL from $\text{Yb}^{3+}/\text{Er}^{3+}$ or $\text{Yb}^{3+}/\text{Ho}^{3+}$ ion pairs, typically results in activation of Gd^{3+} ions with significantly higher efficiency. Because of the unique large energy gap of Gd^{3+} (~ 32000 cm^{-1}), the absorbed energy can be contained and migrate in the Gd^{3+} sub-lattice network, crossing the core/shell interface to reach the Z^{3+} ($\text{Y}=\text{Eu}, \text{Tb}, \text{or Dy}$) sites.

As a result, if the Tm^{3+} ions are selectively doped, the energy in the high-lying excited state of Tm^{3+} can be transferred to the migrator ions (Gd^{3+}), then to the emitters Z^{3+} ($\text{Y} = \text{Eu}, \text{Tb}, \text{or Dy}$) and be released as luminescence. The color tunability is provided by the electronic structure of Eu^{3+} , Tb^{3+} , or Dy^{3+} which are excited through this energy migration process. The issue of surface-related quenching mechanism in this system is addressed by growing an inert shell NaYF_4 .⁹⁷ It can be concluded that the nanoscopic control of energy transfer in hierarchical core/multishell nanoparticles opens a new realm for control upconversion, by tailoring the absorption wavelength, extinction coefficient, UCPL wavelength, lifetime and efficiency.

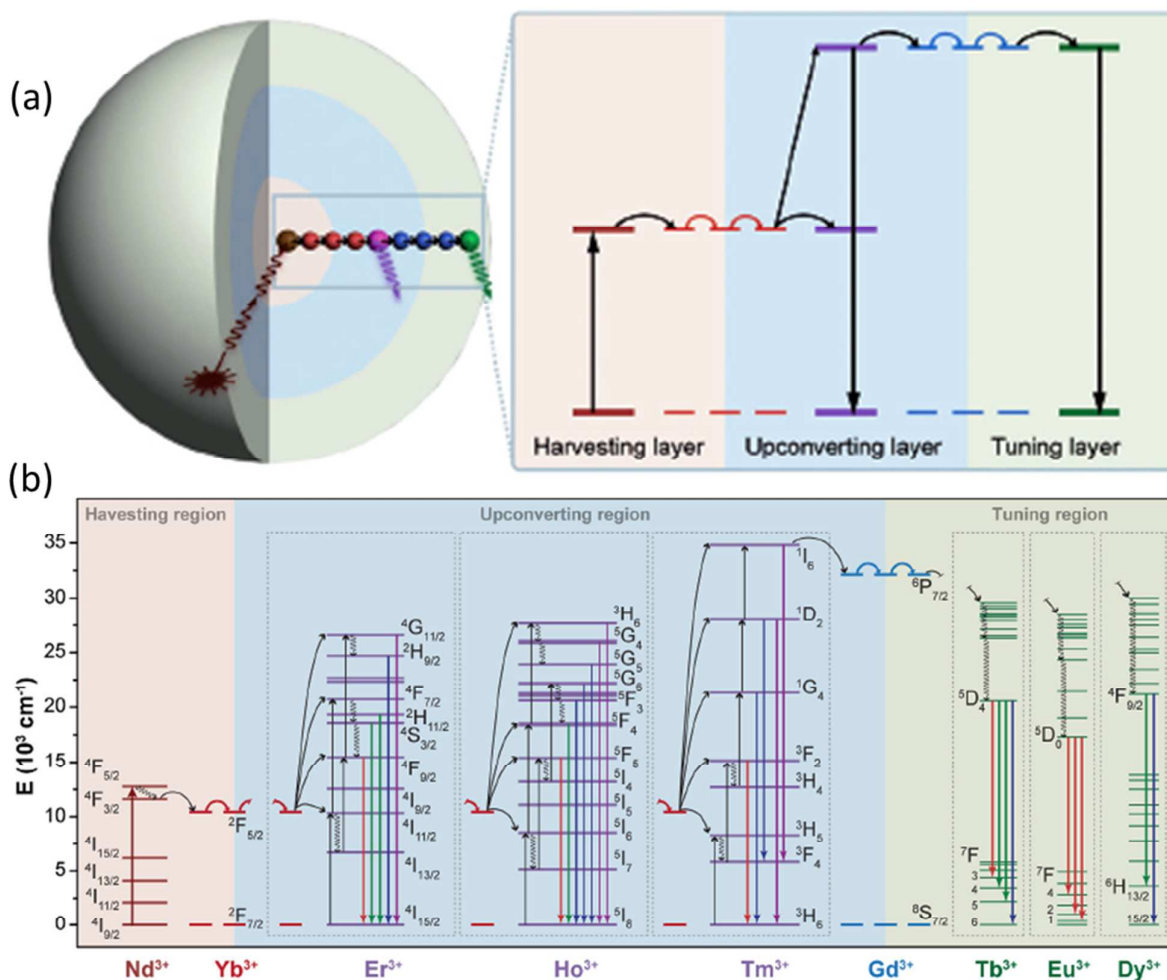


Figure 4. (a) Schematic illustration of the principle of energy flow in a $\text{NaYbF}_4@(\text{Yb,Gd})\text{F}_4@(\text{NaGdF}_4)$ core/shell/shell structure. (b) The corresponding energy levels of Nd^{3+} doped in the core domain, $\text{Yb}^{3+}/\text{X}^{3+}$ ($\text{X}=\text{Er, Ho, Tm}$) in the inner shell, as well as the Z^{3+} ($\text{Y}=\text{Eu, Tb, or Dy}$) ions in the outmost shell. The involved upconversion mechanisms (absorption, energy migration and flow, as well as the luminescence are shown. Reproduced with permission from ref. 87. Copyright 2013, John Wiley and Sons.

2.5. Core/Shell Structure to Tune Color of Upconversion Emission

2.5.1. A Combinatory of Spatially Isolated Lanthanide Ions

The use of a core/shell architecture with two or more lanthanide activators incorporated into the core and different shells is a typical strategy to tune the luminescence of UCNPs, while maintaining a high luminescence efficiency. This strategy also explores different combinations of lanthanide activators to produce multicolor emission and exercises a spatial isolation of these lanthanide activators using an appropriate core/shell structure. It eliminates deleterious cross relaxation between the lanthanide activators and suppresses surface-related quenching mechanism in the core nanoparticles, thus yielding a range of tunable emission with high efficiency.

Lanthanide emitters (activators) of Er^{3+} , Tm^{3+} , Ho^{3+} , and Pr^{3+} ions have long-lived intermediate states, which typically can be sensitized by Yb^{3+} ions to produce efficient UC emission when excited at ~ 980 nm. The use or combined use of these activators with precisely controlled concentration is able to produce three primary UC colors (blue, green, and red) and a range of UC outputs with other colors, even a white light output. Doping two or more of these activators into one single domain is a straight forward way to tune the UC output, but does often introduce the deleterious cross relaxation process resulting in a decrease in the UC intensity. Core/shell structured UCNPs can minimize this

cross relaxation process (see section 2.3 and Figure 2c) while retaining the color tunability through spatial confinement of the emitters. Zhang *et al.* reported on hexagonal-phase $\text{NaYF}_4:\text{Yb}^{3+}/\text{Tm}^{3+}@\text{NaYF}_4:\text{Yb}^{3+}/\text{Er}^{3+}$ and $\text{NaYF}_4:\text{Yb}^{3+}/\text{Tm}^{3+}@\text{NaYF}_4:\text{Yb}^{3+}/\text{Er}^{3+}@\text{NaYF}_4:\text{Yb}^{3+}/\text{Tm}^{3+}$ core/shell nanoparticles to produce multiple emission peaks.⁹⁸ Emissions from both Tm^{3+} and Er^{3+} in these UCNPs were shown to be non-quenched, in contrast to the UCPL from $\text{Tm}^{3+}/\text{Er}^{3+}$ -codoped NaYF_4 nanoparticles. A range of sandwich-structured core/shell/shell nanoparticles of $\text{NaYF}_4:\text{Yb}^{3+}/\text{Er}^{3+}@\text{NaYbF}_4:\text{Tm}^{3+}@\text{NaYF}_4:\text{Yb}^{3+}/\text{Tm}^{3+}$, $\text{NaYF}_4:\text{Yb}^{3+}/\text{Tm}^{3+}@\text{NaYbF}_4:\text{Er}^{3+}@\text{NaYF}_4:\text{Yb}^{3+}/\text{Er}^{3+}$, and $\text{NaYF}_4:\text{Yb}^{3+}/\text{Tm}^{3+}@\text{NaYbF}_4:\text{Er}^{3+}@\text{NaYF}_4:\text{Yb}^{3+}/\text{Tm}^{3+}$ UCNPs have also been developed, exhibiting tunable UC emissions for multicolor cellular imaging.⁹⁹ Ultrasmall UCNPs with hierarchical core/shell/shell architecture ($\text{NaGdF}_4:\text{Yb}^{3+}/\text{Tm}^{3+}@\text{NaGdF}_4:\text{Yb}^{3+}/\text{Er}^{3+}@\text{NaGdF}_4$) have been prepared following a microwave-based thermolysis procedure, producing upconversion emission with the color output tuned by varying the position of the dopants inside the nanoparticles (Figure 5).¹⁰⁰

Lanthanide emitters like Eu^{3+} , Tb^{3+} , Dy^{3+} and Sm^{3+} , which do not have long-lived intermediate energy states, can only be directly excited at NIR light through a simultaneous multi-photon absorption process or a cooperative sensitization upconversion (CSU) process via simultaneous extraction of the energy contained in an excited Yb^{3+} ion pair. These lanthanide ions can be utilized for tuning upconversion through nanoscopic control of energy migration in core/multishell structures (see section 2.4).

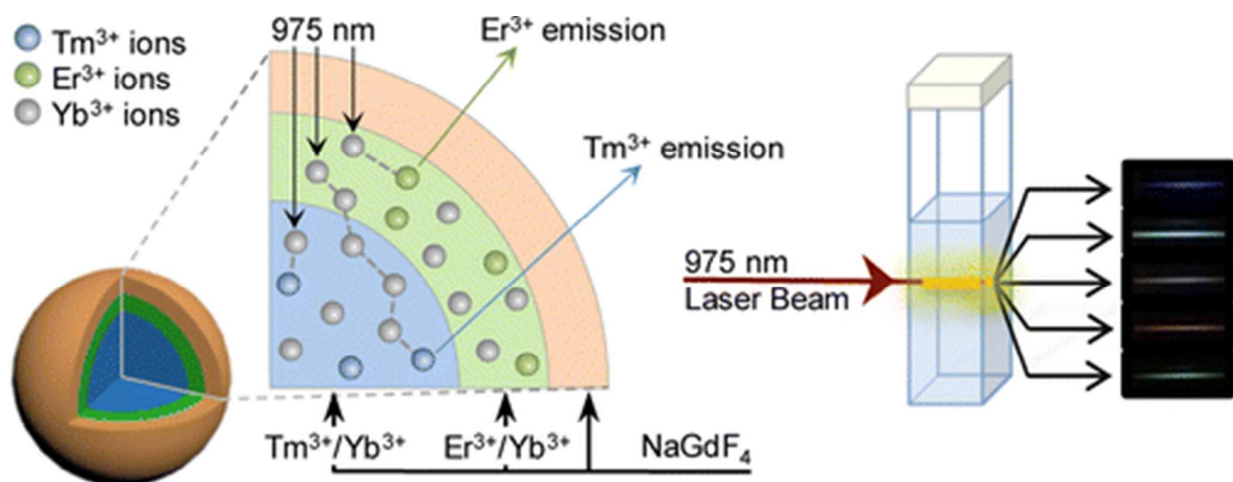


Figure 5. Tuning upconversion luminescence using ultrasmall core/shell/shell NaGdF₄:Yb³⁺/Tm³⁺@NaGdF₄:Yb³⁺/Er³⁺@NaGdF₄ architectures. Reproduced with permission from ref. 100. Copyright 2014, American Chemical Society.

2.5.2. Tuning Upconversion through Energy Transfer

Energy transfer from donor to acceptor can involve two pathways: 1) nonradiative energy transfer *via* multipolar or exchange interactions; 2) radiative energy transfer, *i.e.*, luminescence resonance energy transfer (LRET), where light emitted by the donor is absorbed by an acceptor molecule. When utilizing the UCNPs as an energy donor and dyes or quantum dots (QDs) as an energy acceptor, it offers a larger freedom for upconversion emission wavelengths than for the UCPL produced merely by the lanthanide ions. An expanded range of multicolor emission was obtained from the core/shell NaYF₄:Yb³⁺/Er³⁺(Tm³⁺)@silica nanostructures by encapsulating organic dyes or QDs into the silica shell to produce additional luminescence via nonradiative energy transfer or LRET processes (Figure 6a).¹⁰¹ Alternatively, one or more bands of the UC emission from either NaYF₄:Yb³⁺/Er³⁺ or NaYF₄:Yb³⁺/Tm³⁺ nanoparticles can be selectively quenched by organic

luminescence quenchers or gold nanoparticles contained in the shell layer to produce a tunable color-coded output (Figure 6b).¹⁰²

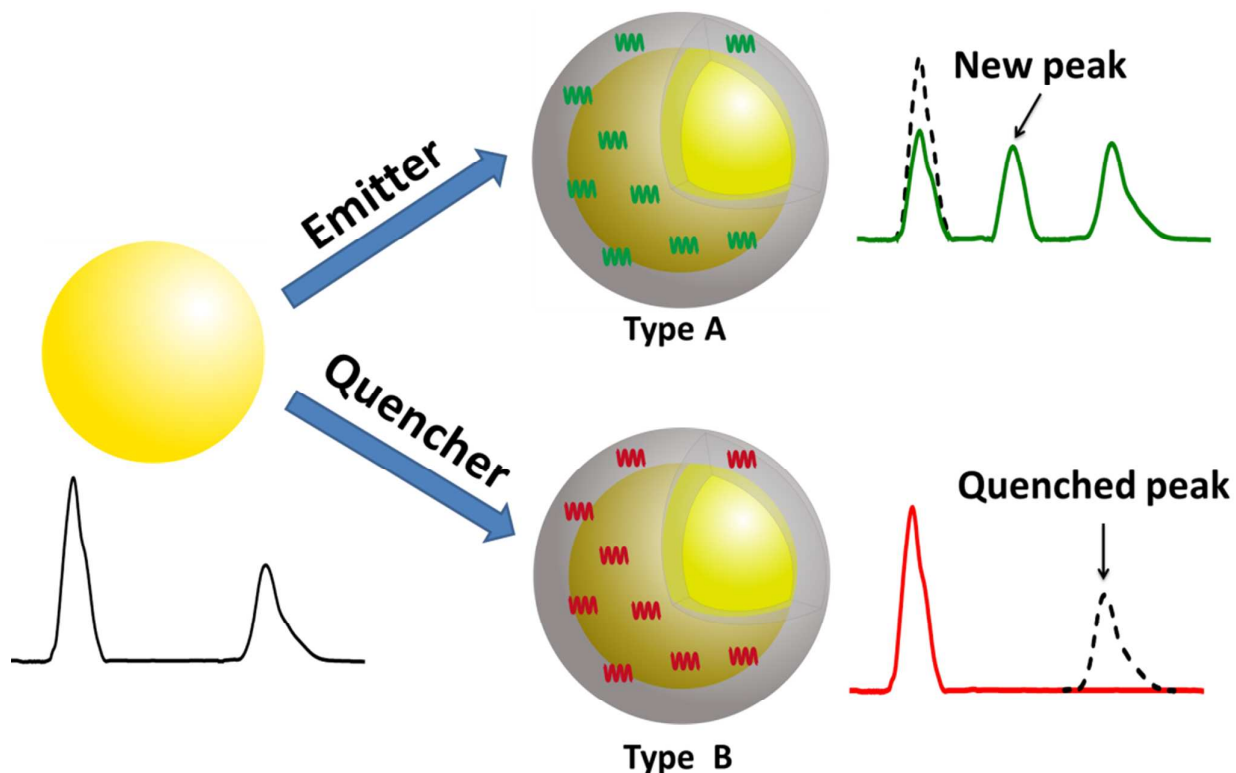


Figure 6. Schematic illustration of tuning upconversion luminescence using non epitaxial UCNPs/silica core/shell structure, where (a) luminescent emitters and (b) luminescent quenchers are loaded in the silica shell.

2.6. Core/Shell UCNPs for Coupling with Localized Surface Plasmon

Localized surface plasmon resonance (LSPR) is a collective oscillation of free charge carriers at the interface of metallic or self-doped semiconductor nanomaterials and dielectric medium; LSPR is generated by incident light when the resonance occurs between frequency of light photons and the natural frequency of surface charge carriers. The plasmon resonant frequency for plasmonic nanostructures is revealed itself as a maximum in optical absorption spectrum (typically in visible

and close NIR ranges for Au and Ag metallic nanostructures).^{19,33} In anisotropic nanostructures such as nanorods, LSPR along the longitudinal direction can be tuned over a wide range by changing the aspect ratio.¹⁰³ The LSPR is able to greatly enhance the electromagnetic field near the particle's surface, which falls off rapidly with distance from the surface. This enhanced field produces an increase in the emission efficiency of an emitter located near the surface of the plasmonic nanostructure.¹⁰⁴ However, coupling to structures with LSPR can also affect the emission in a different way. Close contact of the emitter with the metallic surface introduces large non-radiative decay, resulting in a drastic quenching of emission.¹⁰⁵ That is why the distance between the emitter and the plasmonic nanostructure has to be optimized to obtain the plasmonic enhancement of emission. This optimization can be facilitated by using a core/shell type architecture (Figure 2 e). LSPR has been used to enhance the efficiency of the UCPL of UCNPs involving a large variety of configurations.¹⁰⁶⁻¹¹²

Among the reported work, core/shell nanostructures of metallic@silica@UCNPs or UCNPs@silica@metallic (refer to Figure 2 e for schematic configuration) are of particular importance, as they provide a single platform to couple LSPR and UCPL at the nanoscale. The distance between the metallic nanoparticles and the UCNPs can be precisely controlled to achieve the optimum enhancement of UCPL by varying the thickness of the spacer silica shell. A number of previous reports have used silica layer as a spacer,^{35, 113-118} but some work showed plasmonic-induced UCPL quenching.¹¹⁹⁻¹²¹ Time-resolved measurements did reveal that the emission process is influenced in both cases. The reported enhancements vary widely and the exact enhancement mechanisms are not clearly understood. The plasmonically induced enhancement is generally more pronounced for a multiphoton-induced UCPL band and at a low excitation power

density, when saturation effects are not in play. Detailed measurements and analysis of the enhancement factors for different UCPL bands are necessary to establish the enhancement mechanism, along with theoretical guidance to produce optimized plasmonic structures of appropriate shape, size and situated at an optimum distance from the UCNPs. Lu *et al.* in their recent study “Plasmon Enhancement Mechanism for the Upconversion Processes in NaYF₄:Yb³⁺/Er³⁺ Nanoparticles: Maxwell versus Förster” compared UCPL from NaYF₄:Yb³⁺/Er³⁺ UCNPs deposited on a silver nanograting and that from the ones on a flat silver film, and has shown that the intensity of the green and red UCPL (Er³⁺ emission) on the nanograting was up to 16 and 39 times higher.¹²² The UCPL intensity was found to depend quadratically on the excitation power in the weak excitation power limit and linearly in the strong excitation power limit. Importantly, the authors identified and separated two main mechanisms contributing to plasmon enhancement of luminescence upconversion: absorption of lanthanide ions and energy transfer between them. The absorption enhancement is described by the Maxwell's equations, while the energy transfer obeys the Förster's theory. It was further determined that the absorption enhancement played the dominant role, while the energy transfer enhancement was small and effective only in the weak excitation regime. The expressions for the overall enhancement factors for the upconverted luminescence intensity in the weak and strong excitation limits were derived. It can be assumed that the work of Lu *et al.* sheds light on how surface plasmon enhances the upconversion in lanthanide ions materials and may allow comparison among the widely varying reports in the literature, thus offering a foundation for more advanced engineering of plasmon enhanced upconversion materials.

2.7. Core/Shell UCNPs for Introducing New Functionalities

This section provides an account of integration of various functionalities on a single UCNP platform

using a core-shell architecture, which can be of great value for biomedical applications. Appropriate tailoring of this core/shell nanoplatform is able to produce multifunctionality, either minimizing interference between incorporated functionalities or to the contrary bringing synergy of interaction between them. These functionalities can be utilized for biomedical imaging, sensing, various applications in diagnostics or therapeutics. An important new direction is to entail these core/shell structures for theranostics applications, whereby both diagnostic and therapeutic functions are combined.

2.7.1 New Imaging Modality

Biomedical imaging has become one of the most relied-upon tools in life sciences and healthcare. It embraces optical imaging, magnetic resonance imaging (MRI), computed tomography (CT), positron emission tomography (PET), single-photon emission computed tomography (SPECT), and photoacoustic (PA) imaging.¹²³ A nanoparticle platform for imaging contrast agents may allow for complementary use of the existing imaging techniques and for a development of novel imaging methods, that can lead to early detection, screening, diagnosis, and image-guided treatment of human diseases. The core/shell structure enables incorporation of appropriate imaging modalities into the core as well as in different shell layers (Figure 2 c), without interference between them (refer to the advantages of core/shell architecture discussed in 2.1-2.6).

An epitaxial core/shell structure with the shell containing magnetic elements (Gd^{3+} , Dy^{3+} , Mn^{2+} , and Ho^{3+} ions) is able to produce a new MRI imaging modality without or with limited influence on UCPL from the core.^{124-126 127-129} For example, “smart” lanthanide-based theranostic $\text{NaDyF}_4:\text{Yb}^{3+}/\text{NaGdF}_4:\text{Yb}^{3+}/\text{Er}^{3+}$ core/shell nanoprobles are able to circumvent the up-converting poisoning effect of Dy^{3+} ions to produce efficient up-conversion fluorescence, while offering not

only excellent dark T₂-weighted MR contrast, but also tunable bright and dark T₁ MR contrasts properties.¹²⁹ Core-shell Fe₃O₄@NaYF₄:Yb³⁺/Er³⁺ nanocomplexes has been prepared for T₂-weighted magnetic resonance and upconversion luminescence imaging.¹³⁰ An epitaxial core/shell structure with high X-ray attenuation element (e.g., Lu³⁺ or Yb³⁺) in either in the core or in the shell offers a new modality for CT imaging,^{131, 132} while positioning the radionuclide ¹⁵³Sm in the outmost shell layer allows for SPECT imaging¹³³ or the ¹⁸F radionuclide for PET imaging.¹³⁴ Recent progresses on use of core/shell hierarchical design for multimodal imaging applications are discussed in Section 5.1.2.

2.7.2 Therapeutic Functionality

In general, the UCNPs themselves lack the functionality to produce a therapeutic effect. A pertinent effect using lanthanide-doped nanoparticles (not UCNPs) is demonstrated by Streck *et al.* where high concentration Nd³⁺ containing NaYF₄ is able to provide a local temperature increase when excited at ~532 nm, potentially having applications in photothermal therapy (PTT).¹³⁵ A silica coating of UCNPs (Figure 2 d) provides possibilities to incorporate various therapeutic functionalities into the UCNPs.^{136, 137} The importance of silica coating resides in that it can be produced with controllable porosity, which provides promise for therapeutic loading and controlled release. The controlled release can take place in a sustained way via slow diffusion through voids or channels in the silica,^{138, 139} or activated by UV upconversion light by the action of a NIR light penetrating deep through a biological medium.¹⁴⁰ Silica also has a well-developed surface chemistry to introduce a variety of plasmonic nanomaterials (e.g., metallic nanoshells, metallic nanoparticles, self-doped plasmonic semiconductors) on to them, thus providing abilities to implement photothermal therapy (PTT) and/or photoacoustic imaging using silica coated UCNPs. Indeed, silica coating imparts a large

variety of therapeutic functions to UCNPs, entailing them to be used as theranostic core/shell UCNPs. Use of polymeric coating instead of silica to incorporate various therapeutic functions is also being actively pursued.¹⁴¹ In addition, $\text{NaYF}_4:\text{Yb}^{3+}/\text{Tm}^{3+}@/\text{TiO}_2$, $\text{NaLuF}_4:\text{Yb}^{3+}/\text{Tm}^{3+}/\text{Gd}^{3+}@/\text{TiO}_2$, $\text{NaYF}_4:\text{Yb}^{3+}/\text{Er}^{3+}@/\text{Bi}_2\text{MoO}_6$ core-shell nanoparticles have been prepared which show excellent NIR-driven photocatalytic activity as a result of using upconversion luminescence to activate TiO_2 photocatalyst positioned in the shell.¹⁴²⁻¹⁴⁴ The ability to produce reactive oxygen species (ROS) or free radicals from a TiO_2 shell layer shows promises for the use of these core/shell structures as attractive pro-drugs for NIR light-activated therapy. This potential has recently been verified in an study where the amount of ROS produced from $\text{NaYF}_4:\text{Yb}^{3+}/\text{Tm}^{3+}@/\text{TiO}_2$ nanoparticles was shown to be sufficient for killing cancer cells *in vitro*.¹⁴⁵ The use of varied types of core/shell structure for therapeutic applications is discussed in sections 5.1.3 and 5.1.4.

3. Preparation of Hierarchical Core/ Shell Upconversion Nanoparticles

Use of nanophotonic approaches to control the excitation dynamics of upconversion in a core/shell structure significantly relies on the ability of nanochemistry to produce shells in a precisely defined manner. This is of particular importance for epitaxial core/multishell upconversion nanoparticles, as each shell may play a specific distinct role. This means that host lattice, thickness, crystal structure, as well as concentration and type of dopants might vary in different shell layers, yet the entire multishell coating has to be grown in a well-defined manner. This section provides an account of nanochemical approaches to prepare these epitaxial core/shell structures with single or multiple shell layers with monolayer deposition precision, as well as to synthesize non-epitaxial mesoporous silica coated UCNPs and plasmonic core/shell nanoparticles. The core only UCNPs have been typically prepared using solution-based colloidal nanochemistry via three main types of synthetic approaches:

(i) *Thermal Decomposition*. (ii) *Ostwald-Ripening*, and (iii) *Hydrothermal method*. By carefully adjusting experimental parameters, such as concentrations of precursors, type of solvents, reaction temperature and time, the core only UCNPs with a high crystallinity, narrow size distribution and exceptional optical properties can be prepared. As this nanochemistry has been thoroughly presented by us as well as by others in recent reviews,^{2, 17, 146, 147} they are not discussed in this work.

3. 1 General Nanochemical Approaches to Prepare Epitaxial Core/ Shell UCNPs with Single Shell Layer.

Three techniques have been typically used to produce a single shell layer on the core nanoparticle surface.

(i) *Seed-Mediated Epitaxial Growth*. This is the most widely used chemistry to prepare high quality epitaxial core/shell structure nanoparticles with a uniform morphology and size. The essence in a preparation of the high quality inorganic nanoparticles with a narrow size distribution is to well separate the nucleation stage and the growth stage in time.¹⁴⁸ As a result, “burst nucleation” is typically required in the growth solution to produce abundant nuclei that can then be utilized to direct the deposition of the monomer in the growth stage, but without generating new nuclei for new nanocrystals to form (for the case of synthesis of lanthanide-doped nanoparticles by thermolysis method).^{42, 93, 149} In case of UCNPs, the monomer can be defined as the minimal subunit of the host bulk crystal. For seed-mediated epitaxial growth, the core nanoparticles are utilized as “nuclei” for seeding the growth of the shell layer. As the core UCNPs have been prepared before the growth, the nucleation and the growth stages are therefore automatically separated ensuring high quality core/shell nanoparticle to be formed. Seed-mediated growth applies to both homogenous and heterogeneous core/shell UCNPs discussed in section 2; the only difference is in the variance of shell

precursors used in the growth solution. However, in order to create a homogenous interface between the core and the outer shell, the host lattice of the shell material is required to exhibit a low lattice mismatch with the core material. Moreover, the concentration of shell precursor is typically low in regard to the concentration of the core nanoparticles to avoid formation of new nuclei by shell precursors, that might then evolve into nanoparticles of shell host material alone rather than the core/shell UCNPs. The thickness of the shell can be controlled via adjusting the shell precursor concentration, which can be determined according to chemical stoichiometric calculation. In addition, the shell precursors can be either directly injected into the growing solution of the core nanoparticles to induce a further growth of the shell, or the core nanoparticles can be centrifuged out, and the shell layer is grown in a separate step. These two variants of loading shell precursors also provide two alternatives for layer-by-layer growth of core/multishell structure UCNPs as described in section 3.2.

(ii) Seed-Mediated Ostwald-Ripening. Ostwald ripening refers to the process which favors larger particles with smaller surface to volume ratios over the energetically less stable smaller particles, resulting in the growth of larger particles at the expense of smaller ones. As a result, the Ostwald ripening process is able to dissolve energetically less stable small sacrificial nanoparticles into molecules of shell materials, which can then deposit on the larger stable core nanoparticles. Veggel and co-workers recently exploited this process to perform layer-by-layer shell growth onto larger core nanoparticles.⁴⁷ Small sacrificial alpha-NaYF₄ nanoparticles were firstly synthesized used as the shell precursor. Subsequent injection of these sacrificial nanoparticles into a hot solution of NaYF₄:Ln³⁺ core nanoparticles induces a rapid dissolution of the sacrificial nanoparticles and their deposition onto the larger core NPs (self-focusing Ostwald-ripening process), which resulted in a

formation of the core/shell structured nanoparticles with a well-defined shape, narrow size distribution, with control to provide a tunable shell growth. Thus, the shell thickness can be precisely controlled by manipulating the amount of the injected sacrificial nanoparticles. This method is flexible and holds promise to prepare other high-quality homogeneous and heterogeneous core/shell nanoparticles.

(iii) Cation Exchange Reaction. This strategy involves a reversible chemical reaction between an insoluble solid and a solution, during which cationic ions are interchanged. As a result, cationic ions from the surface of UCNPs are replaced by other cations present in solution, thus producing a unique heterogeneous core/shell structure. One of the earliest examples of use of this technique was the preparation of $\text{GdF}_3@\text{LnF}_3$ core/shell NPs by Veggel and Dong.¹⁵⁰ They exposed the GdF_3 core NPs to an aqueous solution containing excess Ln^{3+} ions and observed a partial replacement of Gd^{3+} ions in the GdF_3 NPs by Ln^{3+} from the solution. The same group used the cation exchange approach to prepare multifunctional $\text{NaYF}_4:\text{Yb}^{3+}/\text{Tm}^{3+}@\text{NaGdF}_4$ core/shell NPs with tunable shell thickness, enhanced UCPL and outstanding paramagnetic performance.¹²⁷ More recently, Wang and Deng reported on in situ cation exchange of hexagonal phase $\text{NaYF}_4:\text{Yb}^{3+}/\text{Er}^{3+}$ nanoparticles with Gd^{3+} ions during synthesis, which retained the small particle size of ~ 12 nm, but increased the UCPL by about 29 times.¹⁵¹ However, extended use of the cation exchange method to prepare core/multishell UCNPs is problematic, as it is ineffective to precisely control the exchanging parts of UCNPs and yield a uniform shell. Notwithstanding, it still provides a versatile alternative to impart new imaging modality to UCNPs through the formation of a core/shell structure.

3.2. Layer-by-Layer Approach to Prepare Core/Multishell UCNPs with Monolayer Thickness Precision.

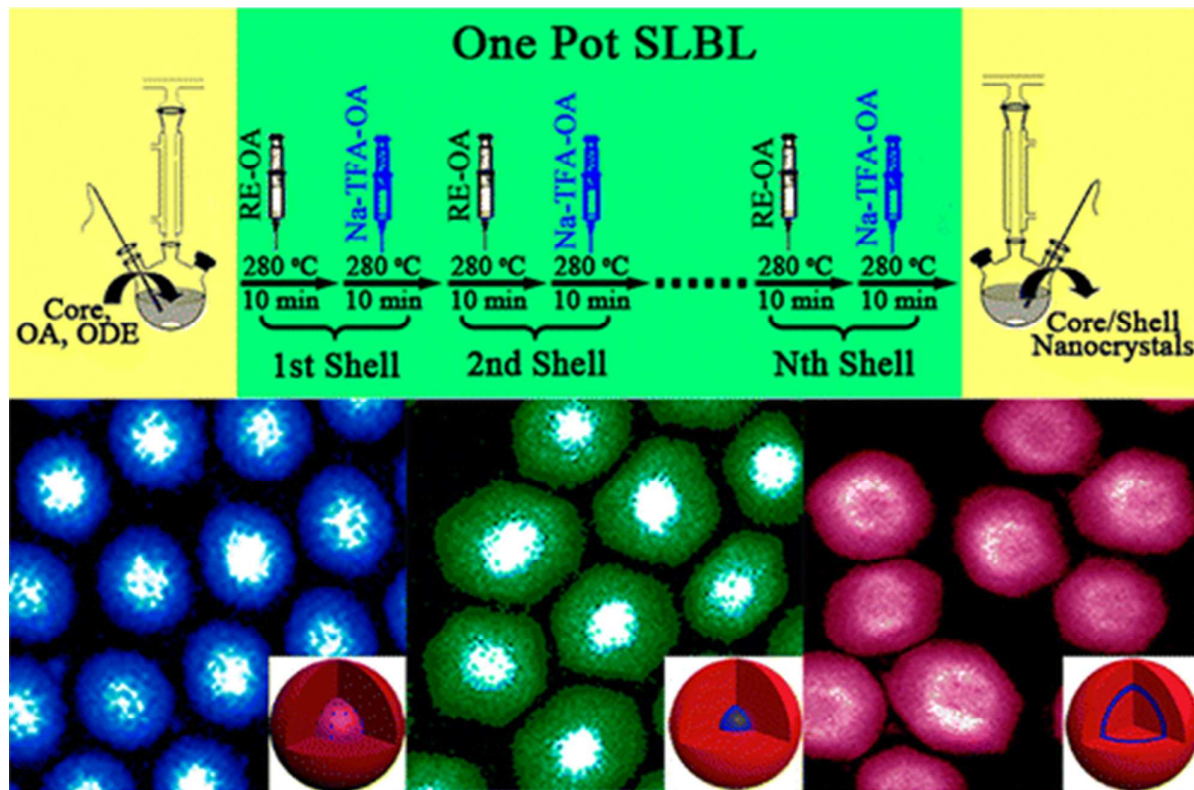


Figure 7. Schematic illustration of one pot successive layer-by-layer (SLBL) deposition to prepare epitaxial core/multishell UCNPs (upper panel), and HAADF STEM images of particles with varied shell thickness (lower panel). Reproduced with permission from ref. 152. Copyright 2013, American Chemical Society.

The chemistry to produce core/multishell UCNPs relies on the deposition of shells in a layer-by-layer way. A straightforward approach is to use a multi-step approach to prepare each shell using seed-mediated epitaxial growth or seed-mediated Ostwald-Ripening methods described above in section 3.1. That is to say the core/1st shell UCNPs is utilized as the seeds for the core/1st shell/2nd shell UCNPs, which are in turn utilized as the seeds for the core/1st shell/2nd shell/3rd shell UCNPs, and then so forth. The stoichiometric nature of involved chemical reactions producing a shell causes its thickness to be precisely proportional to the shell precursor dosage, which can be calculated

according to the increase in molar mass caused by deposition of the shell of a defined thickness. This essentiality provides an exciting opportunity to deposit each shell layer with a single monolayer precision. A multi-step method has been employed by many researchers to prepare core/multishell UCNPs, such as $\text{NaYF}_4:\text{Yb}^{3+}/\text{Er}^{3+}@ \text{NaYbF}_4:\text{Tm}^{3+}@ \text{NaYF}_4:\text{Yb}^{3+}/\text{Tm}^{3+}$,⁹⁹ $\text{NaGdF}_4:\text{Yb}^{3+}/\text{Tm}^{3+}@ \text{NaGdF}_4:\text{Yb}^{3+}/\text{Er}^{3+}@ \text{NaGdF}_4$,¹⁰⁰ $\text{NaYbF}_4@ \text{Na}(\text{Yb},\text{Gd})\text{F}_4@ \text{NaGdF}_4$,⁸⁷ $\text{NaGdF}_4:\text{Yb}^{3+}/\text{Tm}^{3+}@ \text{NaGdF}_4@ \text{NaGdF}_4:\text{Tb}^{3+}$,¹² $\text{NaYF}_4:\text{Yb}^{3+}/\text{Er}^{3+}@ \text{NaYF}_4:\text{Yb}^{3+}@ \text{NaYF}_4:\text{Nd}^{3+}$ (Zhong, *Adv Mater*, *Nd*),⁸⁹ $(\text{NaGdF}_4:\text{Er}^{3+})@(\text{NaGdF}_4:\text{Ho}^{3+})@ \text{NaGdF}_4$,⁷⁹ $(\text{NaYF}_4:\text{Yb}^{3+}/\text{Tm}^{3+})/\text{NaYbF}_4/\text{NaYF}_4$,⁷⁸ and $\text{NaGdF}_4:\text{Nd}^{3+}/\text{NaYF}_4/\text{NaGdF}_4:\text{Nd}^{3+}, \text{Yb}^{3+}, \text{Er}^{3+}/\text{NaYF}_4$.⁸⁸ It is worth noting that Zhao et al. was the first to show that the core/shell $\text{NaYF}_4:\text{Yb}^{3+}/\text{Er}^{3+}@ \text{NaGdF}_4$ UCNPs can be prepared employing monolayer-by-monolayer deposition,⁶³ opening a new era for nanophotonic control of upconversion in core/shell nanostructure with a sub-nanometer precision.

Although the multi-step approach is able to prepare a core/multishell structure with precision and flexibility, it utilizes prolonged heating, volatile solvent removal, centrifugation and washing for growth of each shell. Hence, the preparation process is time-consuming and laborious, especially when a few shell layers are needed. To overcome this, a protocol of one pot successive layer-by-layer (SLBL) deposition was introduced. It utilizes seed-mediated epitaxial growth, which is flexible to deposit uniform multishells on both hexagonal and cubic phase cores via successive introduction of the shell precursor solutions (Ln-OA and Na-TFA-OA dissolved in high boiling-point OA/ODE mixture) (Figure 7).¹⁵² The shell thickness was shown to be well controlled in the range from 1 monolayer (0.36 nm) to more than 20 monolayers (8 nm) by simply adjusting the amounts of the shell precursors. The stoichiometric doping of lanthanides into the shell as well as into the core domain provides a large degree of freedom for engineering light upconversion in a core/shell

structure. The principle of SLBL protocol has implications for the one pot growth of core/multishell nanostructures through the Ostwald-Ripening strategy, when sacrificial nanoparticles are employed as the shell precursor.

3.3. Mesoporous Silica Coating

Silica coating is a strategy for inorganic surface treatment to make nanoparticles water-dispersible and biocompatible as well as to introduce new therapeutic functionalities when using mesoporous silica to entrap a therapeutic agent and deliver it to the disease site. Silica is known to be highly stable, biocompatible, and optically transparent. When utilized as a coating material, surface silanization can flexibly offer abundant functional groups (*e.g.*, -COOH, -NH₂, -SH, *etc.*), allowing for conjugation with biomolecules. Generally, there are two types of conventional chemistry to coat nanoparticles with silica: (i) Stöber method, which applies to the hydrophilic UCNPs using well-established sol-gel chemistry that involves the hydrolysis and condensation of alkoxide-based precursors, such as tetraethyl orthosilicate (TEOS); (ii) Reverse micelle microemulsion, which applies to UCNPs that has hydrophobic capping ligands. This method utilizes chemical reactions in nano-confined hydrophilic cavities generated by a homogeneous mixture of ammonia, cyclohexane, surfactant (*e.g.*, Igepal CO-520), and tetraethyl orthosilicate (TEOS). Since therapeutic upconversion nanoparticles typically exploit mesoporous silica coated core/shell UCNPs structures, we focus here on chemistries to prepare them. Readers interested in UCNPs with non-mesoporous silica coating are recommended to refer to recent reviews on this topic.^{2,17,147}

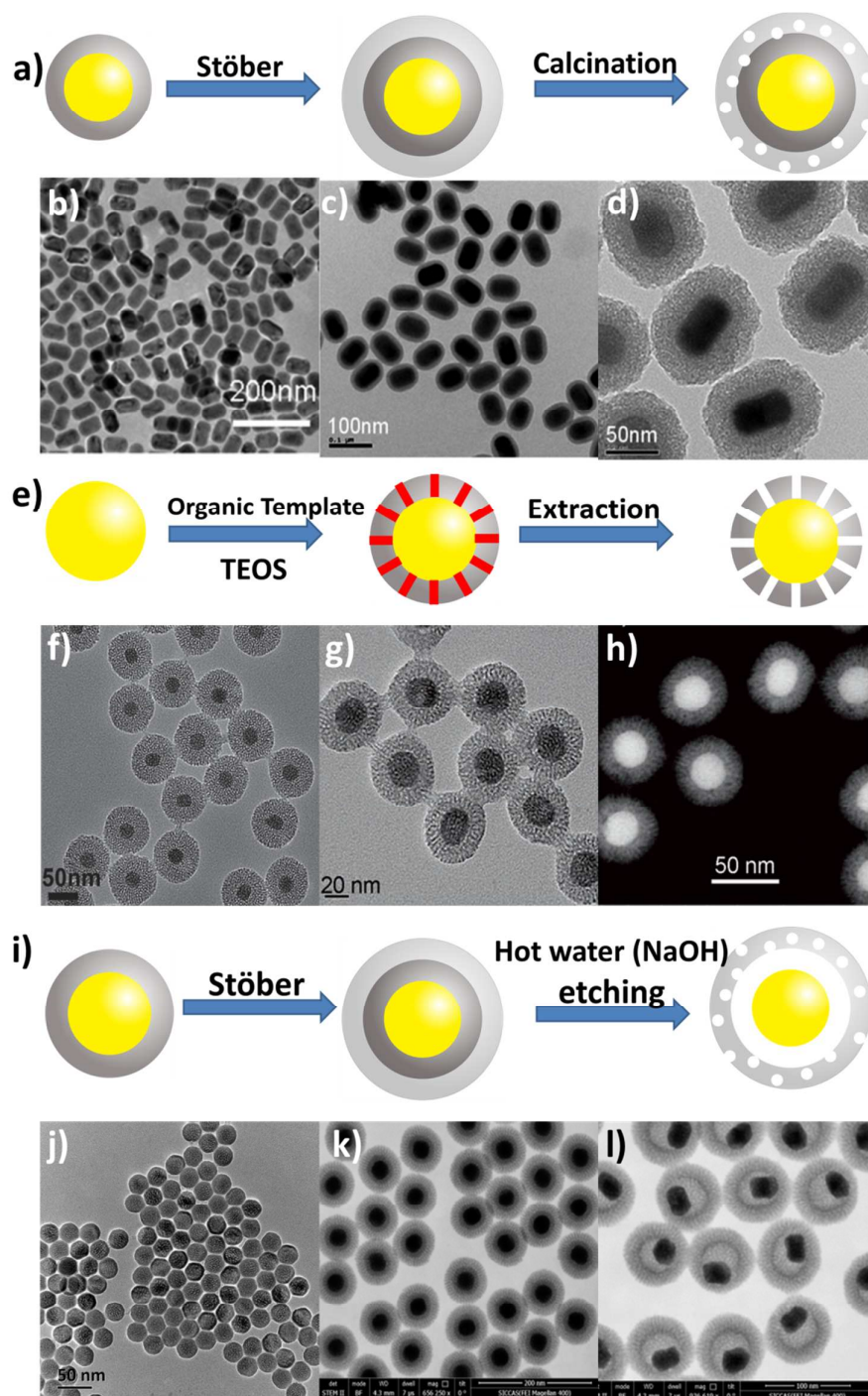


Figure 8. Coating of UCNPs with a mesoporous silica shell. (a) Schematic of the calcination method; (b-d) Corresponding TEM images of $\text{NaYF}_4:\text{Yb}^{3+}/\text{Er}^{3+}$, $\text{NaYF}_4:\text{Yb}^{3+}/\text{Er}^{3+}@$ silica, and mesoporous-silica-coated $\text{NaYF}_4:\text{Yb}^{3+}/\text{Er}^{3+}@$ silica nanoparticles obtained using the calcination method. (e) Schematic of the template method; (f) TEM image of

β -NaYF₄:Yb³⁺/Er³⁺@ β -NaGdF₄:Yb³⁺/Er³⁺@mSiO₂ nanocomposites, prepared using CTAB as a template, (g, h) TEM and dark-field STEM image of NaYF₄:Tm³⁺/Yb³⁺@NaYF₄@mSiO₂ prepared using CTAC as a template. (i) Schematic of the etching method; (j) TEM image of NaYF₄:Yb/Tm@NaYF₄, (k) HAADF STEM image of NaYF₄:Yb/Tm@NaYF₄@dSiO₂@mSiO₂, (l) HAADF STEM image of NaYF₄:Yb/Tm@NaYF₄@hmSiO₂ (d SiO₂, dense layer silica; mSiO₂ mesoporous layer silica, hmSiO₂ obtained by etching the dense silica layer in hot water). Reproduced with permission from refs. 153, 158 and 162. Copyright 2009 and 2013, John Wiley and Sons. Copyright 2014, American Chemical Society.

A mesoporous silica shell on UCNPs can be obtained by three methods, as illustrated in Figure 9. (i) The calcination method (Figure 8 a), which typically takes three steps. The first step is to produce an amorphous silica shell on top of UCNPs, which is then coated with an organically modified silica shell using the Stöber method, where a combination of tetraethylorthosilicate and octadecyltrimethoxysilane with an appropriate ratio is used as silica precursor. Finally, calcination at high temperature (~ 500 °C) yields a mesoporous silica on top of UCNPs@amorphous silica core/shell nanostructure. Zhang *et al.* have utilized this method to prepare the core/shell NaYF₄:Yb³⁺/Er³⁺@SiO₂@mSiO₂ nanoparticles to incorporate a photosensitizer or a genetic material into the mesoporous silica for upconversion photodynamic therapy (UC PDT) or controlled drug release in order to explore activation by deep penetrating NIR light excitation (Figures 8 b-d).^{26, 27, 153} (ii) The organic template method (Figure 8 e), which utilize a surfactant, [for example, cetyl trimethylammonium bromide (CTAB) or hexadecyl trimethyl ammonium chloride (CTAC)] as a template. In this method, the first step is to produce a hydrophilic complex of CTAB or CTAC with UCNPs, which is then processed with Stöber method to create a template-patterned silica shell.

Subsequent extraction of the CTAB or CTAC using ion exchange (*e.g.*, with sodium chloride) yields a patterned mesoporous silica shell. Cichos and Karbowski developed a general and versatile procedure based on CTAB to produce a controlled thin mesoporous silica layer on the top of lanthanide-doped NaGdF₄ nanoparticles and PbS quantum dots.¹⁵⁴ Shi *et al.* utilized a CTAC template to prepare NaYF₄:Yb³⁺/Tm³⁺@mSiO₂ core/shell UCNPs for light-regulated drug release by making use of the NIR-to-UV mediated trans–cis photoisomerization of azo molecules grafted in the mesopore network of a mesoporous silica layer.¹⁵⁵ Lin *et al.* have utilized CTAB as a template to fabricate a set of multifunctional mesoporous core/shell structured nanocomposites such as Fe₃O₄@SiO₂@mSiO₂@NaYF₄:Yb³⁺/Er³⁺,¹⁵⁶ Gd₂O₃:Er³⁺@SiO₂@mSiO₂,¹⁵⁷ β-NaYF₄:Yb³⁺/Er³⁺@β-NaGdF₄:Yb³⁺/Er³⁺@mSiO₂ nanocomposites (Figures 8 f-h)¹⁵⁸ and NaYF₄:Yb³⁺/Er³⁺@SiO₂@mSiO₂,¹⁵⁹ to be used as efficient nanoagents for drug delivery and optical imaging. A critical review by Lin and co-workers on this topic has appeared recently.¹³⁸ (iii) Etching method (Figure 8 i). This method usually involves the growth of two dense silica shells, and the second shell growth usually employed a water-phase Stöber method. Subsequently, a surface-protected hot water etching process (using PVP as a surface protector) at ~ 95 °C can etch away the first silica shell and produce mesoporous pores in the second silica shell, yielding a “yolk” nanostructure with a mesoporous silica shell. Shi *et al.* have utilized this method to produce a yolk nanostructure of NaYF₄:Yb³⁺/Er³⁺@NaGdF₄@mSiO₂ to be used for synergetic chemo-/radiotherapy as well as to deliver magnetic/luminescent dual-modal imaging modality.¹⁶⁰ The same nanostructure has also been utilized for real-time *in vivo* quantitative monitoring of drug release determined by the varied signal intensities of both MRI and UCPL.¹⁶¹ The same group prepared NaYF₄:Yb/Tm@NaYF₄@hmSiO₂ using similar approach for selective hypoxia imaging *in vivo* upon NIR excitation (Figures 8 j-l).¹⁶²

3.4. Coupling of UCNPs with Plasmonics using Core/Shell architecture

Coupling of plasmonic properties with UCNPs can be of great importance for obtaining plasmonically enhanced UCPL (see section 2.6). On the other hand, even if plasmonic effect on UCPL is not revealed, the core/shell architected hybride of upconversion and plasmonic nanosystems might be of significance for number of applications exploiting both plasmonic and UCPL features (e.g., optical and photoacoustic imaging, imaging guided photothermal therapy, etc.). Two variants for the fabrication of the plasmonic core/shell structures (Figure 9) are described below.

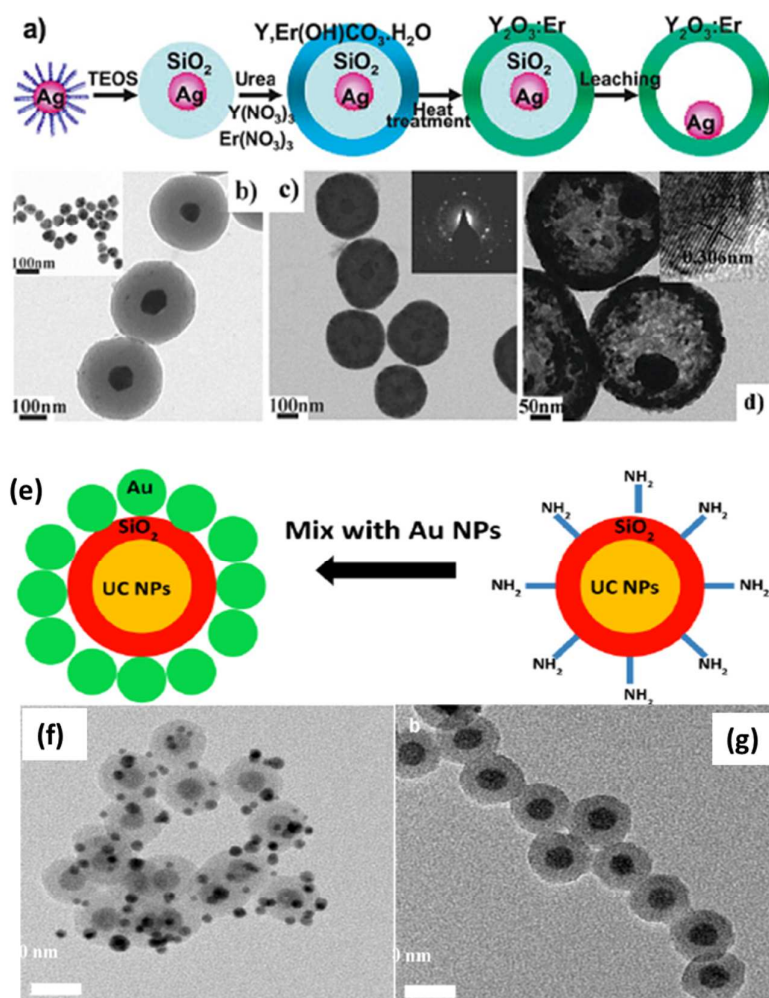


Figure 9. (a) Schematic illustration for preparing core/shell/shell structures of

metallic@silica@UCNPs, along with (b-d) TEM images of the nanostructures obtained in each step. (e) Schematic illustration for synthesizing UCNPs@silica@metallic core/shell/shell structure, along with (f) and (g) TEM images of the corresponding samples. Reproduced with permissions from refs. 113 and 121. Copyright 2010 American Chemical Society and 2013 Ivy Spring International Publisher.

(i) Metallic@Silica@UCNPs Nanostructure. Figure 9 (a) illustrates a typical procedure for creating metallic@silica@UCNPs core/shell/shell nanostructure, where a plasmonic metallic core of silver (Ag) nanospheres are utilized as an example.¹¹³ The first step is to coat silica onto metallic nanoparticles by using either the Stöber method or the reverse micelle microemulsion method (Figure 9 b). By controlling the coating process, the resulting metallic@SiO₂ (e.g., Ag@SiO₂) can have a uniform diameter and contain one metallic nanoparticle positioned at the centre. The thickness of the silica can also be precisely controlled via adjusting the amount of the utilized TEOS as well as by varying other parameters. In the second step, the metallic@SiO₂ can then be coated with a layer of Y:Ln(OH)CO₃·H₂O through a homogeneous precipitation method from yttrium nitrate, lanthanide nitrate, and urea (e.g., at 90 °C for 2 h) (Figure 9 c). Finally, heat treatment at high temperature (e.g., 700 °C for 3 h) can convert the Y:Ln(OH)CO₃·H₂O layer into a crystallized lanthanide-doped Y₂O₃ upconverting layer (Figure 9 d). The thickness of this layer is determined by the thickness of the layer of Y:Ln(OH)CO₃·H₂O. This procedure was employed by Zhang *et al.* to prepare Ag@SiO₂@Y₂O₃:Er³⁺ nanoparticles.¹¹³ An optimized LSPR UC enhancement of ~40 times was reported, along with the use of this nanoplatfrom for bioimaging. Ge *et al.* reported on LSPR enhanced UCPL in Au@SiO₂@Y₂O₃:Yb³⁺/Er³⁺ nanoparticles which are prepared utilizing the chemistry described here.³⁵ An optimization of the silica spacer's thickness resulted in a maximum

~10 fold enhancement of the green UC emission of Er^{3+} ions, when excited at ~980 nm. It is to be noted that the chemistry described in this section can be extended to prepare other multifunctional core/shell nanoparticle platforms, e.g., core/shell/shell $\text{Fe}_3\text{O}_4@\text{SiO}_2@\text{NaYF}_4:\text{Yb}^{3+}/\text{Er}^{3+}$ that integrate the magnetic properties and the UCPL properties for targeted chemotherapy.¹⁶³ For this, the metallic nanoparticles are replaced by Fe_3O_4 , and the $\text{Fe}_3\text{O}_4@\text{SiO}_2@\text{Y}_2\text{O}_3:\text{Yb}^{3+}/\text{Er}^{3+}$ is further subject to ion-exchange in the presence of HF and NaF solution to form the $\text{Fe}_3\text{O}_4@\text{SiO}_2@\text{NaYF}_4:\text{Yb}^{3+}/\text{Er}^{3+}$ multifunctional nanopatform.

(ii) UCNPs@Silica@Metallic Nanostructure. The chemistry or the procedure to prepare UCNPs@silica@metallic nanoparticles is illustrated in Figure 9 (e).^{120, 121} The first step involves coating silica onto UCNPs by using either the Stöber method or the reverse micelle microemulsion method (Figure 9 g). An amino-functionalized silica can be produced by refluxing the $\text{NaGdF}_4:\text{Yb}^{3+}/\text{Er}^{3+}@\text{silica}$ nanoparticles dispersed in ethanol with the addition of a hint amount of 3-aminopropyltriethoxysilane (APTES) at an elevated temperature for a reasonable time range (e.g., at 80 °C for 1 hour). As the amino group has a strong affinity to the metallic element, the amino-functionalized silica can directly hold the synthesized metallic nanoparticles with a loosely coordinated ligand (e.g., poly-vinylpyrrolidone) (Figure 9f).¹²¹ We have prepared $\text{NaGdF}_4:\text{Yb}^{3+}/\text{Er}^{3+}@\text{silica}@\text{Au}$ nanostructures using this nanochemistry for biomodal optical imaging as well as for studies of LSPR interaction with UCPL.¹²¹ Li *et al.* reported on $\text{NaYF}_4:\text{Yb}^{3+}/\text{Er}^{3+}@\text{silica}@\text{Au}$ satellites for tunable green-to-red upconversion emissions using the absorption capability of gold.¹²⁰ This chemistry has also been utilized to prepare PEGylated $\text{NaY}/\text{GdF}_4:\text{Yb}^{3+}, \text{Er}^{3+}, \text{Tm}^{3+} @\text{SiO}_2-\text{Au}@\text{PEG5000}$ nanoparticles with an uniform size of less than 50 nm for CT, MR, as well as for upconversion luminescence bioimaging.¹⁶⁴ It is important to note

that when replacing the silica shell with ligands containing functional groups, the chemistry as well as the procedure outlined can be utilized to grow UCNPs/ligands/metallic nanostructures to deliver a combined and/or synergistic plasmonic and UCPL properties.¹¹⁰

4. Characterizations of Core/Shell Upconversion Nanoparticles

A range of characterization tools can be utilized to indirectly suggest or directly verify the presence of a core/shell structure. These characterization tools encompass X-ray diffraction (XRD), transmission electron microscopy (TEM), X-ray photoelectron spectroscopy (XPS) based on tunable synchrotron radiation, high-angle annular dark-field (HAADF) scanning transmission electron microscopy (STEM), electron energy loss spectroscopy (EELS), energy-dispersive X-ray spectroscopy (EDX), PL lifetime, PL intensity, etc. Typically, the formation of a core/shell structure can be indicated by presence of five characteristic features (Figure 10): (i) The increase of the average size, due to the introduction of a new layer onto of the core only nanoparticles. The average size values can be directly obtained through averaging the size of nanoparticles in TEM images, or calculated through the XRD pattern via Scherrer's equation. (ii) The variance of UCPL intensity. The formation of an epitaxial core/shell structure can significantly increase UCPL due to suppression of surface-related quenching mechanisms. Non-epitaxial core/shell structure, e.g., UCNPs@silica and UCNPs@metallic, also can affect the UCPL due to the interaction between the core and the non-epitaxial shell. (iii) The variance of UCPL lifetime. An epitaxial core/shell structure generally can result in a prolonged UCPL lifetime as compared to that of the core only nanoparticles. This is due to spatial isolation of the lanthanide ions from the surrounding surface quenchers as well as the passivation of surface defects of the core nanoparticles. (iv) The TEM contrast between the core domain and the shell domain in a single nanoparticle. (v) The variance of element content between

the core domain and the shell domain in a single nanoparticle. The last two features are able to provide direct evidence of the formation of a core/shell structure, which will be discussed in the following two sections.

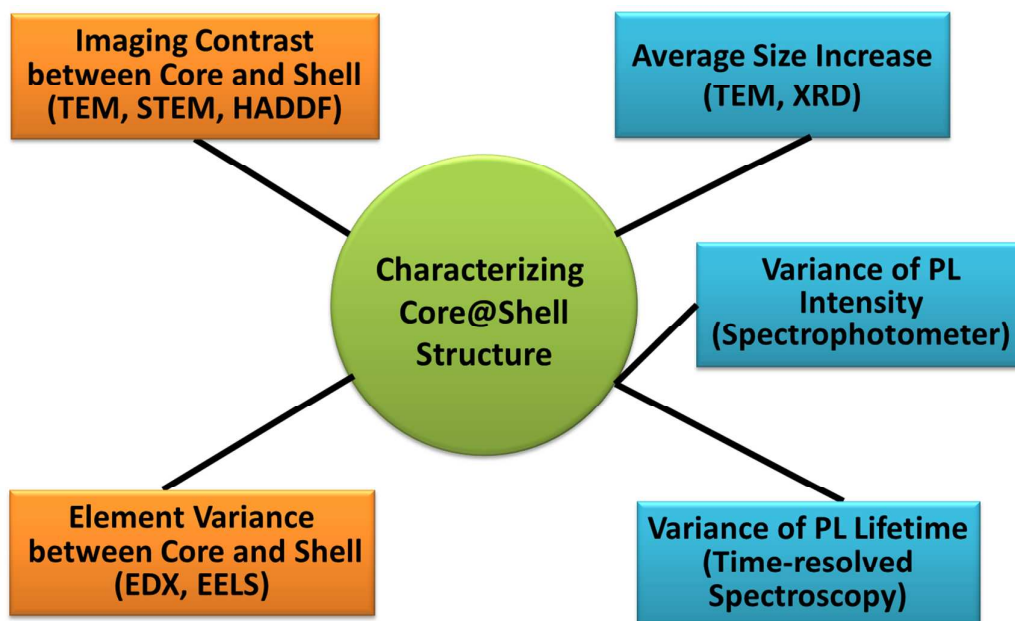


Figure 10. Schematic illustration of five strategies to characterize formation of a core/shell structure. The imaging contrast and the elemental variance provide direct evidence to verify the formation, while the other three strategies yield indirect evidence to suggest the formation.

4.1. Imaging of Core–Shell Structures

The primary limitation for characterization techniques to demonstrate the formation of a core/shell structure is that it may be unable to clearly distinguish the structural and compositional variance between the shell layer and the core. TEM only discerns the core/shell structure when the core and the shell have significant difference in composition and crystallinity (and corresponding difference in electron scattering) to create a good phase contrast between the core and the shell. Usually, non-epitaxial core/shell UCNPs nanostructures can be visualized in such way; for example, the

core/shell structure of the UCNPs@Silica and Ag@Silica@UCNPs can be easily discerned in regular TEM phase contrast imaging.^{113, 121} However, TEM phase contrast imaging does not generally work for epitaxial core/shell UCNPs, since the core and the shell are compositionally similar or identical, and have similar crystallinity.

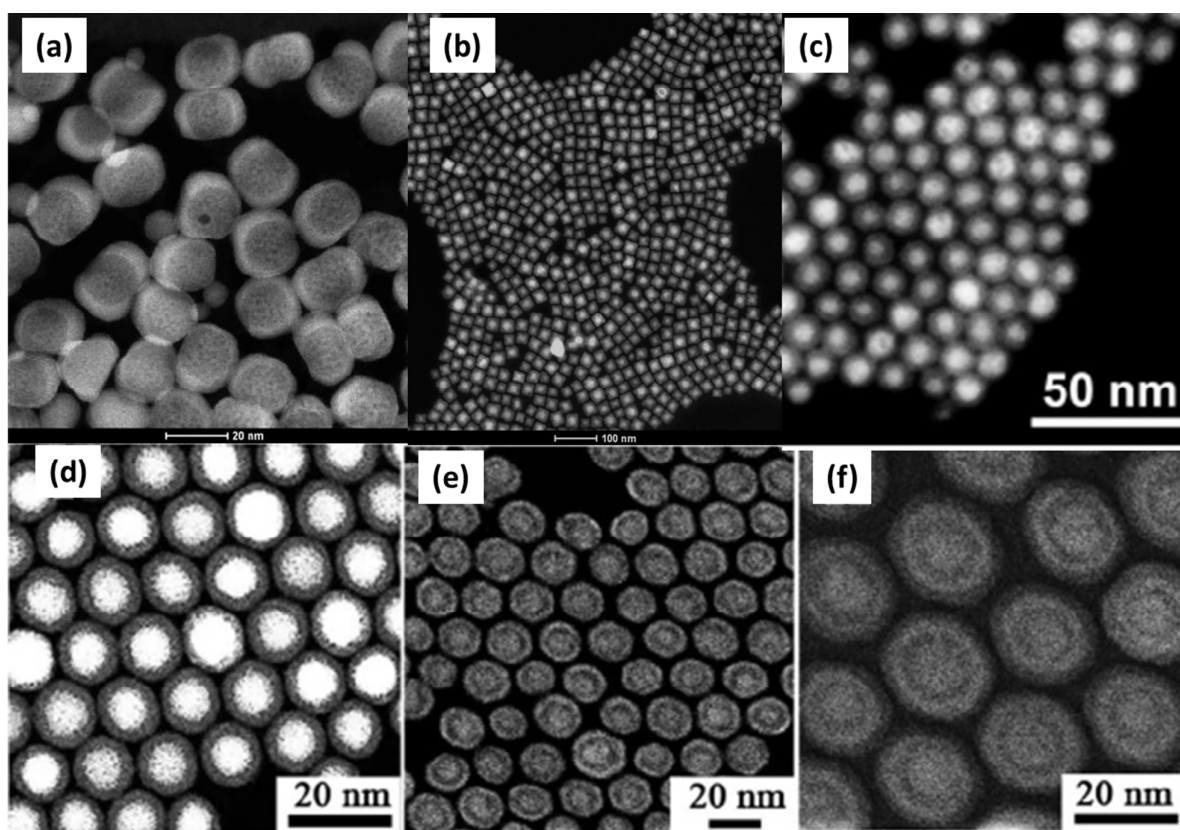


Figure 11. HAADF STEM image of (a) $\text{NaYF}_4@\text{NaGdF}_4$, (b) $(\text{NaYbF}_4:0.5\% \text{Tm}^{3+})@\text{CaF}_2$, (c) $\text{NaYF}_4:\text{Yb}^{3+}/\text{Er}^{3+}@\text{CaF}_2$, (d) $\text{NaGdF}_4:\text{Nd}^{3+}/\text{NaYF}_4$, (e) $\text{NaGdF}_4:\text{Nd}^{3+}/\text{NaYF}_4/\text{NaGdF}_4:\text{Nd}^{3+}, \text{Yb}^{3+}, \text{Er}^{3+}$ and (f) $\text{NaGdF}_4:\text{Nd}^{3+}/\text{NaYF}_4/\text{NaGdF}_4:\text{Nd}^{3+}, \text{Yb}^{3+}, \text{Er}^{3+}/\text{NaYF}_4$ nanoparticles with resolved core/shell structures. Reproduced with permission from refs. 25, 88, and 165. Copyright 2012 American Chemical Society. Copyright 2013 Nature Publishing Group.

Although to date there is a lack of tools to discern the homogenous core/shell epitaxial structure, HAADF can be still utilized to discriminate the heterogeneous epitaxial core/shell structure, as the

contrast of HAADF is approximately proportional to the square of the atomic number of the element contained, producing a *z*-contrast image.²⁵ This technique was also used by Veggel *et al.*, Zhao *et al.*, and Chen *et al.* to demonstrate the formation of NaYF₄@NaGdF₄ (Figure 11 a) or NaGdF₄@NaYF₄ heterogeneous core/shell structure, in which the Y-rich domain appears to be darker than the Gd-rich domain.^{63, 68, 165} We have utilized HAADF to characterize the alpha-NaYbF₄:Tm³⁺@CaF₂ core/shell structure, the image of which shows a clear contrast between the core which appears bright (ytterbium *Z* = 70,) and the shell which appears dark (calcium *Z* = 20) (Figure 11 b).²⁵ Yan *et al.* and Chen *et al.* employed this technique to demonstrate the formation of NaYF₄:Yb³⁺/Er³⁺@CaF₂ (Figure 11 c) and CaF₂:Yb³⁺/Er³⁺@CaF₂ core/shell structure, respectively.^{65, 166} HAADF-STEM images of core/shell and core/multishell NaGdF₄:Nd@NaYF₄, NaGdF₄:Nd@NaYF₄@NaGdF₄:Nd,Yb,Er, (Figure 11 e, f) and NaGdF₄:Nd@NaYF₄@NaGdF₄:Nd,Yb,Er@NaYF₄ (Figure 11 g) nanoparticles were also presented recently by Zhao *et al.*⁸⁸ However, the utilization of this technique requires an adequate difference between atomic number of the elements in core and shell.

4.2. Element Mapping in a Single Nanoparticle

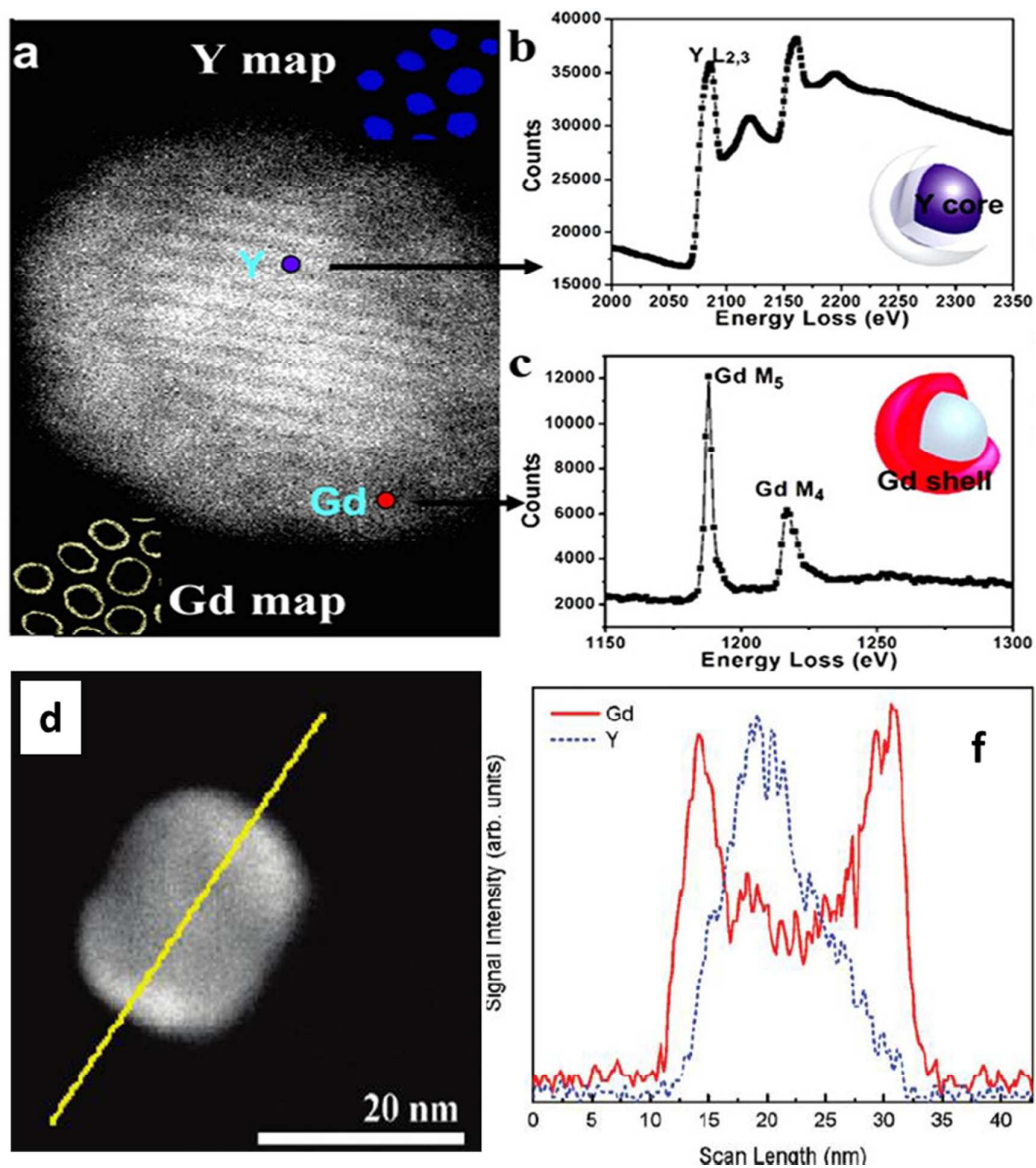


Figure 12. (a) HAADF image of a single NaYF₄:Yb³⁺/Er³⁺@NaGdF₄ nanocrystal. EELS spectra of yttrium L_{2,3} (b) and gadolinium M_{4,5} (c) edges taken from the probe location on the inferred NaYF₄:Yb³⁺/Er³⁺ core and NaGdF₄ shell. (d) TEM image of one single NaYF₄@NaGdF₄ nanoparticle, as well as (e) the corresponding results of an EDS line scan. Reproduced with permission from refs. 63 and 165. Copyright 2012 American Chemical Society.

The element difference between the core and the shell provides another way to discern the heterogeneous core/shell structure. Veggel *et al.* first reported direct evidence for such core/shell

structure ($\text{NaYF}_4@/\text{NaGdF}_4$ UCNPs) formation using XPS produced by tunable synchrotron radiation.⁶⁷ The intensity ratio of the Y^{3+} 3d peak to the Gd^{3+} 4d peak increases with an elevation of the kinetic energy of the synchrotron radiation, indicating that the Gd^{3+} from the shell screens the Y^{3+} intensity from the core, and thus providing direct evidence for a core/shell structure. While this characterization technique does deliver a confirmation of a core/shell structure, it is an ensemble measurement and does not provide elemental details about a single core/shell UCNP. With respect to this, the line scan of EDX and EELS can provide the precise element distribution of single core/shell nanostructures.¹⁶⁵ The characterization capabilities of EDX are due to that each element has a unique atomic structure, yielding a unique, well energy separated, set of peaks in its X-ray spectrum, as in the case of $\text{NaYF}_4/\text{NaGdF}_4$ core/shell structure (Figures 12 d and f).¹⁶⁵ In our previous work, EDX line scan conducted with STEM imaging on a $\text{NaYbF}_4/\text{CaF}_2$ nanoparticle showed a higher Ca concentration in the peripheral region and a higher Yb concentration in the central region of the crystal, verifying the designed heterogenous core/shell structure.²⁵ In EELS, a material is exposed to a beam of electrons with a known, narrow range of kinetic energies. Some of the electrons will undergo inelastic scattering, which means that they lose energy and have their paths slightly and randomly deflected. The amount of energy loss can be measured using an electron spectrometer and interpreted, in terms of what caused the energy loss. Zhao *et al.* demonstrated the use of cryo-TEM operating at 96 K to minimize the electron beam damage and provided evidence of a core/shell structure (Figures 12 a-c). A linear correlation between the NaGdF_4 shell thickness and the optical properties of monodisperse hexagonal $\text{NaYF}_4:\text{Yb}^{3+}/\text{Er}^{3+}@/\text{NaGdF}_4$ core/shell nanoparticles was demonstrated, revealing the importance of the shell thickness.⁶³

5. Applications of Core/Shell UCNPs

5.1 Biomedical Applications

5.1.1 Deep 3D Bioimaging

Optical imaging is one of the most important techniques used in biomedical imaging as it is capable of providing cellular or molecular level information with almost single molecule sensitivity.^{167, 168} Owing to their unique and versatile spectral properties and exceptional stability, UCNPs are found to be excellent optical probes for photoluminescence bioimaging, as they are devoid of many drawbacks attributed to other photoluminescent probes, namely broad emission and susceptibility to bleaching for organic luminophores, blinking and toxicity for semiconductor QDs, etc.² The UCNPs, possessing spectrally narrow and tunable emission bands excitable by a single wavelength in NIR, can be readily employed as probes for multiplexed bioimaging.¹⁶⁹ Numerous studies reported the use of UCNPs as targeted probes for cellular imaging *in vitro*,^{169, 170} but full advantages of UCPL imaging with UCNPs are revealed in the *in vivo* imaging, since anti-Stokes character of the emission excludes manifestation of the auto-fluorescence from the biological tissues, resulting in a decrease in the imaging background. In addition, the imaging background produced by the scattering of excitation light can be reduced by using short-pass filters with the imaging camera, since the emitted light is considerably shifted in wavelengths relatively to excitation. Another benefit of UCPL imaging with UCNPs is that the excitation of the upconversion emission lies in the NIR spectral range, more importantly in the “optical transparency window” for the biological tissues (~700-1000 nm). NIR light of this spectral range attenuates less and penetrates deeper in the tissue as a result of both lower absorption of the tissue constitutions and reduced scattering for NIR light.^{171, 172} In a marked contrast to the multiphoton imaging employing NIR excitation from expensive ultrashort-pulsed lasers, a low-cost cw laser diode can be utilized as the NIR excitation source for UCPL

imaging, with an excitation density of $\sim 10^{-1} \text{ W/cm}^2$.^{2, 12, 173} We have pioneered a UCPL bioimaging approach in which both excitation (980 nm) and emission (800 nm) wavelengths are in the optical transmission window, utilizing the NIR-to-NIR upconversion in $\text{Tm}^{3+}/\text{Yb}^{3+}$ -codoped NaYF_4 UCNPs.²⁴ In this work, a NIR-to-NIR UCPL imaging of a Balb-c mouse intravenously injected with UCNPs was reported, with the signal to background ratio (SBR) evaluated to be on the order of ~ 10 . It is important to emphasize that as the UC QY is strongly dependent on the excitation power density, UCNPs with a high UC quantum yield at low power excitation density is of critical importance for deep tissue imaging. This is because, according to the *American National Standard Z136.1-2007* (American National Standard for Safe Use of Lasers), the employed excitation power density for a $\sim 980 \text{ nm}$ cw laser has to be lower than the safety threshold of 0.73 W/cm^2 when applied to human skin. Moreover, the strong scattering properties of a tissue will produce a significantly lower excitation density (than the excitation density at the tissue surface) at the location of UCNPs inside the tissue. As illustrated in section 2.1, the core/shell design is an important strategy to reach a high UC QY.

Introduction of the core-shell architected UCNPs with boosted UC QY allows us to further improve sensitivity of NIR-to-NIR UCPL in vivo imaging. The $\alpha\text{-}(\text{NaYbF}_4:0.5\% \text{ Tm}^{3+})@\text{CaF}_2$ core/shell UCNPs manifest a UC QY as high as 0.6% under an excitation of 0.3 W/cm^2 .²⁵ As a result, high contrast optical imaging (the SBR is ~ 310) of live animals (mice) was achieved. We have also demonstrated that NIR-to-NIR UCPL imaging is possible through a $\sim 3.2 \text{ cm}$ thick animal tissue (pork), which constitutes a leap forward for 3D optical imaging of deeper tissues using UCNPs.²⁵ It is worth noting that the NIR UC QY of hexagonal $\text{NaLuF}_4:\text{Gd}^{3+}/\text{Yb}^{3+}/\text{Tm}^{3+}$, reported by Li *et al.*, reaches about 0.47% under excitation density of 17.5 W/cm^2 at 980 nm, thus enabling an optical imaging depth of about 2 cm.¹⁷⁴ An epitaxial growth of a shell layer onto this type of UCNPs and

characterization of the UC QY under excitation power density below 0.7 W/cm^2 convenient for imaging would be appealing, possibly leading to even further improved imaging depth and SBR. We note that the total UC QY, covering the UV, visible, and NIR PL spectral range, of $(\text{LiLuF}_4:\text{Yb}^{3+}/\text{Tm}^{3+})@\text{LiLuF}_4$ core/shell UCNPs is reported to be 7.6% at a high excitation power density of 127 W/cm^2 .⁶¹ This suggests the possibility of achieving a high UC QY for the NIR UCPL of $(\text{LiLuF}_4:\text{Yb}^{3+}/\text{Tm}^{3+})@\text{LiLuF}_4$ core/shell UCNPs. It becomes very attractive to characterize their NIR UC QY at the excitation power density suitable for *in vivo* imaging, and apply these UCNPs for optical bioimaging. Andersson-Engels *et al.* recently showed that deep tissue optical imaging of core/shell $(\text{NaYF}_4:\text{Yb}^{3+}/\text{Tm}^{3+})@\text{NaYF}_4$ upconverting nanoparticles can be enabled by exploiting higher intrinsic QY through the use of millisecond single pulse excitation with high peak power.¹⁷⁵ This provides new possibilities for better deep tissue optical imaging (and also optical tomography) using reported core/shell UCNPs and a pulsed laser with optimized parameters.

Another promising direction for UCPL bioimaging is to utilize excitation other than $\sim 980 \text{ nm}$, since water absorbance at this wavelength can cause significant heating of a biological tissue under irradiation. S. He with co-authors explored the heating effect under 980 nm irradiation and proposed the use of the 915 nm laser, which produces less heating, to excite cubic $\text{NaYbF}_4:\text{Yb}^{3+}/\text{Tm}^{3+}$ UCNPs in the UCPL biomaging *in vitro* and *in vivo*.¹⁷⁶ It should be however noted that that UCPL in this case still originates from the absorption of Yb^{3+} ions, which has maximum at $\sim 980 \text{ nm}$ and is much weaker at 915 nm . Since UCPL is proportional to the absorption of the exciting light by UCNPs, an efficient UCPL imaging with excitation at $\sim 980 \text{ nm}$ could be achieved at a lower excitation power than for 915 nm excitation, without producing significant heating. A comparison of UCPL imaging at $\sim 980 \text{ nm}$ and 915 nm (or another wavelength from the spectral range of Yb^{3+} absorption), along

with evaluation of the thermal effect produced by both wavelengths, is needed to conclude how beneficial it would be to excite at 915 nm for the UCPL imaging employing UCNP containing Yb^{3+} ions.

The heating effect caused by long time irradiation at 980 nm can be also significantly reduced when using other NIR excitation wavelengths, introduced through doping of other NIR absorbing lanthanide ions. In particular, to tune the NIR absorption of the nanoparticles, incorporation of Nd^{3+} ions can be proposed.⁸⁴⁻⁸⁶ Very recently, Zhong *et al.* reported the $\text{NaYF}_4:\text{Yb}^{3+}$ 20%, Er^{3+} 2% @ $\text{NaYF}_4:\text{Yb}^{3+}$ 10% @ $\text{NaNdF}_4:\text{Yb}^{3+}$ 10% core/shell/shell UCNP (ErCSS), which are excitable at 800 nm owing to incorporation of Nd^{3+} ions into the outer shell.⁸⁹ The absolute quantum yield for the UCPL peaked at ~540 nm is 0.11% under excitation at 800 nm with power density of 20 W/cm^2 . Figure 13 (a) illustrates contributions of the Nd^{3+} and Yb^{3+} ions into absorption of ErCSS. As a result of the difference in extinction, UCPL under 800 nm excitation were found to be ~8 times brighter than under 980 nm excitation (Figure 13 b). It should be noted that the intensity of UCPL from ErCSS excited at 980 nm was similar to that from the conventional $\text{NaYF}_4:\text{Yb}^{3+}$ 20%, Er^{3+} 2% @ NaYF_4 core/shell UCNP of similar size (Figure 13 b). The possibility of *in vivo* UCPL imaging with ErCSS and ErCS was evaluated and compared. After penetrating of the exciting light through ca. 1 cm of lean pork, a much higher SBR image was acquired from 800 nm-excited UCNP than from the control sample with 980 nm excitation (Figure 13 c). Due to the difference in water absorption at 800 and 980 nm, after penetrating through 5 cm of water, the UCPL of the Nd^{3+} -sensitized UCNP was about 125 times stronger than that of the conventional Yb^{3+} -sensitized UCNP.⁸⁹ The lower water absorption of 800 nm laser source not only results in a deeper penetration depth, but can also help to minimize tissue overheating. As shown in Figure 13 d, a much higher temperature

distribution can be observed for the 980 nm irradiated area, compared with the 800 nm irradiated one. While the temperature of 800 nm laser heated water was raised from initially 24 °C to 25.7 °C, water under 980 nm irradiation was heated to a temperature as high as 45.9 °C (same excitation power density and exposure time were used in both cases).

Although UCNPs with Nd³⁺ sensitized UCPL do show a promising potential for deep tissue imaging, it should be however noted that, since the green UC emission of Er³⁺ at ~540 nm is outside the optical transparency window and can be strongly attenuated by biological tissues, further studies are necessary to provide evidence for superior advantage of these UCNPs for deep tissue imaging, when compared with the use of well-established NIR-to-NIR Yb³⁺/Tm³⁺-doped core/shell UCNPs.²⁵

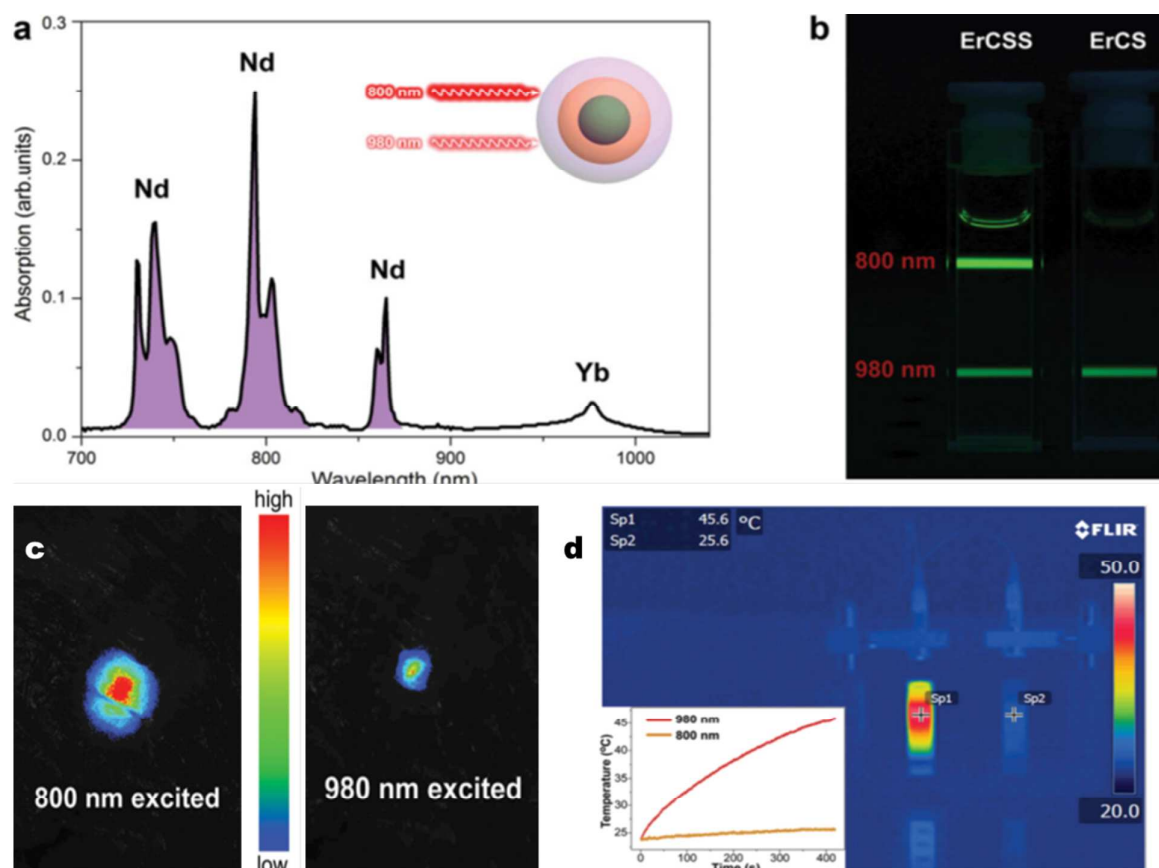


Figure 13. Comparison of UCPL under excitation at 800 nm and 980 nm for Nd³⁺-doped core/shell/shell UCNPs (ErCSS) and conventional Yb³⁺-sensitized core-shell UCNPs (ErCS). a)

Absorption spectra of ErCSS (20 mg mL⁻¹ in hexane). b) UCPL photographs of ErCSS and ErCS excited at 800 (top) and 980 nm (bottom) with 0.5 W cm⁻² diode lasers. c) UCPL from Nd³⁺-sensitized nanoparticles excited at 800 nm (left) and from Yb³⁺-sensitized nanoparticles excited at 980 nm (right). Excitation with power density of 400 mW cm⁻² was used. d) Temperature-distribution image recorded after 7 min irradiation (Sp1: 980 nm; Sp2: 800 nm; 20 W/cm²). Inset: Temperature increase with time under 800 and 980 nm. Reproduced with permission from ref. 89. Copyright 2014 John Wiley and Sons.

5.1.2. Multimodal Bioimaging

While UCPL is the key feature of UCNPs and provides a basis for their application in bioimaging, they can also open the door for other possibilities in biomedical field. There is a growing interest in the development of nanoparticle probes that can function as multiple contrast agents for simultaneous use in different medicinal imaging modalities providing complementary diagnostic information (e.g., optical, MRI, PET, SPECT, CT). Correlation between these imaging techniques using a single multimodal nanoprobe will accelerate the diagnostic process, while reducing the stress on the patient related to multiple steps necessary for complete diagnostic using the current imaging technology.¹²³ As discussed in section 2.7.1, with use of a hierarchical core-shell approach, a range of imaging modalities can be incorporated into UCNPs, thus supporting their use as multimodal nanoprobes. For example, epitaxial core/shell UCNPs of NaYF₄:Yb³⁺/Er³⁺@NaGdF₄,¹⁷⁷ NaYF₄:Yb³⁺/Tm³⁺@NaGdF₄,¹²⁷ and NaYbF₄:Tm³⁺@NaGdF₄,⁶⁰ as well as non-epitaxial epitaxial core/shell UCNPs of NaYF₄:Tm³⁺/Yb³⁺/Gd³⁺@mSiO₂,¹⁷⁸ and NaYF₄:Ln³⁺@Si-DTTA-Gd³⁺,¹⁷⁹ have been reported to exhibit both T1 MR relaxivity (provided by Gd³⁺ ions) and UCPL. Bioconjugation of the Angiopep-2 peptide, using EDC chemistry, on the surface of PEGylated

(NaYF₄:Tm³⁺/Yb³⁺/Gd³⁺)@NaGdF₄ core/shell nanoparticles enables them to cross the BBB barrier to biotarget glioblastoma, and then functions as a simultaneous MRI/NIR-to-NIR UCPL bimodal imaging agent, which showed a much enhanced imaging performance in comparison with the clinically used single MRI contrast (Gd-DTPA) and fluorescent dye (5-ALA).¹⁸⁰ Moreover, Liu *et al.* developed multifunctional nanoparticles, NaYF₄:Yb³⁺/Er³⁺@Fe₃O₄@Au, which incorporated optical and T2 magnetic properties useful for dual-modal imaging, while utilizing the gold shell for photothermal therapy.³⁷ Li *et al.* reported seed-mediated synthesis of NaYF₄:Yb³⁺/Tm³⁺@Fe_xO_y and Fe₃O₄@NaLuF₄:Yb³⁺/Er³⁺/Tm³⁺ core/shell nanostructure as imaging agents for T2 MRI and UCPL bimodal imaging.^{132, 181} Use of the same Fe₃O₄ core but a different (β-NaGdF₄: Yb³⁺, Tm³⁺) shell and a polyelectrolyte coating allowed Anker with co-authors to obtain UCNPs which are stabilized against aggregation through PEGylation and capable to serve as bimodal (UCPL/MRI) imaging probes, providing both T1 and T2 MRI contrast due to availability of both a ferromagnetic core and a paramagnetic shell.¹⁸²

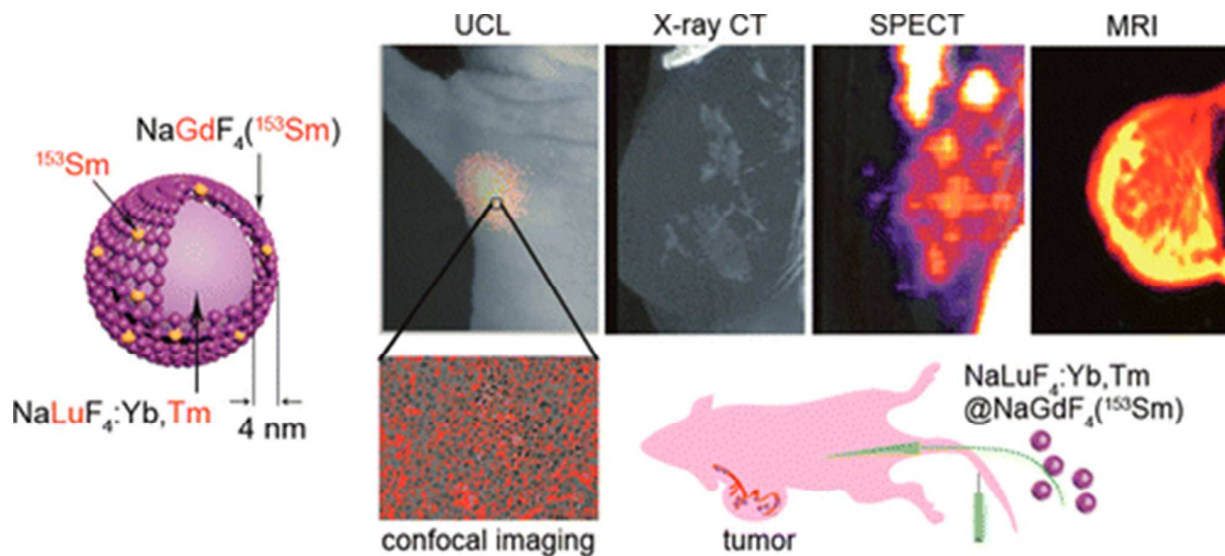


Figure 14. Schematic illustration of NaLuF₄:Yb³⁺/Tm³⁺@NaGdF₄(¹⁵³Sm) core/shell UCNPs for SPECT/CT/MR/UCPL four-modal bioimaging. In this design, the Yb³⁺/Tm³⁺ ion pair provides the

UCPL optical property; the Gd^{3+} ions in the epitaxial shell provides the ability for T1 MR imaging; the Lu^{3+} ions in the core host lattice leads to strong absorption of X-ray to enable for CT imaging, and the ^{153}Sm in the shell (half-life, 46.3 hours) is a radioisotope which produces gamma rays for SPECT imaging. Reproduced with permission from ref. 186. Copyright 2013 American Chemical Society.

In addition to MRI and UCPL biomodal imaging, trimodal CT/MRI/UCPL imaging as well as four modal SPECT/CT/MR/UCPL imaging have also been recently reported, exploiting the capability of a core/shell structure to incorporate multiple modalities. For example, core/shell nanostructures of $\text{Fe}_3\text{O}_4@\text{NaLuF}_4:\text{Yb}^{3+}/\text{Er}^{3+}/\text{Tm}^{3+}$ and $\text{NaLuF}_4:\text{Yb}^{3+}/\text{Tm}^{3+}@\text{SiO}_2\text{-GdDTPA}$ have been reported as imaging probes for tri-modality CT/MRI/UCPL imaging.^{132, 183} TaO_x -decorated $\text{NaYF}_4:\text{Yb}^{3+}/\text{Er}^{3+}/\text{Tm}^{3+}@\text{NaGdF}_4$ core/shell UCNPs were reported by Shi *et al.* for *in vivo* CT/MR/UCPL trimodal imaging.¹⁸⁴ Same type of the trimodal imaging was realized through the design and synthesis of the multi-shell structured $\text{NaYF}_4:\text{Yb}/\text{Tm}@\text{NaLuF}_4@\text{NaYF}_4@\text{NaGdF}_4$ nanoparticles.¹⁸⁵ While Gd^{3+} ions in the outermost shell provide T1-weighted MRI, the thick NaLuF_4 shell epitaxially grown on the core not only constitutes a CT functional layer, but also offers an optically inert layer for remarkable enhancement of the UCPL. More importantly, the $\text{NaLuF}_4:\text{Yb}^{3+}/\text{Tm}^{3+}@\text{NaGdF}_4$ (^{153}Sm) core/shell UCNPs have been reported for use in SPECT/CT/MR/UCPL four-modal bioimaging, providing an excellent paradigm for multimodal imaging using a core/shell architecture (Figure 14).¹⁸⁶ Furthermore, in this work, *in vivo* tumor angiogenesis analysis was performed by combining CT and SPECT imaging with confocal UCL imaging, showing the potential of using multimodal imaging for early detection of disease onset and real-time monitoring of a therapeutic approach.

In all aforementioned multimodal design, the provision of imaging modalities is as follows: (i) The Gd^{3+} , Fe_3O_4 , and TaO_x are utilized to empower the MRI imaging. The Gd^{3+} ions at the shell surface are preferred, which can interact more efficiently with proton. (ii) High Z elements, *e.g.*, Lu^{3+} or Yb^{3+} , are used to produce strong attenuation of X-rays to realize CT imaging. (iii) The $\text{Yb}^{3+}/\text{Er}^{3+}$ (Tm^{3+}) lanthanide ion pairs are doped, preferably in the core, to implement UCPL imaging. Positioning these dopants in the core also exploits the use of shell protection to suppress surface-related quenching mechanism and produce efficient UCPL. (iv) The radionuclide (or radioisotope) of ^{153}Sm and the ^{18}F are utilized to entail for SPECT imaging and PET imaging, respectively. These radioisotopes are often introduced into the shell layer at a later stage during the sample preparation, to avoid adverse interaction with synthetic chemicals. In all, the strategy to construct multimodal imaging nanoprobe using the core/shell structure is to appropriately position each type of imaging contrast element without producing interference between different types.

Novel biomaging techniques are being developed these days which can be combined with the conventional medical imaging modalities using core-shell structured UCNPs as a platform. For example, Niu *et al* recently presented a combination of the UCPL and surface enhanced Raman scattering imaging (SERS) using core-multishell architecture.¹⁸⁷ The silica coated UCNPs ($\text{NaYF}_4:\text{Yb},\text{Er}@\text{SiO}_2$) served as a photoluminescent core. Ag nanoparticles in situ grown on silica layer with different kinds of Raman reporters adsorbed on the surface formed an SERS-functional layer, while last layer of denatured bovin serum albumin (dBSA) was coated on the tag UCPL/SERS tag to improve the colloidal stability and biocompatibility. The combined UCPL/SERS imaging modalities with the synthesized nanoprobe were demonstrated *in vitro* and *in vivo*.¹⁸⁷ In another recent report, the UCPL signal provided by UCNPs in a core-shell nanostructure was shown to be

partly converted to the high photoacoustic (PA) signal which can be utilized in the photoacoustic tomography (PAT).¹⁸⁸ The core UCNP (NaYF₄:Yb³⁺, Er³⁺) were coated with a shell of α -cyclodextrin (α -CD). The UCPL signal for UCNP- α -CD core-shell nanoparticles dispersed in water was found to be noticeably quenched in comparison with that from the core alone UCNP dispersed in cyclohexane. At the same time, the PA signal from the UCNP- α -CD nanoparticles under 980 nm excitation was greatly enhanced, permitted use of these nanoparticles as efficient probes for PAT in vivo. It is suggested that UCPL quenching in UC- α -CD in aqueous solution, resulted from non-radiative relaxation of the excited states, leads to an increase in intrinsic heat generation under 980 nm excitation and subsequent PA signal enhancement.

With their multiple imaging capabilities, UCNP are able to provide a powerful nanocarrier platform for imaging guided drug delivery. Using the hierarchical core-shell approach, the UCNP-based multifunctional nanoparticles can be not only endowed with UCPL, MR and CT imaging abilities, but also loaded with therapeutic agent, serving as nanocarriers for targeted, imaging guided drug delivery.¹⁸⁹⁻¹⁹¹

5.1.3. NIR-Light Controlled Photoactivation and Drug Release

This section focuses on the application of core/shell UCNP as NIR-to-UV photon nanoconverters to initiate a UV-mediated photochemical process in situ. The UV-triggered photochemistry can be potentially applied to control chemical reactivity with a spatial and temporal precision for the widest applications range. However, its practical usage is significantly limited by problems associated with the delivery of UV light to the reaction site. In case of biological systems, that would be a severe phototoxicity and considerably limited penetration depth of UV light in biological media.^{2, 66} The utilization of biocompatible, deep penetrating NIR light for in situ generation of UV light by the

UCNPs is expected to provide powerful leverage in chemical biology, since such photon nanoconverters can spatiotemporally restrict photochemical reactions in the nanometer regime with minimal photo-damage, enable exceptional light penetration depth, and produce desired photochemical effects with a precise control.

The importance of NIR-to-UV UC for photochemistry was first illustrated by Branda *et al.* who showed photoswitching in dithienylethene using either the $\text{NaYF}_4:\text{Yb}^{3+}/\text{Tm}^{3+}$ and the $\text{NaYF}_4:\text{Yb}^{3+}/\text{Tm}^{3+}@\text{NaYF}_4:\text{Yb}^{3+}/\text{Er}^{3+}@\text{NaYF}_4$ core/shell/shell UCNPs.^{192, 193} They also demonstrated photo-release of caged compounds,¹⁹⁴ photo-release of bio macromolecules from hydrogels,¹⁹⁵ as well as dissociation of block copolymer micelles using epitaxial core/shell $\text{NaYF}_4:\text{Yb}^{3+}/\text{Tm}^{3+}@\text{NaYF}_4$ NIR-to-UV UCNPs.¹⁹⁶ However, none of these reports involves the use of a biological model, which is needed to assess the potential use of these photon nanoconverters in biomedical field.

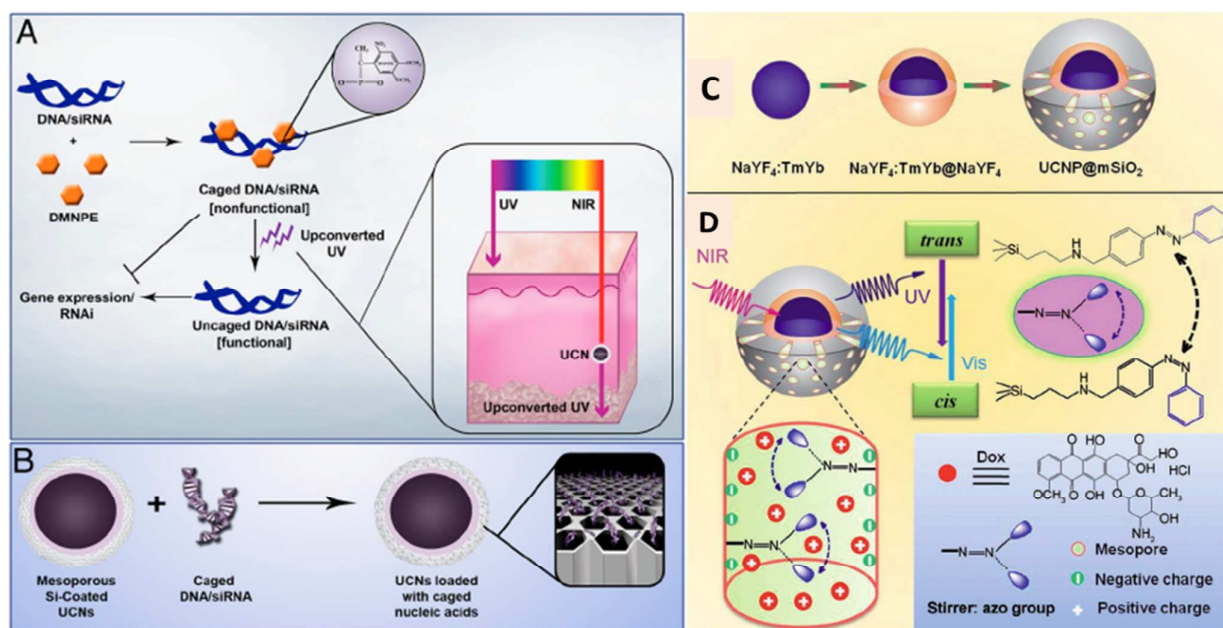


Figure 15. NIR Light-controlled release of (a, b) genetic materials using photo-uncaging, and (c, d) the chemotherapeutics drug doxorubicin (Dox), using a photomechanical path. (a) Plasmid DNA and

siRNA are caged with DMNPE and then uncaged by NIR-to-UV light conversion by the core/shell UCNPs/silica nanostructure. The inset shows the penetration depth of UV and NIR light in the skin. (b) Loading of caged plasmid DNA/siRNA into the mesopores of the core/shell UCNPs/silica nanostructure. (c) Synthetic procedure for an epitaxial core/shell upconverting nanoparticle coated with a mesoporous silica outer layer. (d) NIR light-triggered Dox release by the NIR-to-UV conversion, which causes trans–cis photoisomerization of azo molecules grafted in the mesopore network of a mesoporous silica layer. Reproduced with permission from refs. 27 and 155. Copyright 2012 National Academy of Sciences, and 2013 John Wiley and Sons.

Recently, light-regulated release *in vitro* and *in vivo* has been shown by a number of groups, using non-epitaxial UCNPs@silica nanostructures which have strong NIR-to-UV upconversion, and provide an adequate space (mesopores and the surface) in the silica shell to hold pertinent molecules (genetic materials, chemotherapeutic drugs, etc). Another important advantage of the core/shell structure is the nanoscale distance between the light-sensitive molecules in the silica shell and the core UCNPs that can allow for an efficient photoactivation process. The involved light-activatable molecules can be either a caged molecule, one moiety of which can be cleaved upon UV irradiation to release (or uncage), or a photoisomerizable molecule, the structure or spatial conformation of which can be changed upon UV irradiation. Zhang *et al.* reported on mesoporous silica coated NIR-to-UV NaYF₄:Yb³⁺/Tm³⁺@NaYF₄ nanostructures to release the photocaged nucleic acids in much deeper tissues compared to conventional systems (Figures 15 a, b).²⁷ The use of photo-uncaging processes has also been reported by Xing *et al.*, Li *et al.*, as well as by us for light-controlled release using various core/shell nanostructures.^{66, 197, 198} Shi *et al.* reported on *in vitro* control of Dox drug release using NaYF₄:Yb³⁺/Tm³⁺@NaYF₄ coated with an azo-modified

mesoporous silica, which exploits the NIR-to-UV light-controlled trans–cis photoisomerization of azo molecules grafted in the mesopore network of a mesoporous silica layer (Figures 15 c, d).¹⁵⁵ Real time monitoring of NIR-to-UV drug release *in vitro* and *in vivo* using simultaneous UCPL and MRI imaging has also been demonstrated by them using NaYF₄:Yb³⁺/Tm³⁺@NaGdF₄ UCNPs coated with an azo-modified mesoporous silica.¹⁶¹ It is worth noting that epitaxial core/shell NIR-to-UV UCNPs are preferred for these light-regulated processes, as it can deliver more UV light for use than UCNPs that are devoid of an epitaxial shell, mainly due to the higher UC efficiency.

5.1.4. Photodynamic Therapy

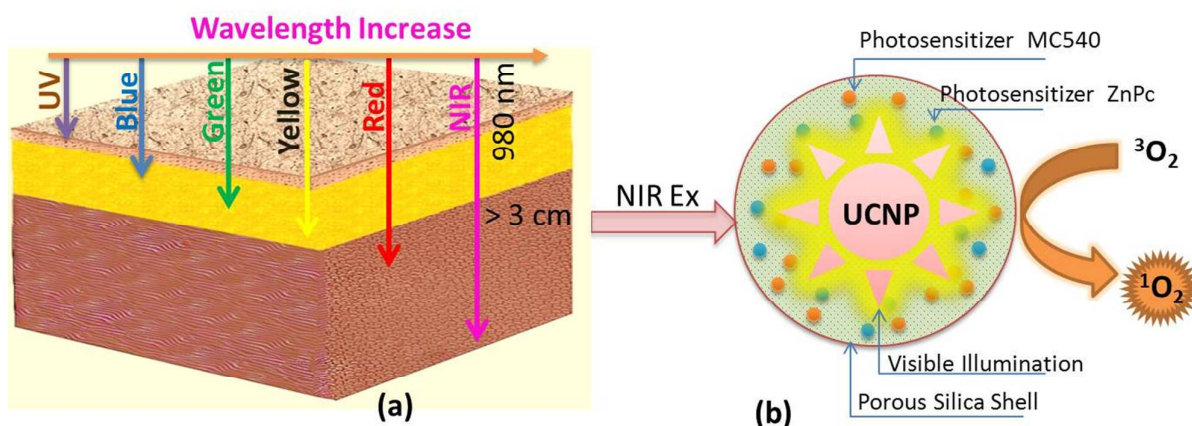


Figure 16. (a) Schematic illustration of the penetration depth of different wavelength in a tissue model; (b) upconversion nanoparticle as a frequency conversion nanotransducer to convert the NIR excitation to visible illumination for activation of photosensitizers, producing reactive singlet molecular oxygen for photochemical treatment of diseased sites.

Photodynamic therapy (PDT) is an important noninvasive treatment modality of cancer and other diseases, which is conducted with light-sensitive compounds called photosensitizers (PS) or PDT drugs. PS are nontoxic in “dark”, not light-activated state, but becomes cytotoxic, generating reactive species (e.g., excited state of molecular oxygen, ¹O₂), upon exposure with light of appropriate

wavelengths matching PS optical absorption.¹²³ PDT has been approved by the Food and Drug Administration in the United States as well as by equivalent agencies in other countries for treatment of certain types of cancer as well as for macular degeneration and some skin diseases.¹⁶⁷ The photosensitizers used in conventional PDT are mostly activated by visible light, which has limited penetration through a biological tissue (consult Figure 16 a). Therefore, the application of these visible light photosensitizers is limited to treating surface tumors on or just below the skin or on the lining of internal organs or cavities, and is consequently less effective when treating deep and thick tumors. As NIR light in the range of ~700-1100 nm has a much greater penetration depth in tissues than the visible light, the NIR-excitable UCNPs can efficiently convert the deep penetrating NIR light within this window to visible or UV wavelengths that can excite conventional photosensitizers to produce cytotoxic agent promising their application in PDT of thick tumors.¹²³

Though the potential of UC PDT for deep tissues was pointed out earlier,¹⁶⁷ the inability to achieve efficient upconversion in water dispersible nanoparticles has been limiting its use in PDT until recently.¹⁹⁹ Taking advantage of an efficient energy transfer (a mechanism of Luminescence Resonance Energy Transfer, LRET)²⁰⁰ from blue, green, and red emitting UCNPs to photosensitizers with appropriate absorption, a broad spectrum of UCNP-photosensitizer systems have been established for *in vitro* PDT^{201, 202} A general non-epitaxial core/shell structure has been utilized, where UCNPs constitute the core and the photosensitizer contained in silica or a polymer as the shell. We illustrate these core/shell nanostructures in Figure 16 (b), based on the typically used mesoporous silica coated UCNPs. A close proximity between the photosensitizer/s encased in the mesoporous silica shell and the UCNP core allows for energy transfer from the core to the photosensitizers, thereby activating the photosensitizers to generate cytotoxic species (¹O₂) from oxygen molecules,

which exist in the environment in its ground electronic state ($^3\text{O}_2$).

In vivo UC PDT was first demonstrated by Liu *et al.* using PEGylated amphiphilic polymer-coated hexagonal $\text{NaYF}_4:\text{Yb}^{3+}/\text{Er}^{3+}$ UCNPs in association with the chlorine 6 photosensitizer.²⁰³ However, the tumor-selectivity of this UCNP-photosensitizer nanosystem is not shown in this work due to the lack of tumor targeting ligand. Also, the employed $\text{NaYF}_4:\text{Yb}^{3+}/\text{Er}^{3+}$ UCNPs without an epitaxial shell have lower UC QY which results in reduced treatment efficacy. Mesoporous silica-coated $\text{NaYF}_4:\text{Yb}^{3+}/\text{Er}^{3+}$ UCNPs with a tumor-targeting agent have been developed, which not only allow selective accumulation in tumor, but also permit a high loading of photosensitizers (consult Figure 16 b).^{26, 153} Visible UC emission with two main peaks, green (~540 nm) and red (~660 nm), is well matched with the absorption of two photosensitizers, merocyanine 540 (MC540) and zinc (II) phthalocyanine (ZnPc), thus yielding greater PDT efficacy compared to approaches using a single photosensitizer.²⁶ *In vivo* studies have shown a tumor growth inhibition in tumor-bearing mice using intratumoral injection of non-targeted UCNPs or intravenous injection of UCNPs conjugated with a tumor-targeting agent, followed by UC PDT.

As it is noted above, the use of UCNPs makes possible UCPL imaging at an unprecedented depth of more than 3 cm, utilizing an excitation of 980 nm and an upconversion emission at 800 nm (see section 5.1.1).²⁵ It is important to note that while during imaging, NIR light goes in (980 nm) and comes out (800 nm), PDT requires only one way for NIR light (i.e., 980 nm) to propagate and excite photosensitizers. This peculiarity has strong implications for the possibility to treat deep-seated tumors using UC PDT. However, the efficacy of upconversion PDT strongly depends on the efficiency (brightness) of the UCNPs. New designs of high-quality epitaxial core/shell UCNPs that outperform present forms with improved optical properties are required for PDT in deeper

tissues, in particular, at an excitation density lower than $\sim 10^{-1}$ W/cm², to compensate for attenuation of the excitation light and make possible PDT of deeper tissues.

5.2 Applications in Solar Energy Harvesting

The loss of sub-band-gap photons is one of the major obstacles on the way of improving efficiency of solar cells, as only absorption of photons with energy higher than the band-gap can generate electron–hole pairs contributing to electric current.³³ For example, the c-Si solar cells have a low semiconductor band gap, and thus a relatively small part of solar irradiation is unabsorbed and thus lost (transmission loss). However, even in such case, the energy loss still can be as high as $\sim 20\%$.²⁰⁴ Without altering the already existing designs and merits of a solar cell, UC technology provides a solution to circumvent this transmission loss by converting two or more sub-band-gap photons into one above-band-gap photon. Indeed, theoretical calculations indicate that the Shockley-Queisser efficiency limit for a c-silicon solar cell can be increased from $\sim 30\%$ to 40.2%, when combined with ideal upconverters under non-concentrated air mass (AM) 1.5 solar irradiation.²⁰⁵ Moreover, even with a very narrow absorption bandwidth between 0.1–0.5 eV, upconverters can boost the Shockley-Queisser efficiency of a 1.7 eV band gap cell from 28.2% to 33.5–43.6%.²⁰⁶ Potential impacts of UC are now fueling the development of appropriate UC materials and their use in photovoltaics.

UCNPs are able to work efficiently in the NIR range of ~ 800 – 1600 nm. Some of examples are: (i) Nd³⁺/Yb³⁺/Ln³⁺ (Ln=Er, Tm, Ho) are able to harvest photons at ~ 800 nm and then produce visible upconversion at ~ 480 , 550, or 650 nm;^{84, 86} ii) Yb³⁺/Ln³⁺ (Ln=Er, Tm, Ho) are capable of up-conversion from 980 nm to ~ 480 , 550 or ~ 650 nm;^{207, 208} iii) Ho³⁺ can upconvert light at ~ 1180 nm to ~ 550 nm and ~ 650 nm; iv) Er³⁺ can upconvert light at ~ 1500 nm to ~ 550 nm and ~ 650 nm.³³

²⁰⁹ The upconversion in $\text{NaYF}_4:\text{Er}^{3+}$ powders was shown to significantly improve the response of a silicon solar cell at 1532 nm,²¹⁰ while the use of $\text{LaF}_3:\text{Yb}^{3+}/\text{Er}^{3+}$ and $\text{YF}_3:\text{Yb}^{3+}/\text{Er}^{3+}$ UCNPs resulted in an impressive increase in the efficiency of dye-sensitized solar cells (DSSCs) at ~ 980 nm.^{211, 212} We have also reported an improvement of the DSSC efficiency through infiltration of ~ 20 nm colloidal $\text{NaYF}_4:\text{Yb}^{3+}/\text{Er}^{3+}$ UCNPs into the TiO_2 pores in the DSSC device. This increase was ascribed to a combination of the overall increased light absorption of visible solar light by dye in DSSC (due to the light scattering by UCNPs), and the upconversion of NIR light absorbed by UCNPs.²¹³ This bifunctional role (scattering/upconversion) was then explored later in a DSSC using non-epitaxial core/shell $\beta\text{-NaYF}_4:\text{Yb}^{3+}/\text{Er}^{3+}@\text{SiO}_2$ UCNPs (Figure 17 a-c) and core/shell/shell $\beta\text{-NaYF}_4:\text{Yb}^{3+}/\text{Er}^{3+}@\text{SiO}_2@\text{TiO}_2$ sub-micropisms, both producing an impressive efficiency increase of 6-11%.^{214, 215} It is worth noting that the performance of an inverted polymer bulk heterojunction (BHJ) solar cell has also been improved by utilizing the bifunctional role of $\text{NaYF}_4:\text{Yb}^{3+}/\text{Er}^{3+}$ UCNPs incorporated into a blend of PCDTBT:PCBM (Figure 17 d).²¹⁶ The use of epitaxial core/shell hexagonal $\text{NaYF}_4:\text{Yb}^{3+}/\text{Er}^{3+}@\text{NaYF}_4$ UCNPs with highly efficient UC was also reported, which can enhance the overall DSSC efficiency by $\sim 11.9\%$ under AM 1.5 sun irradiation.²¹⁷ Plasmonic core/shell nanostructures of $\text{NaYF}_4:\text{Yb}^{3+}/\text{Er}^{3+}/\text{Gd}^{3+}$ (18/2/30 mol%) nanorods coated with Au nanoparticles or Au shell were prepared and applied to the front of a-Si:H solar cells, which resulted in a 16- to 72-fold improvement of the photocurrent under 980 nm light in comparison with the cell without an upconverter.²¹⁸ In addition, a novel core/shell $\text{NaYF}_4:\text{Yb}^{3+}/\text{Er}^{3+}@\text{TiO}_2$ nanoparticle was utilized to prepare the photoelectrode (PE) of a DSSC which showed a 23.1% enhancement of the energy conversion efficiency when compared with the one with a pure TiO_2 PE and 99.1% higher than the efficiency of the PE from a mixture of the TiO_2

and the $\text{NaYF}_4:\text{Yb}^{3+}/\text{Er}^{3+}$ UCNPs.²¹⁹ More recently, a hetero-nanostructured photoanode with core/shell/shell $\text{NaYF}_4:\text{Yb}^{3+}/\text{Er}^{3+}@/\text{NaYF}_4@/\text{TiO}_2$ nanostructures embedded in porous photonic crystals has been prepared for use in CdSe quantum dots sensitized solar cell (Figure 17 e).²²⁰

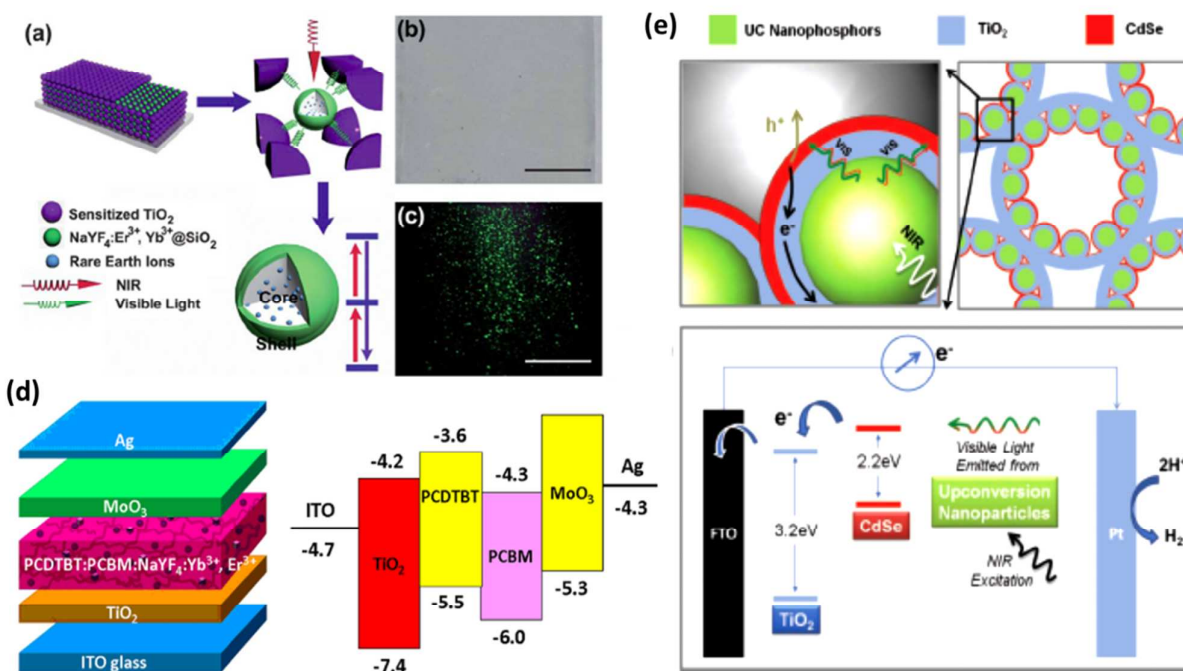


Figure 17. (a) Principle of use of photon upconversion provided by core/shell $\beta\text{-NaYF}_4:\text{Yb}^{3+}/\text{Er}^{3+}@/\text{SiO}_2$ UCNPs in the photoelectrode of a DSSC. Upconversion luminescence of photoelectrode with (c) and without (b) core/shell UCNPs confirmed the existence of core/shell UCNPs in the photo electrode. (d) The structure of an inverted polymer solar cell device which incorporates UCNPs, along with the corresponding energy level structure. (e) Energy flow in hetero-nanostructures from $\text{NaYF}_4:\text{Yb}^{3+}/\text{Er}^{3+}@/\text{NaYF}_4$ core/shell UCNPs to visible light-absorbing CdSe nanoparticles to TiO₂ photonic structures upon near-infrared photoexcitation. Energy diagram illustrating charge injection from excited CdSe into TiO₂ and the transport of photoinjected electrons to the electrode surface for hydrogen generation. Reproduced with permission from refs. 214, 216,

and 220. Copyright 2014 Royal Society of Chemistry. Copyright 2014 Elsevier. Copyright 2013 John Wiley and Sons.

Despite recent progresses in application of a range of novel and efficient core/shell UCNPs in different types of solar cells, till now the reported improvement of the overall solar cell efficiency remains rather limited till now. This is mainly because of two limitations. First of them is that the UC efficiency of current core/shell UCNPs is still far from perfect, as most of the absorbed NIR light still cannot be efficiently converted into visible range. Particularly, the efficiency of most current UCNPs is extremely low under AM 1.5 solar irradiation due to a low spectral sun irradiance on the order of $\sim 1 \text{ W/m}^2/\text{nm}$ or $\sim 0.01 \text{ W/cm}^2/\text{nm}$. For laser irradiance close to sun irradiance, the reported highest UC QY is $\sim 0.6\%$ in $\alpha\text{-(NaYbF}_4\text{:}0.5\% \text{ Tm}^{3+})\text{@CaF}_2$ core/shell UCNPs for an excitation of 0.3 W/cm^2 .²⁵ Design and fabrication of UCNPs which will be much more efficient UCNPs under low light irradiance is needed; this can be potentially achieved through nanophotonic control of utilizing a hierarchical core/shell structure. The second limitation arises from the narrow, discrete, and rather weak absorption of doped lanthanide ion owing to the nature of f-f transition. This severely restricts the harvesting capabilities of nanomaterials doped with lanthanide ions of the same type. The calculations by Briggs *et al.*, however, revealed that the lanthanide-based upconverters can significantly increase cell efficiencies from 28% to over 34% with improved quantum yield, despite their narrow bandwidths. Should upconverter quantum yields be boosted beyond their current values, cell efficiency enhancement of several absolute percent is predicted for the efficiency of a solar cell. These calculations highlight the promise of upconversion for photovoltaics and stress the critical roles of upconverter absorption, bandwidth and quantum yield in the push towards technological viability.²⁰⁶ Thus, development of efficient UC materials that are broadly responsive to infrared light

is in need. Fortunately, a number of wavelengths in the range of 800-1550 nm can be collectively upconverted by a set of lanthanide ions. A straightforward method to broaden the range of spectral sensitivity of UCNPs is to prepare a core/multiple shells nanostructure in which several types of lanthanide ions are separately doped into the core nanoparticles or in spatially isolated different shell layers (Figure 2 c). This design minimizes any possible cross relaxation between different types of lanthanide activators, and thus ensures a relatively high efficiency, while spectrally broadening the NIR light harvesting (see section 2. 2). In addition, dye-sensitized upconversion in lanthanides circumvents the drawback of low and narrow absorption of lanthanide ions, opening up the possibility of using an antenna effect to implement broad-band upconversion.⁸⁰

5.3. Security Encoding Applications

The UV-excitable Stokes fluorescence from organic dyes (i.e., UV-to-VIS downconversion) has been used for protection against counterfeiting of bills, checks and other securities (e.g., as well as for fingerprint detection). However, the problem with the application of organic dyes fluorescence in anti-counterfeiting is that it is easy to duplicate and fake. The fingerprint application of organic fluorophores suffers from background fluorescence and selectivity at the expense of generality. Since the naked eye is sensitive in the visible range, while having no response to the NIR light; this recognition offers an opportunity to address the security and the fingerprint detection applications by utilization of NIR-to-Visible UCPL. Indeed, an encrypted 3D pattern that is invisible to a human eye under regular illumination, but flares up under specific wavelength (i.e., laser diode of a specific wavelength), provides a unique way to secure the object.

Using traditional photolithography, we fabricated a well-defined pattern with single or multiple layers (3-D) from NaYF₄:Er³⁺/Yb³⁺ and NaYF₄:Tm³⁺/Yb³⁺ UCNPs with the specifically modified

surface. These security patterns became visible to naked eye when irradiated by a laser diode at ~ 975 nm, illustrating elegance suitability of UCNPs for security.²⁸ More recently, Meruga *et al.* developed a specially tailored ink, which comprised oleic acid-capped $\text{NaYF}_4:\text{Er}^{3+}/\text{Yb}^{3+}$ and $\text{NaYF}_4:\text{Tm}^{3+}/\text{Yb}^{3+}$ UCNPs in toluene and methyl benzoate with poly(methyl methacrylate) as the binding agent. The ink were used to print quick response codes, which can be scanned by a smart phone.²²¹ Jin *et al.* also demonstrated the utilization of high Tm^{3+} containing UCNPs for security printing use under an extremely high excitation density (on the order of $\sim 10^6$ W/cm^2) to produce an ultrabright visible upconverted emission for detection (Figure 18 a).²²² Ressler *et al.* used atomic force microscopy (AFM) nanoxerography to fabricate micrometer sized quick response codes through 3D close-packed assemblies of core/shell ($\text{NaYF}_4:\text{Gd}^{3+}/\text{Yb}^{3+}/\text{Er}^{3+}$)/ NaYF_4 UCNPs.²²³ Importantly, Lee *et al.* reported a facile encoding strategy that combines spatial patterning with UCNPs using polymers, single-wavelength NIR excitation and portable charge coupled device (CCD)-based decoding to distinguish particles patterned by means of flow lithography (Figure 18 b).²²⁴ Yuan *et al.* showed that UCNPs functionalized with a lysozyme-binding aptamer can be used to detect fingerprints through recognizing lysozyme in the fingerprint ridges.²²⁵ This extends the security use of UCNPs to fingerprinting, which have long been utilized as one of the most useful types of physical evidence and also utilized in areas such as forensic investigations and access control.

Most of the reported security application studies have utilized lanthanide-doped core UCNPs without any epitaxial shell. It is known that an epitaxial core/shell structure is able to increase upconversion luminescence intensity by orders of magnitude (see section 2). As a result, the use of epitaxial core/shell UCNPs in future studies will facilitate optical detection of secured patterns with considerably improved detection limit.

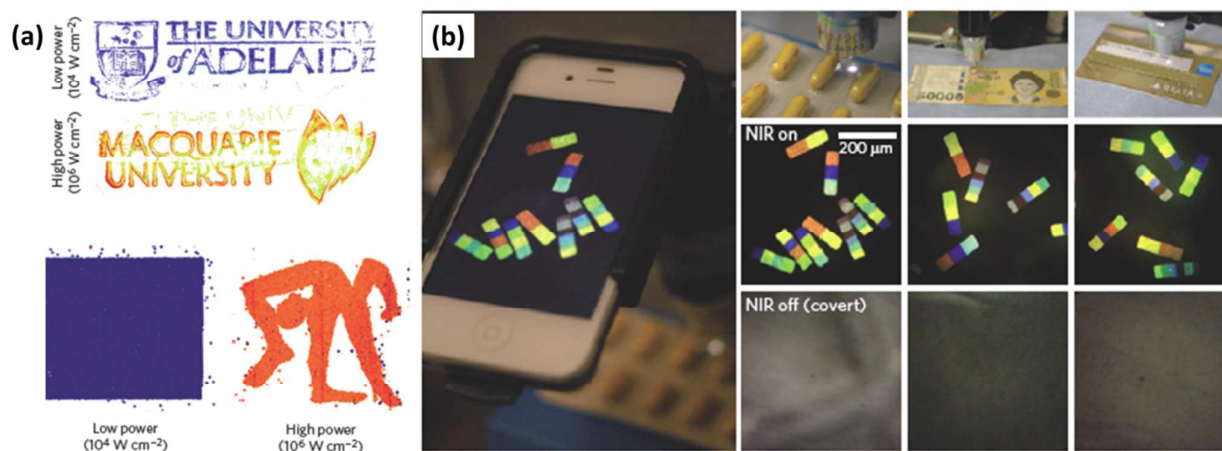


Figure 18. (a) The printed image secured with high Tm^{3+} containing UCNPs, which becomes visible when high laser power density ($\sim 10^6$ W/cm²) is utilized. (b) Imaging of encoded UCNPs with portable (Apple iPhone 4S) decoder in challenging settings (from left to right, pharmaceutical blister packs, currency, and credit cards). Top: Image acquisition using a portable decoder, Middle and bottom: Acquired image when exposed to 1W 980 nm laser excitation (middle) and in the absence of NIR excitation (bottom). Reproduced with permission from refs. 171 and 173. Copyright 2013 and 2014 Nature Publishing Group.

6. Concluding Remarks.

In this review, we have summarized nanophotonics approaches to control the excitation dynamics in core/shell upconversion nanoparticles (UCNPs), and various synthetic nanochemistries to prepare epitaxial and non-epitaxial core/shell UCNPs. A range of advanced characterization tools to provide indirect or direct evidences for the formation of core/shell structure, is also described to generate guidelines for the UC field. We have also presented some exciting examples of the emerging utilization of core/shell UCNPs for photonic applications, such as high contrast deep optical bioimaging, multimodal bioimaging, light-regulated photoactivation and drug release, photodynamic therapy, solar energy conversion and security applications. Indeed, a core-shell structure provides

numerous opportunities to manipulate excitation, energy transfer, and the emission, to tune desired UC properties for improving technology in a pertinent way. The ability to incorporate a broad range of imaging and therapeutic modalities into a single conduct, along with the capability of surface engineering for molecular targeting, promise their usage in the emerging field of theranostics applications for next generation personalized medicine. However, there still exist technical challenges for core/shell UCNPs, some of which are listed here:

- (i) The reported UC QY for core/shell UCNPs remains rather limited for all *in vivo* uses (including optical imaging, PDT, as well as for light-regulated photoactivation or drug release) especially under low irradiance of $\sim 0.1 \text{ W/cm}^2$. This value is close to the safety threshold ($\sim 0.73 \text{ W/cm}^2$ for the 980 nm cw laser diode when applied to the human skin, according to the American National Standard for Safe Use of Lasers). Moreover, a significant attenuation in the tissue will result in a significantly lower irradiance value than the threshold, when the excitation light reaches the UCNPs inside the tissue. To date, the reported highest UCQY for nanostructures is 7.6% for $(\text{LiLuF}_4:\text{Yb}^{3+}/\text{Tm}^{3+})@\text{LiLuF}_4$ core/shell UCNPs at an excitation density of 127 W/cm^2 .⁶¹ Due to the strong dependence on the excitation density, this UC QY will become significantly lower at $\sim 0.1 \text{ W/cm}^2$. The $\alpha\text{-}(\text{NaYbF}_4:0.5\% \text{ Tm}^{3+})@\text{CaF}_2$ core/shell UCNPs were reported to display a UC QY of 0.6% under an excitation of 0.3 W/cm^2 , but that is still not satisfactory. Nanophotonic approaches to control the excitation dynamics of core/shell UCNPs to produce adequate UCQY under irradiance of $\sim 0.1 \text{ W/cm}^2$,²⁵ will be appealing for all types of *in vivo* applications.
- (ii) The core/shell UCNPs have limited light harvesting ability, reducing their brightness for various bioapplications, as well as their use in solar cells. The absorption band for each type

of lanthanide ion is quite narrow and low because of the nature of the involved f-f transition, and it is specific for the lanthanide element, severely limiting the infrared light harvesting capability. It will be attractive to utilize a core/multiple shell structure (Figure 2 c) to incorporate a set of lanthanide ions into the core as well as the shells to collectively broaden the absorption of NIR light, without introducing cross relaxation processes. Moreover, the combined use of two more NIR dyes to sensitize the f-f transition will also be attractive, harvesting a broad range of NIR light.

- (iii) Concentration quenching of the emitters, typically produced by the cross relaxation processes, sets a serious limitation on the improvement of the brightness of UCNPs by simply increasing the concentration. Despite recent results have shown that the concentration quenching can be removed or reduced under high irradiance at $\sim 10^6$ W/cm² (mainly because high irradiance can activate the lanthanides at a rate higher than the quenching rate), the concentration quenching effect still dominates for the low excitation power density.^{222, 226} The necessity of high irradiance might limit the UCNPs use in a number of applications, restricting its appeal. A core/shell nanostructure is effective in eliminating the deleterious cross relaxations, as well as in suppression of surface-related quenching mechanisms. As a consequence, it will be advantageous to utilize a core/multiple shell structure to incorporate a high concentration of activators/emitters without concentration quenching, and also to produce an ultra-bright core/shell UCNPs under both low and high laser irradiance.
- (iv) To reduce possible heating-induced effects in aqueous-based environment, the commonly used excitation wavelength of ~ 980 nm (for Yb³⁺-containing UCNPs) is reported to be successfully shifted to ~ 800 nm, using a core/shell structure incorporating the Nd³⁺ ions to

sensitize Yb^{3+} ions (consult section 2. 3). This opens up new possibilities to explore use of $\text{Nd}^{3+}/\text{Yb}^{3+}$ containing UCNPs for a range of applications. Since the UC efficiency in this system relies on the efficiency of energy transfer from the Nd^{3+} ions in the shell to the Yb^{3+} ions in the core, a careful engineering of the energy transfer process might result in much more efficient UCPL. Moreover, the absolute efficiency of most of the current systems remains unassessed, suggesting necessity of a spotlight research to allow comprehensive comparison of $\text{Nd}^{3+}/\text{Yb}^{3+}$ containing UCNPs with the typically used Yb^{3+} -containing core or core/shell UCNPs.

- (v) The integration of a broad spectrum of imaging modalities such as optical imaging, MRI, PET, SPECT and CT into a single nanoparticle platform, may provide complementary information to allow accurate comprehensive diagnostics in a reduced time frame. Moreover, the ability to incorporate therapeutic entities in a non-epitaxial shell produces opportunities for imaging-guided therapy as well as for real-time assessment of a therapeutic effect. With this hierarchical core-shell approach, ~~an~~ introduction of biomolecules (which can help nanoparticles to cross various biological barriers and target an intended site through a molecular recognition mechanism) onto the surface of multimodal or multifunctional core/shell nanostructures will be more beneficial.

Acknowledgement. This work was supported by the grants from the Air Force Office of Scientific Research (Grant No. 95500910361), the Swedish Energy Agency (project 32076-1), the Natural Science Foundation of China (Grant No. 51102066), the Fundamental Research Funds for the

Central Universities, and the Program for Basic Research Excellent Talents in Harbin Institute of Technology (BRETH 2012018).

Abbreviations. UC, upconversion; IR, infrared; UCNPs, upconversion nanoparticles; NIR, near infrared; PL, photoluminescence; PDT, photodynamic therapy; PTT, photothermal therapy; LSPR, localized surface plasmon resonance; QY, quantum yield; MRI, magnetic resonance imaging ; CT, computed tomography; PET, positron emission tomography; SPECT, single-photon emission computed tomography; PA, photoacoustic; TEOS, tetraethyl orthosilicate; APTES, (3-aminopropyl)triethoxysilane; CTAB, cetyl trimethylammonium bromide; CTAC, hexadecyl trimethyl ammonium chloride; PVP, polyvinylpyrrolidone; XRD, X-ray diffraction; TEM, transmission electron microscopy; XPS, X-ray photoelectron spectroscopy; HAADF, high-angle annular dark-field; STEM, scanning transmission electron microscopy; EELS, electron energy loss spectroscopy; EDX, energy-dispersive X-ray spectroscopy; CCD, charge coupled device.

References

1. F. Auzel, *Chem. Rev.*, 2004, **104**, 139-173.
2. G. Chen, H. Qiu, P. N. Prasad and X. Chen, *Chem. Rev.*, 2014, **114**, 5161-5214.
3. G. S. He, L. S. Tan, Q. Zheng and P. N. Prasad, *Chem. Rev.*, 2008, **108**, 1245-1330.
4. M. J. Shultz, C. Schnitzer, D. Simonelli and S. Baldelli, *Int. Rev. Phys. Chem.*, 2000, **19**, 123-153.
5. P. Pantazis, J. Maloney, D. Wu and S. E. Fraser, *P. Natl. Acad. Sci. USA*, 2010, **107**, 14535-14540.
6. A. V. Kachynski, A. N. Kuzmin, M. Nyk, I. Roy and P. N. Prasad, *J. Phys. Chem. C*, 2008, **112**, 10721-10724.
7. N. Bloembergen, *Phys. Rev. Lett.*, 1959, **2**, 84.
8. F. Auzel, *C. R. Acad. Sci. (Paris)*, 1966, **262**, 1016-1019.
9. V. V. Ovsyankin and P. P. Feofilov, *Sov. Phys. JETP Lett.*, 1966, **3**, 322-323.
10. V. V. Ovsyankin and P. P. Feofilov, *Sov. Phys. JETP Lett.*, 1966, **4**, 317-318.
11. G. Y. Chen, C. H. Yang and P. N. Prasad, *Acc. Chem. Res.*, 2013, **46**, 1474-1486.
12. F. Wang, R. R. Deng, J. Wang, Q. X. Wang, Y. Han, H. M. Zhu, X. Y. Chen and X. G. Liu, *Nat. Mater.*, 2011, **10**, 968-973.
13. D. R. Gamelin and H. U. Gudel, *Acc. Chem. Res.* 2000, **33**, 235-242.
14. J. E. Stehr, S. L. Chen, N. K. Reddy, C. W. Tu, W. M. Chen and I. A. Buyanova, *Adv. Func. Mater.*, 2014, **24**, 3760-3764.
15. Z. Deutsch, L. Neeman and D. Oron, *Nat. Nanotechnol.*, 2013, **8**, 649-653.
16. J. Z. Zhao, W. H. Wu, J. F. Sun and S. Guo, *Chem. Soc. Rev.*, 2013, **42**, 5323-5351.
17. F. Wang and X. G. Liu, *Chem. Soc. Rev.*, 2009, **38**, 976-989.
18. X. Wang, X. G. Kong, Y. Yu, Y. J. Sun and H. Zhang, *J. Phys. Chem. C*, 2007, **111**, 15119-15124.
19. P. N. Prasad, *Nanophotonics*, Wiley-Interscience, New Jersey, 2004.
20. G. H. Dieke and H. M. Crosswhite, *Appl. Opt.*, 1963, **2**, 675-686.
21. B. R. Judd, *Phys. Rev.*, 1962, **127**, 750-761.
22. G. S. Ofelt, *J. Chem. Phys.*, 1962, 511-520.

23. B. G. Wybourne, *J. Opt. Soc. Am.*, 1965, **55**, 928-934.
24. M. Nyk, R. Kumar, T. Y. Ohulchansky, E. J. Bergey and P. N. Prasad, *Nano Lett.*, 2008, **8**, 3834-3838.
25. G. Y. Chen, J. Shen, T. Y. Ohulchansky, N. J. Patel, A. Kutikov, Z. P. Li, J. Song, R. K. Pandey, H. Agren, P. N. Prasad and G. Han, *ACS Nano*, 2012, **6**, 8280-8287.
26. N. M. Idris, M. K. Gnanasammandhan, J. Zhang, P. C. Ho, R. Mahendran and Y. Zhang, *Nat. Med.*, 2012, **18**, 1580-1585.
27. M. K. G. Jayakumar, N. M. Idris and Y. Zhang, *P. Natl. Acad. Sci. USA*, 2012, **109**, 8483-8488.
28. W. J. Kim, M. Nyk and P. N. Prasad, *Nanotechnology*, 2009, **20**, 185301.
29. S. W. Hao, G. Y. Chen and C. H. Yang, *Theranostics*, 2013, **3**, 331-345.
30. F. Vetrone, R. Naccache, A. Zamarron, A. J. de la Fuente, F. Sanz-Rodriguez, L. M. Maestro, E. M. Rodriguez, D. Jaque, J. G. Sole and J. A. Capobianco, *ACS Nano*, 2010, **4**, 3254-3258.
31. L. H. Fischer, G. S. Harms and O. S. Wolfbeis, *Angew. Chem. Int. Edit.*, 2011, **50**, 4546-4551.
32. J. Shen, L. Zhao and G. Han, *Adv. Drug. Deliver. Rev.*, 2013, **65**, 744-755.
33. G. Y. Chen, J. Seo, C. H. Yang and P. N. Prasad, *Chem. Soc. Rev.*, 2013, **42**, 8304-8338.
34. X. Y. Huang, S. Y. Han, W. Huang and X. G. Liu, *Chem. Soc. Rev.*, 2013, **42**, 173-201.
35. W. Ge, X. R. Zhang, M. Liu, Z. W. Lei, R. J. Knize and Y. Lu, *Theranostics*, 2013, **3**, 282-288.
36. G. Chen, T. Y. Ohulchansky, W. C. Law, H. Agren and P. N. Prasad, *Nanoscale*, 2011, **3**, 2003-2008.
37. L. Cheng, K. Yang, Y. Li, J. Chen, C. Wang, M. Shao, S. T. Lee and Z. Liu, *Angew. Chem. Int. Ed.*, 2011, **50**, 7385-7390.
38. A. Kar and A. Patra, *Nanoscale*, 2012, **4**, 3608-3619.
39. N. J. J. Johnson and F. van Veggel, *Nano Res.*, 2013, **6**, 547-561.
40. F. Wang, J. A. Wang and X. G. Liu, *Angew. Chem. Int. Ed.*, 2010, **49**, 7456-7460.
41. G. Chen, T. Y. Ohulchansky, R. Kumar, H. Agren and P. N. Prasad, *ACS Nano*, 2010, **4**, 3163-3168.
42. J. C. Boyer, F. Vetrone, L. A. Cuccia and J. A. Capobianco, *J. Am. Chem. Soc.*, 2006, **128**, 7444-7445.

43. J. C. Boyer, L. A. Cuccia and J. A. Capobianco, *Nano Lett.*, 2007, **7**, 847-852.
44. G. S. Yi and G. M. Chow, *Chem. Mater.*, 2007, **19**, 341-343.
45. H. X. Mai, Y. W. Zhang, L. D. Sun and C. H. Yan, *J. Phys. Chem. C*, 2007, **111**, 13721-13729.
46. Y. Wang, L. P. Tu, J. W. Zhao, Y. J. Sun, X. G. Kong and H. Zhang, *J. Phys. Chem. C*, 2009, **113**, 7164-7169.
47. N. J. J. Johnson, A. Korinek, C. H. Dong and F. van Veggel, *J. Am. Chem. Soc.*, 2012, **134**, 11068-11071.
48. J. C. Boyer, M. P. Manseau, J. I. Murray and F. van Veggel, *Langmuir*, 2010, **26**, 1157-1164.
49. Q. Tian, K. Tao and K. Sun, *Micro Nano Lett.*, 2013, **8**, 731-734.
50. D. Li, Q. Shao, Y. Dong and J. Jiang, *J. Alloy. Comp.*, 2014, **617**, 1-6.
51. H. Schafer, P. Ptacek, O. Zerzouf and M. Haase, *Adv. Func. Mater.*, 2008, **18**, 2913-2918.
52. Y. P. Du, X. Sun, Y. W. Zhang, Z. G. Yan, L. D. Sun and C. H. Yan, *Cryst. Growth Des.*, 2009, **9**, 2013-2019.
53. Y. S. Liu, D. T. Tu, H. M. Zhu, R. F. Li, W. Q. Luo and X. Y. Chen, *Adv. Mater.*, 2010, **22**, 3266-3271.
54. H. T. Wong, F. Vetrone, R. Naccache, H. L. W. Chan, J. H. Hao and J. A. Capobianco, *J. Mater. Chem.*, 2011, **21**, 16589-16596.
55. G. S. Yi, Y. F. Peng and Z. Q. Gao, *Chem. Mater.*, 2011, **23**, 2729-2734.
56. G. Y. Chen, H. L. Qiu, R. W. Fan, S. W. Hao, S. Tan, C. H. Yang and G. Han, *J. Mater. Chem.*, 2012, **22**, 20190-20196.
57. J. Stecher, A. Rohlfing and M. Therien, *Nanomaterials*, 2014, **4**, 69-86.
58. J. Ouyang, D. Yin, X. Cao, C. Wang, K. Song, B. Liu, L. Zhang, Y. Han and M. Wu, *Dalton Trans.*, 2014, **43**, 14001-14008.
59. J. C. Boyer and F. van Veggel, *Nanoscale*, 2010, **2**, 1417-1419.
60. W. Shao, G. Y. Chen, J. Damasco, X. L. Wang, A. Kachynski, T. Y. Ohulchanskyy, C. H. Yang, H. Agren and P. N. Prasad, *Opt. Lett.*, 2014, **39**, 1386-1389.
61. P. Huang, W. Zheng, S. Y. Zhou, D. T. Tu, Z. Chen, H. M. Zhu, R. F. Li, E. Ma, M. D. Huang and X. Y. Chen, *Angew. Chem. Int. Ed.*, 2014, **53**, 1252-1257.
62. R. H. Page, K. I. Schaffers, P. A. Waide, J. B. Tassano, S. A. Payne, W. F. Krupke and W. K.

- Bischel, *J. Opt. Soc. Am. B-Opt. Phys.*, 1998, **15**, 996-1008.
63. F. Zhang, R. C. Che, X. M. Li, C. Yao, J. P. Yang, D. K. Shen, P. Hu, W. Li and D. Y. Zhao, *Nano Lett.*, 2012, **12**, 2852-2858.
64. L. X. Liu, F. Qin, H. Zhao, T. Q. Lv, Z. G. Zhang and W. W. Cao, *Opt. Lett.*, 2013, **38**, 2101-2103.
65. Y. F. Wang, L. D. Sun, J. W. Xiao, W. Feng, J. C. Zhou, J. Shen and C. H. Yan, *Chemistry-a European Journal*, 2012, **18**, 5558-5564.
66. J. Shen, G. Y. Chen, T. Y. Ohulchanskyy, S. J. Kesseli, S. Buchholz, Z. P. Li, P. N. Prasad and G. Han, *Small*, 2013, **9**, 3213-3217.
67. K. A. Abel, J. C. Boyer and F. van Veggel, *J. Am. Chem. Soc.*, 2009, **131**, 14644-14645.
68. D. Q. Chen and P. Huang, *Dalton Trans.*, 2014, **43**, 11299-11304.
69. K. W. Kramer, D. Biner, G. Frei, H. U. Gudel, M. P. Hehlen and S. R. Luthi, *Chem. Mater.*, 2004, **16**, 1244-1251.
70. J. Damasco, G. Chen, W. Shao, H. Agren, H. Huang, W. Song, J. F. Lovell and P. N. Prasad, *ACS Appl. Mater. Interfaces*, 2014, **6**, 13884-13893.
71. F. Vetrone, R. Naccache, V. Mahalingam, C. G. Morgan and J. A. Capobianco, *Adv. Func. Mater.*, 2009, **19**, 2924-2929.
72. M. L. Chen, Y. Ma and M. Y. Li, *Mater. Lett.*, 2014, **114**, 80-83.
73. Q. H. Zeng, B. Xue, Y. L. Zhang, D. Wang, X. M. Liu, L. P. Tu, H. F. Zhao, X. G. Kong and H. Zhang, *Cryst. Eng. Commun.*, 2013, **15**, 4765-4772.
74. L. Lei, D. Q. Chen, W. Zhu, J. Xu and Y. Wang, *Chem. Asian J.*, 2014, Doi: 10.1002/asia.201402610.
75. B. Zhou, L. Tao, Y. H. Tsang and W. Jin, *J. Mater. Chem. C*, 2013, **1**, 4313-4318.
76. P. Ghosh, J. Oliva, E. De la Rosa, K. K. Haldar, D. Solis and A. Patra, *J. Phys. Chem. C*, 2008, **112**, 9650-9658.
77. D. M. Yang, C. X. Li, G. G. Li, M. M. Shang, X. J. Kang and J. Lin, *J. Mater. Chem.*, 2011, **21**, 5923-5927.
78. H. Qiu, C. H. Yan, W. Shao, J. Damasco, X. Wang, H. Agren, P. N. Prasad and G. Chen, *Nanomaterials*, 2014, **4**, 55-68.
79. D. Q. Chen, L. Lei, A. P. Yang, Z. X. Wang and Y. S. Wang, *Chem. Commun.*, 2012, **48**,

5898-5900.

80. W. Q. Zou, C. Visser, J. A. Maduro, M. S. Pshenichnikov and J. C. Hummelen, *Nat. Photon.*, 2012, **6**, 560-564.
81. M. D. Ward, *Coord. Chem. Rev.*, 2010, **254**, 2634-2642.
82. X. M. Liu, X. G. Kong, Y. L. Zhang, L. P. Tu, Y. Wang, Q. H. Zeng, C. G. Li, Z. Shi and H. Zhang, *Chem. Commun.*, 2011, **47**, 11957-11959.
83. X. M. Li, R. Wang, F. Zhang and D. Y. Zhao, *Nano. Lett.*, 2014, **14**, 3634-3639.
84. J. Shen, G. Y. Chen, A. M. Vu, W. Fan, O. S. Bilsel, C. C. Chang and G. Han, *Adv. Opt. Mater.*, 2013, **1**, 644-650.
85. Y. F. Wang, G. Y. Liu, L. D. Sun, J. W. Xiao, J. C. Zhou and C. H. Yan, *ACS Nano*, 2013, **7**, 7200-7206.
86. X. J. Xie, N. Y. Gao, R. R. Deng, Q. Sun, Q. H. Xu and X. G. Liu, *J. Am. Chem. Soc.*, 2013, **135**, 12608-12611.
87. H. L. Wen, H. Zhu, X. Chen, T. F. Hung, B. L. Wang, G. Y. Zhu, S. F. Yu and F. Wang, *Angew. Chem. Int. Ed.*, 2013, **52**, 13419-13423.
88. X. M. Li, R. Wang, F. Zhang, L. Zhou, D. K. Shen, C. Yao and D. Y. Zhao, *Sci. Rep.*, 2013, **3**, 3536.
89. Y. T. Zhong, G. Tian, Z. J. Gu, Y. J. Yang, L. Gu, Y. L. Zhao, Y. Ma and J. N. Yao, *Adv. Mater.*, 2014, **26**, 2831-2837.
90. Y. X. Liu, D. S. Wang, L. L. Li, Q. Peng and Y. D. Li, *Inorg. Chem.*, 2014, **53**, 3257-3259.
91. J. R. DiMaio, C. Sabatier, B. Kokuoz and J. Ballato, *P. Natl. Acad. Sci. USA*, 2008, **105**, 1809-1813.
92. F. Wang, X. P. Fan, M. Q. Wang and Y. Zhang, *Nanotechnology*, 2007, **18**.
93. J. C. Boyer, J. Gagnon, L. A. Cuccia and J. A. Capobianco, *Chem. Mater.*, 2007, **19**, 3358-3360.
94. W. P. Qin, C. Y. Cao, L. L. Wang, J. S. Zhang, D. S. Zhang, K. Z. Zheng, Y. Wang, G. D. Wei, G. F. Wang, P. F. Zhu and R. Kim, *Opt. Lett.*, 2008, **33**, 2167-2169.
95. G. Y. Chen, H. J. Liang, H. C. Liu, G. Somesfalean and Z. G. Zhang, *Opt. Exp.*, 2009, **17**, 16366-16371.
96. L. L. Wang, M. Lan, Z. Y. Liu, G. S. Qin, C. F. Wu, X. Wang, W. P. Qin, W. Huang and L.

- Huang, *J. Mater. Chem. C*, 2013, **1**, 2485-2490.
97. Q. Q. Su, S. Y. Han, X. J. Xie, H. M. Zhu, H. Y. Chen, C. K. Chen, R. S. Liu, X. Y. Chen, F. Wang and X. G. Liu, *J. Am. Chem. Soc.*, 2012, **134**, 20849-20857.
98. H. S. Qian and Y. Zhang, *Langmuir*, 2008, **24**, 12123-12125.
99. Q. Q. Dou, N. M. Idris and Y. Zhang, *Biomaterials*, 2013, **34**, 1722-1731.
100. M. Quintanilla, F. Ren, D. Ma and F. Vetrone, *ACS Photonics*, 2014, **1**, 662-669.
101. Z. Q. Li, Y. Zhang and S. Jiang, *Adv. Mater.*, 2008, **20**, 4765-4769.
102. H. H. Gorris, R. Ali, S. M. Saleh and O. S. Wolfbeis, *Adv. Mater.*, 2011, **23**, 1652-1655.
103. H. Ding, K. T. Yong, I. Roy, H. E. Pudavar, W. C. Law, E. J. Bergey and P. N. Prasad, *J. Phys. Chem. C*, 2007, **111**, 12552-12557.
104. J. R. Lakowicz, *Anal. Biochem.*, 2001, **298**, 1-24.
105. E. Dulkeith, A. C. Morteani, T. Niedereichholz, T. A. Klar, J. Feldmann, S. A. Levi, F. van Veggel, D. N. Reinhoudt, M. Moller and D. I. Gittins, *Phys. Rev. Lett.*, 2002, **89**, 203002.
106. H. P. Paudel, L. L. Zhong, K. Bayat, M. F. Baroughi, S. Smith, C. K. Lin, C. Y. Jiang, M. T. Berry and P. S. May, *J. Phys. Chem. C*, 2011, **115**, 19028-19036.
107. M. Saboktakin, X. C. Ye, S. J. Oh, S. H. Hong, A. T. Fafarman, U. K. Chettiar, N. Engheta, C. B. Murray and C. R. Kagan, *ACS Nano*, 2012, **6**, 8758-8766.
108. W. Xu, S. Xu, Y. S. Zhu, T. Liu, X. Bai, B. A. Dong, L. Xu and H. W. Song, *Nanoscale*, 2012, **4**, 6971-6973.
109. W. H. Zhang, F. Ding and S. Y. Chou, *Adv. Mater.*, 2012, **24**, OP236-OP241.
110. H. Zhang, Y. J. Li, I. A. Ivanov, Y. Q. Qu, Y. Huang and X. F. Duan, *Angew. Chem. Int. Ed.*, 2010, **49**, 2865-2868.
111. S. Schietinger, T. Aichele, H. Q. Wang, T. Nann and O. Benson, *Nano Lett.*, 2010, **10**, 134-138.
112. Q. C. Sun, H. Mundoor, J. C. Ribot, V. Singh, Smalyukh, II and P. Nagpal, *Nano Lett.*, 2014, **14**, 101-106.
113. F. Zhang, G. B. Braun, Y. F. Shi, Y. C. Zhang, X. H. Sun, N. O. Reich, D. Y. Zhao and G. Stucky, *J. Am. Chem. Soc.*, 2010, **132**, 2850-2851.
114. L. Sudheendra, V. Ortolan, S. Dey, N. D. Browning and I. M. Kennedy, *Chem. Mater.*, 2011, **23**, 2987-2993.

115. W. Xu, B. T. Chen, W. Yu, Y. S. Zhu, T. Liu, S. Xu, X. L. Min, X. Bai and H. W. Song, *Dalton Trans.*, 2012, **41**, 13525-13532.
116. A. Priyam, N. M. Idris and Y. Zhang, *J. Mater. Chem.*, 2012, **22**, 960-965.
117. W. Deng, L. Sudheendra, J. B. Zhao, J. X. Fu, D. Y. Jin, I. M. Kennedy and E. M. Goldys, *Nanotechnology*, 2011, **22**, 325604.
118. Y. Ding, X. R. Zhang, H. Gao, S. Xu, C. Wei and Y. Zhao, *J. Lumin.*, 2014, **147**, 72-76.
119. L. P. Qian, L. H. Zhou, H. P. Too and G. M. Chow, *J. Nanopart. Res.*, 2011, **13**, 499-510.
120. Z. Q. Li, L. M. Wang, Z. Y. Wang, X. H. Liu and Y. J. Xiong, *J. Phys. Chem. C*, 2011, **115**, 3291-3296.
121. S. Liu, G. Y. Chen, T. Y. Ohulchanskyy, M. T. Swihart and P. N. Prasad, *Theranostics*, 2013, **3**, 275-281.
122. D. Liu, S. K. Cho, S. Ahn, L. Brun, C. J. Summers and W. Park, *ACS Nano*, 2014, **8**, 7780-7792.
123. P. N. Prasad, *Introduction to Nanomedicine and Nanobioengineering*, Wiley Interscience, New Jersey, 2012.
124. R. Kumar, M. Nyk, T. Y. Ohulchanskyy, C. A. Flask and P. N. Prasad, *Adv. Func. Mater.*, 2009, **19**, 853-859.
125. M. Norek, E. Kampert, U. Zeitler and J. A. Peters, *J. Am. Chem. Soc.*, 2008, **130**, 5335-5340.
126. Y. Zhang, J. D. Lin, V. Vijayaragavan, K. K. Bhakoo and T. T. Y. Tan, *Chem. Commun.*, 2012, **48**, 10322-10324.
127. C. H. Dong, A. Korinek, B. Blasiak, B. Tomanek and F. van Veggel, *Chem. Mater.*, 2012, **24**, 1297-1305.
128. D. L. Ni, W. B. Bu, S. J. Zhang, X. P. Zhang, M. Li, H. Y. Xing, Q. F. Xiao, Y. Liu, Y. Q. Hua, L. P. Zhou, W. J. Peng, K. L. Zhao and J. L. Shi, *Adv. Func. Mater.*, 2014, DOI: 10.1002/adfm.201401609.
129. G. K. Das, N. J. J. Johnson, J. Cramen, B. Blasiak, P. Latta, B. Tomanek and F. C. van Veggel, *J. Phys. Chem. Lett.*, 2012, **3**, 524-529.
130. L. Y. Zeng, L. C. Xiang, W. Z. Ren, J. J. Zheng, T. H. Li, B. Chen, J. C. Zhang, C. W. Mao, A. G. Li and A. G. Wu, *RSC Adv.*, 2013, **3**, 13915-13925.
131. Y. L. Liu, K. L. Ai, J. H. Liu, Q. H. Yuan, Y. Y. He and L. H. Lu, *Angew. Chem. Int. Ed.*, 2012,

- 51**, 1437-1442.
132. X. J. Zhu, J. Zhou, M. Chen, M. Shi, W. Feng and F. Y. Li, *Biomaterials*, 2012, **33**, 4618-4627.
133. Y. Yang, Y. Sun, T. Y. Cao, J. J. Peng, Y. Liu, Y. Q. Wu, W. Feng, Y. J. Zhang and F. Y. Li, *Biomaterials*, 2013, **34**, 774-783.
134. Q. Liu, Y. Sun, C. G. Li, J. Zhou, C. Y. Li, T. S. Yang, X. Z. Zhang, T. Yi, D. M. Wu and F. Y. Li, *ACS Nano*, 2011, **5**, 3146-3157.
135. A. Bednarkiewicz, D. Wawrzynczyk, M. Nyk and W. Strek, *Appl. Phys. B*, 2011, **103**, 847-852.
136. X. J. Yang, Q. Q. Xiao, C. X. Niu, N. Jin, J. Ouyang, X. Y. Xiao and D. C. He, *J. Mater. Chem. B*, 2013, **1**, 2757-2763.
137. G. B. Shan, R. Weissleder and S. A. Hilderbrand, *Theranostics*, 2013, **3**, 267-274.
138. P. P. Yang, S. L. Gai and J. Lin, *Chem. Soc. Rev.*, 2012, **41**, 3679-3698.
139. C. X. Li, Z. Y. Hou, Y. L. Dai, D. M. Yang, Z. Y. Cheng, P. A. Ma and J. Lin, *Biomater. Sci.*, 2013, **1**, 213-223.
140. Y. M. Yang, B. Velmurugan, X. G. Liu and B. G. Xing, *Small*, 2013, **9**, 2937-2944.
141. M. L. Viger, M. Grossman, N. Fomina and A. Almutairi, *Adv. Mater.*, 2013, **25**, 3733-3738.
142. Y. W. Zhang and Z. L. Hong, *Nanoscale*, 2013, **5**, 8930-8933.
143. W. Wang, M. Y. Ding, C. H. Lu, Y. R. Ni and Z. Z. Xu, *Appl. Catal. B-Environ.*, 2014, **144**, 379-385.
144. C. Wang, K. Song, Y. Feng, D. Yin, J. Ouyang, B. Liu, X. Cao, L. Zhang, Y. Han and M. Wu, *RSC Adv.*, 2014, **4**, 39118-39125.
145. N. M. Idris, L. S. Sasidharan, Z. Q. Li, K. Huang and Y. Zhang, *J. Mater. Chem. B*, 2014, DOI: 10.1039/C4034TB01169D.
146. Y. S. Liu, D. T. Tu, H. M. Zhu and X. Y. Chen, *Chem. Soc. Rev.*, 2013, **42**, 6924-6958.
147. J. Zhou, Z. Liu and F. Y. Li, *Chem Soc Rev*, 2012, **41**, 1323-1349.
148. W. Feng, L.-D. Sun, Y.-W. Zhang and C.-H. Yan, *Coord. Chem. Rev.*, 2010, **254**, 1038-1053.
149. H. X. Mai, Y. W. Zhang, R. Si, Z. G. Yan, L. D. Sun, L. P. You and C. H. Yan, *J. Am. Chem. Soc.*, 2006, **128**, 6426-6436.
150. C. H. Dong and F. C. J. M. van Veggel, *ACS Nano*, 2009, **3**, 123-130.

151. M. L. Deng and L. Y. Wang, *Nano Res.*, 2014, **7**, 782-793.
152. X. M. Li, D. K. Shen, J. P. Yang, C. Yao, R. C. Che, F. Zhang and D. Y. Zhao, *Chem. Mater.*, 2013, **25**, 106-112.
153. H. S. Qian, H. C. Guo, P. C. L. Ho, R. Mahendran and Y. Zhang, *Small*, 2009, **5**, 2285-2290.
154. J. Cichos and M. Karbowiak, *J. Mater. Chem. B*, 2014, **2**, 556-568.
155. J. A. Liu, W. B. Bu, L. M. Pan and J. L. Shi, *Angew. Chem. Int. Ed.*, 2013, **52**, 4375-4379.
156. S. L. Gai, P. P. Yang, C. X. Li, W. X. Wang, Y. L. Dai, N. Niu and J. Lin, *Adv. Func. Mater.*, 2010, **20**, 1166-1172.
157. Z. H. Xu, C. X. Li, P. A. Ma, Z. Y. Hou, D. M. Yang, X. J. Kang and J. Lin, *Nanoscale*, 2011, **3**, 661-667.
158. C. X. Li, D. M. Yang, P. A. Ma, Y. Y. Chen, Y. Wu, Z. Y. Hou, Y. L. Dai, J. H. Zhao, C. P. Sui and J. Lin, *Small*, 2013, **9**, 4150-4159.
159. X. J. Kang, Z. Y. Cheng, C. X. Li, D. M. Yang, M. M. Shang, P. A. Ma, G. G. Li, N. A. Liu and J. Lin, *J. Phys. Chem. C*, 2011, **115**, 15801-15811.
160. W. P. Fan, B. Shen, W. B. Bu, F. Chen, K. L. Zhao, S. J. Zhang, L. P. Zhou, W. J. Peng, Q. F. Xiao, H. Y. Xing, J. N. Liu, D. L. Ni, Q. J. He and J. L. Shi, *J. Am. Chem. Soc.*, 2013, **135**, 6494-6503.
161. J. N. Liu, J. W. Bu, W. B. Bu, W. P. Pan, F. Chen, L. P. Zhou, W. J. Peng, K. L. Zhao, J. L. Du and J. L. Shi, *Angew. Chem. Int. Ed.*, 2014, **53**, 4551-4555.
162. J. N. Liu, Y. Liu, W. B. Bu, J. W. Bu, Y. Sun, J. L. Du and J. L. Shi, *J. Am. Chem. Soc.*, 2014, **136**, 9701-9709.
163. F. Zhang, G. B. Braun, A. Pallaoro, Y. C. Zhang, Y. F. Shi, D. X. Cui, M. Moskovits, D. Y. Zhao and G. D. Stucky, *Nano Lett.*, 2012, **12**, 61-67.
164. H. Y. Xing, W. B. Bu, S. J. Zhang, X. P. Zheng, M. Li, F. Chen, Q. J. He, L. P. Zhou, W. J. Peng, Y. Q. Hua and J. L. Shi, *Biomaterials*, 2012, **33**, 1079-1089.
165. K. A. Abel, J. C. Boyer, C. M. Andrei and F. C. J. M. van Veggel, *J. Phys. Chem. Lett.*, 2011, **2**, 185-189.
166. W. Zheng, S. Y. Zhou, Z. Chen, P. Hu, Y. S. Liu, D. T. Tu, H. M. Zhu, R. F. Li, M. D. Huang and X. Y. Chen, *Angew. Chem. Int. Ed.*, 2013, **52**, 6671-6676.
167. P. N. Prasad, *Introduction to Biophotonics*, Wiley-Interscience: Hoboken, New Jersey, 2003.

168. J. Michaelis, C. Hettich, J. Mlynek and V. Sandoghdar, *Nature*, 2000, **405**, 325-328.
169. L. A. Cheng, K. Yang, S. A. Zhang, M. W. Shao, S. T. Lee and Z. A. Liu, *Nano Res.*, 2010, **3**, 722-732.
170. J. F. Jin, Y. J. Gu, C. W. Y. Man, J. P. Cheng, Z. H. Xu, Y. Zhang, H. S. Wang, V. H. Y. Lee, S. H. Cheng and W. T. Wong, *ACS Nano*, 2011, **5**, 7838-7847.
171. R. Weissleder, *Nat. Biotechnol.*, 2001, **19**, 316-317.
172. J. V. Frangioni, *Curr. Opin. Chem. Biol.*, 2003, **7**, 626-634.
173. N. Bogdan, F. Vetrone, G. A. Ozin and J. A. Capobianco, *Nano Lett.*, 2011, **11**, 835-840.
174. Q. Liu, Y. Sun, T. S. Yang, W. Feng, C. G. Li and F. Y. Li, *J. Am. Chem. Soc.*, 2011, **133**, 17122-17125.
175. H. C. Liu, C. T. Xu, G. Dumlupinar, O. B. Jensen, P. E. Andersen and S. Andersson-Engels, *Nanoscale*, 2013, **5**, 10034-10040.
176. Q. Q. Zhan, J. Qian, H. J. Liang, G. Somesfalean, D. Wang, S. L. He, Z. G. Zhang and S. Andersson-Engels, *ACS Nano*, 2011, **5**, 3744-3757.
177. H. Guo, Z. Q. Li, H. S. Qian, Y. Hu and I. N. Muhammad, *Nanotechnology*, 2010, **21**.
178. J. A. Liu, W. B. Bu, S. J. Zhang, F. Chen, H. Y. Xing, L. M. Pan, L. P. Zhou, W. J. Peng and J. L. Shi, *Chem. Eur. J.*, 2012, **18**, 2335-2341.
179. Z. Q. Li, Y. Zhang, B. Shuter and N. M. Idris, *Langmuir*, 2009, **25**, 12015-12018.
180. D. L. Ni, J. W. Zhang, W. B. Bu, H. Y. Xing, F. Han, Q. F. Xiao, Z. W. Yao, F. Chen, Q. J. He, J. N. Liu, S. J. Zhang, W. P. Fan, L. P. Zhou, W. J. Peng and J. L. Shi, *ACS Nano*, 2014, **8**, 1231-1242.
181. A. Xia, Y. Gao, J. Zhou, C. Y. Li, T. S. Yang, D. M. Wu, L. M. Wu and F. Y. Li, *Biomaterials*, 2011, **32**, 7200-7208.
182. H. Y. Chen, B. Qi, T. Moore, D. C. Colvin, T. Crawford, J. C. Gore, F. Alexis, O. T. Mefford and J. N. Anker, *Small*, 2014, **10**, 160-168.
183. A. Xia, M. Chen, Y. Gao, D. M. Wu, W. Feng and F. Y. Li, *Biomaterials*, 2012, **33**, 5394-5405.
184. Q. F. Xiao, W. B. Bu, Q. G. Ren, S. J. Zhang, H. Y. Xing, F. Chen, M. Li, X. P. Zheng, Y. Q. Hua, L. P. Zhou, W. J. Peng, H. Y. Qu, Z. Wang, K. L. Zhao and J. L. Shi, *Biomaterials*, 2012, **33**, 7530-7539.

185. J. W. Shen, C. X. Yang, L. X. Dong, H. R. Sun, K. Gao and X. P. Yan, *Anal. Chem.*, 2013, **85**, 12166-12172.
186. Y. Sun, X. J. Zhu, J. J. Peng and F. Y. Li, *ACS Nano*, 2013, **7**, 11290-11300.
187. X. J. Niu, H. Y. Chen, Y. Q. Wang, W. H. Wang, X. Y. Sun and L. X. Chen, *ACS Appl. Mater. Interfaces*, 2014, **6**, 5152-5160.
188. S. K. Maji, S. Sreejith, J. Joseph, M. Lin, T. He, Y. Tong, H. Sun, S. W.-K. Yu and Y. Zhao, *Adv. Mater. (Deerfield Beach, Fla.)*, 2014, **26**, 5633-5638.
189. G. Tian, Z. J. Gu, L. J. Zhou, W. Y. Yin, X. X. Liu, L. Yan, S. Jin, W. L. Ren, G. M. Xing, S. J. Li and Y. L. Zhao, *Adv. Mater.*, 2012, **24**, 1226-1231.
190. C. Wang, L. A. Cheng and Z. A. Liu, *Biomaterials*, 2011, **32**, 1110-1120.
191. G. Tian, W. Y. Yin, J. J. Jin, X. Zhang, G. M. Xing, S. J. Li, Z. J. Gu and Y. L. Zhao, *J. Mater. Chem. B*, 2014, **2**, 1379-1389.
192. C. J. Carling, J. C. Boyer and N. R. Branda, *J. Am. Chem. Soc.*, 2009, **131**, 10838-10839.
193. J. C. Boyer, C. J. Carling, B. D. Gates and N. R. Branda, *J. Am. Chem. Soc.*, 2010, **132**, 15766-15772.
194. C. J. Carling, F. Nourmohammadian, J. C. Boyer and N. R. Branda, *Angew. Chem. Int. Ed.*, 2010, **49**, 3782-3785.
195. B. Yan, J. C. Boyer, D. Habault, N. R. Branda and Y. Zhao, *J. Am. Chem. Soc.*, 2012, **134**, 16558-16561.
196. B. Yan, J. C. Boyer, N. R. Branda and Y. Zhao, *J. Am. Chem. Soc.*, 2011, **133**, 19714-19717.
197. L. Z. Zhao, J. J. Peng, Q. Huang, C. Y. Li, M. Chen, Y. Sun, Q. N. Lin, L. Y. Zhu and F. Y. Li, *Adv. Func. Mater.*, 2014, **24**, 363-371.
198. Y. M. Yang, Q. Shao, R. R. Deng, C. Wang, X. Teng, K. Cheng, Z. Cheng, L. Huang, Z. Liu, X. G. Liu and B. G. Xing, *Angew. Chem. Int. Ed.*, 2012, **51**, 3125-3129.
199. P. Zhang, W. Steelant, M. Kumar and M. Scholfield, *J. Am. Chem. Soc.*, 2007, **129**, 4526-+.
200. P. R. Selvin, T. M. Rana and J. E. Hearst, *J. Am. Chem. Soc.*, 1994, **116**, 6029-6030.
201. J. N. Shan, S. J. Budijono, G. H. Hu, N. Yao, Y. B. Kang, Y. G. Ju and R. K. Prud'homme, *Adv. Func. Mater.*, 2011, **21**, 2488-2495.
202. G. Tian, W. L. Ren, L. Yan, S. Jian, Z. J. Gu, L. J. Zhou, S. Jin, W. Y. Yin, S. J. Li and Y. L. Zhao, *Small*, 2013, **9**, 1929-1938.

203. C. Wang, H. Q. Tao, L. Cheng and Z. Liu, *Biomaterials*, 2011, **32**, 6145-6154.
204. B. M. van der Ende, L. Aarts and A. Meijerink, *Phys. Chem. Chem. Phys.*, 2009, **11**, 11081-11095.
205. T. Trupke, A. Shalav, B. S. Richards, P. Wurfel and M. A. Green, *Sol. Energ. Mat. Sol. C*, 2006, **90**, 3327-3338.
206. J. A. Briggs, A. C. Atre and J. A. Dionne, *J. Appl. Phys.*, 2013, **114**.
207. G. Y. Chen, Y. Liu, Y. G. Zhang, G. Somesfalean, Z. G. Zhang, Q. Sun and F. P. Wang, *Appl. Phys. Lett.*, 2007, **91**.
208. G. Y. Chen, H. C. Liu, G. Somesfalean, H. J. Liang and Z. G. Zhang, *Nanotechnology*, 2009, **20**.
209. G. Y. Chen, T. Y. Ohulchansky, A. Kachynski, H. Agren and P. N. Prasad, *ACS Nano*, 2011, **5**, 4981-4986.
210. A. Shalav, B. S. Richards, T. Trupke, K. W. Kramer and H. U. Gudel, *Appl. Phys. Lett.*, 2005, **86**.
211. G. B. Shan and G. P. Demopoulos, *Adv. Mater.*, 2010, **22**, 4373-4377.
212. J. H. Wu, J. L. Wang, J. M. Lin, Z. Lan, Q. W. Tang, M. L. Huang, Y. F. Huang, L. Q. Fan, Q. B. Li and Z. Y. Tang, *Adv. Energy Mater.*, 2012, **2**, 78-81.
213. C. Z. Yuan, G. Y. Chen, P. N. Prasad, T. Y. Ohulchansky, Z. J. Ning, H. N. Tian, L. C. Sun and H. Agren, *J. Mater. Chem.*, 2012, **22**, 16709-16713.
214. Z. Y. Zhou, J. H. Wang, F. Nan, C. H. Bu, Z. H. Yu, W. Liu, S. S. Guo, H. Hu and X. Z. Zhao, *Nanoscale*, 2014, **6**, 2052-2055.
215. L. L. Liang, Y. M. Liu, C. H. Bu, K. M. Guo, W. W. Sun, N. Huang, T. Peng, B. Sebo, M. M. Pan, W. Liu, S. S. Guo and X. Z. Zhao, *Adv. Mater.*, 2013, **25**, 2174-2180.
216. K. Z. Z. W. B. Guo, W. F. Xie, L. Sun, L. Shen, C. Y. Liu, Y. Y. He, and Z. H. Zhang *Sol. Eng. Mater. Sol. Cell.*, 2014, **124**, 126-132.
217. A. F. Khan, R. Yadav, P. K. Mukhopadhyaya, S. Singh, C. Dwivedi, V. Dutta and S. Chawla, *J. Nanopart. Res.*, 2011, **13**, 6837-6846.
218. Z. Q. Li, X. D. Li, Q. Q. Liu, X. H. Chen, Z. Sun, C. Liu, X. J. Ye and S. M. Huang, *Nanotechnology*, 2012, **23**.
219. J. Zhang, H. O. Shen, W. Guo, S. H. Wang, C. T. Zhu, F. Xue, J. F. Hou, H. Q. Su and Z. B.

- Yuan, *J. Power Sources*, 2013, **226**, 47-53.
220. L. T. Su, S. K. Karuturi, J. S. Luo, L. J. Liu, X. F. Liu, J. Guo, T. C. Sum, R. R. Deng, H. J. Fan, X. G. Liu and A. I. Y. Tok, *Adv. Mater.*, 2013, **25**, 1603-1607.
221. J. M. Meruga, W. M. Cross, P. S. May, Q. Luu, G. A. Crawford and J. J. Kellar, *Nanotechnology*, 2012, **23**.
222. J. B. Zhao, D. Y. Jin, E. P. Schartner, Y. Q. Lu, Y. J. Liu, A. V. Zvyagin, L. X. Zhang, J. M. Dawes, P. Xi, J. A. Piper, E. M. Goldys and T. M. Monro, *Nat. Nanotechnol.*, 2013, **8**, 729-734.
223. N. M. Sangeetha, P. Moutet, D. Lagarde, G. Sallen, B. Urbaszek, X. Marie, G. Viau and L. Ressler, *Nanoscale*, 2013, **5**, 9587-9592.
224. J. Lee, P. W. Bisso, R. L. Srinivas, J. J. Kim, A. J. Swiston and P. S. Doyle, *Nat. Mater.*, 2014, **13**, 524-429.
225. J. Wang, T. Wei, X. Y. Li, B. H. Zhang, J. X. Wang, C. Huang and Q. Yuan, *Angew. Chem. Int. Ed.*, 2014, **53**, 1616-1620.
226. D. J. Gargas, E. M. Chan, A. D. Ostrowski, S. Aloni, M. V. P. Altoe, E. S. Barnard, B. Sani, J. J. Urban, D. J. Milliron, B. E. Cohen and P. J. Schuck, *Nat. Nanotechnol.*, 2014, **9**, 300-305.